# Doctral dissertation
# Studies on dust-plasma interaction in Saturn's inner magnetosphere and its magnetosphere-ionosphere coupling
### (土星内部磁気圏におけるダストープラズマ相互作用及び 磁気圏ー電離圏結合に関する研究)

## Shotaro Sakai
### 堺 正太朗

Planetary and Space Group, Department of Cosmosciences,
Graduate School of Science, Hokkaido University
北海道大学 大学院理学院 宇宙理学専攻 惑星宇宙グループ

## December 2013

# Abstract

Saturn's magnetic field forms a "magnetosphere" in the surrounding space due to the interaction with the solar wind. Plasma originated in Saturn's satellites and rings exist in the inner magnetosphere inside 10 $R_S$ ($R_S$: Saturn radius, 60268 km). The moon Enceladus is evolving a lot of water vapor from its south pole, and it is one of the major sources of the plasma in the inner magnetosphere. Enceladus also expels icy dusts from the south pole. These dusts extend to the inner magnetosphere and form E ring between 3 and 8 $R_S$. An interesting feature is that the dust grains in the plume and E ring are negatively charged and their kinetics are electromagnetically coupled to the ambient plasma. A large amount of the electrons are attached to the small dust grains and the dust plays an important role in plasma as a negative charge carrier. This situation is so called "the dusty plasma" and possibly affects the electrodynamics of the extended plasma disk of the Saturn's magnetosphere.

The dust-plasma interaction in Saturn's inner magnetosphere was suggested from the observation of cold plasma characteristics. However, it is difficult to clarify the dust-plasma interaction with only observations. In this thesis, the dust-plasma interaction in the inner magnetosphere are clarified from the analyses of the cold plasma data in the Enceladus plume and the numerical model in the inner magnetosphere, and the importance of the magnetosphere-ionosphere coupling for the dust-plasma interaction is also discussed.

The in-situ observations of the Enceladus' plasma environment obtained by the Cassini Langmuir Probe is presented. Here five flybys were used, where Cassini passed across the plume of different altitudes, to determine the altitudinal profile of the plasma densities,

electron temperatures, ion speeds, and the spacecraft potential as a proxy to the electrical potential of dust grains. Combining all the results from the five flybys, the diameter of the plume was ~3.8 $R_E$ at $Z = -1.3$ $R_E$, and ~8.4 $R_E$ at $Z = -11$ $R_E$. The plume was broader in the downstream at high altitudes. The electron density was lower than the ion densities in the plume region, which was similar to previous observations near the E ring and Enceladus. The ion density and the density ratio of the electron to the ion were ~$10^4$ cm$^{-3}$ and ~1% at the low altitude of $Z = -1.3$ $R_E$ while they became ~$10^2$ cm$^{-3}$ and 50% at the high altitude of $Z = -7.3$ $R_E$. The plume signature was identified at least at $Z = -12$ $R_E$. The electron temperature was higher (~4 eV) in the plume than the background temperature at the low altitude since the photoelectron escaped from the plume gas had the high energy. The estimated negative charged dust density was ~20 cm$^{-3}$ at the low altitude and decreased to 0.3 cm$^{-3}$ at the high altitudes.

The ion velocity was calculated by using multi-component fluid equations, taking into account dust interactions to investigate the effects of ion-dust coulomb collision, mass loading, as well as taking into account magnetosphere-ionosphere coupling to investigate the effect of the magnetospheric electric field. The results show that the ion speeds can be significantly reduced by the electric fields generated by the ion-dust collisions when the dust density is high and the thickness of dust distribution is large. The ion speeds estimated from our model are consistent with the Langmuir probe observations, when the dust density is larger than ~$10^5$ m$^{-3}$ for ionospheric conductivity of 1 S.

The effect of the ionospheric conductivity to the dust-plasma interaction was investigated by using a MHD model of Saturn's mid-latitude ionosphere. The plasma density was about $10^9$ m$^{-3}$ at the altitude of 1200 km, and it decreased to about $10^7$ m$^{-3}$ at the altitude of 10000 km. Below 10000 km the light ion has the upward velocity, while heavy ions have zero or downward velocity at low altitudes. This might be due to the difference of mass. The electron increased to 20000 K at the altitude of 10000 km. This is since the heat flow significantly affects the electron temperature. The electron temperature was about 2000 K at the altitude of 1000 km, and the collision and joule heating were contributing to temperature below 2000 km. The peak density changed between about $10^8$

and $10^{10}$ m$^{-3}$ during one Saturn's day, and the electron density decreased with increasing the altitude. On the other hand, the electron temperature didn't depend on the local time, and it decreased with increasing the altitude. The Pedersen conductivity was the maximum 0.77 S on day time and the minimum 0.30 S on dawn time. The Pedersen conductivity strongly depends on the ionospheric plasma density.

The magnetospheric ion drift velocity was calculated again in consideration of the ionospheric Pedersen conductivity. The Pedersen conductivity was the largest at $L = 3$ and it decreased as the distance from Saturn was large. The conductivity changed in local time, and the maximum was on the day time and the minimum was on the dawn time. The calculated ion velocity decreased from the co-rotation speed outside 3.5 R$_\mathrm{S}$. The ion velocity was 60-80% of the co-rotation speed in the inner magnetosphere. The ion velocity was smaller than the co-rotation speed since the magnetospheric electric field is smaller than the co-rotational electric field when the current due to the ion-dust collision flows in the inner magnetosphere. The ion velocity strongly depended on the local time since the conductivity also depended on the local time. It is suggested that the dispersion of the observed speeds could show the dependence of local time. The ion velocity is fast during the solar irradiation since the Pedersen conductivity is large, while it becomes slow after the sunset because of the small conductivity.

The magnetosphere-ionosphere coupling is significantly important for the dust-plasma interaction. It is impossible to understand the dust-plasma interaction in Saturn's inner magnetosphere without understanding of the Saturn's ionosphere, since the magnetosphere and ionosphere is intimately-connected.

# Acknowledgements

# Contents

# List of Figures

# List of Tables

# Chapter 1

# General introduction

## 1.1   Saturn's system

### 1.1.1   Properties

Saturn is the sixth planet of the solar system and located in 9.5 AU from the sun. The equatorial radius is 60,268 km (= 1 $R_S$), the mass is $5.68 \times 10^{26}$ kg, the mass density is 0.69 g cm$^{-3}$, the equatorial gravity is 10.44 m s$^{-2}$, the revolution period is 29.46 years and the rotation period is 0.436 day. The slippage between rotational axis and magnetic axis is less than 1°. The magnetic moment is $4.7 \times 10^{28}$ gauss cm$^3$, which is about 600 times higher than that of the Earth. The magnetic field of Saturn is produced by the convection of conducting hydrogen [e.g., *Stevenson*, 1983] since the interior of Saturn is at high pressure and temperature due to the large masses and low thermal conductivity [*Hubbard*, 1980; *Stevenson*, 1982] and hydrogens are fluid under these condition [*Ross et al.*, 1981; *Hubbard et al.*, 1997].

Saturn has many satellites and beautiful rings. The rings are called C, B, A, F, G and E ring from inside, and they were named from A ring in order of the discovery. The rings are composed of nano to a few meter sized ice and rocks. The E ring covers the inner magnetosphere and it is possible that it plays important roles in dynamics of the inner magnetosphere. A list of the ring sizes is shown in Table 1.1.

1
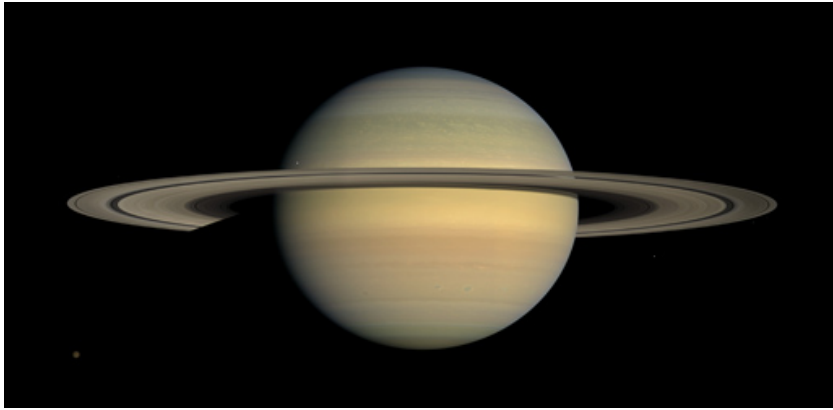
Figure 1.1: Saturn available at http://saturn.jpl.nasa.gov/photos/ [Credit: *NASA/JPL/Space Science Institute*].

Table 1.1: The ring size in Saturn. $^a$1R$_S$ = 60, 330 km, [*Stone and Owen*, 1984].

| Feature Distance from Saturn Center | (R$_S$)$^a$ |
|---|---|
| D Ring inner edge | 1.11 |
| C Ring inner edge | 1.23 |
| Maxwell Gap | 1.45 |
| B Ring inner edge | 1.53 |
| B Ring outer edge | 1.95 |
| Huygens Gap | 1.95 |
| Cassini Division | 1.99 |
| A Ring inner edge | 2.02 |
| Encke Gap | 2.21 |
| Keeler Gap | 2.26 |
| A Ring outer edge | 2.27 |
| F Ring center | 2.33 |
| G Ring center | 2.8 |
| E Ring inner edge | 3 |
| E Ring outer edge | 8 |

The number of Saturn's satellites are more than 60. Table 1.2 shows the radius and semimajor axis of the orbit of main satellites. Cassini explorer discovered that Enceladus ejects a large amount of water vapor and dust from its south pole and they are one of the sources of the E ring [e.g., *Porco et al.*, 2006]. Rhea has thin atmosphere including the oxygen and the carbon dioxide [*Teolis et al.*, 2010] and Titan has sea composed of organic substances such as methane and ethane [e.g., *Sagan and Dermott*, 1982; *Lunine et al.*,

1983; *Lunine*, 1993, 1994; *Dermott and Sagan*, 1995; *Brown et al.*, 2008]. Therefore, the existence of lives are expected in Saturn's system.

Table 1.2: Main satellites of Saturn [*de Pater and Lissauer*, 2001].

| Satellite | Radius(km) | Semimajor axis of the orbit($10^3$ km) |
|---|---|---|
| Mimas | 198.8±0.6 | 185.52 ($\sim 3.08$ $R_S$) |
| Enceladus | 249.1±0.3 | 238.02 ($\sim 3.95$ $R_S$) |
| Tethys | 529.9±1.5 | 294.66 ($\sim 4.89$ $R_S$) |
| Dione | 560±5 | 377.71 ($\sim 6.27$ $R_S$) |
| Rhea | 764±4 | 527.04 ($\sim 8.74$ $R_S$) |
| Titan | 2575±2 | 1221.85 ($\sim 20.27$ $R_S$) |
| Iapetus | 718±8 | 3561.3 ($\sim 59.09$ $R_S$) |

## 1.1.2 Enceladus and E ring

Enceladus is located in about 3.95 $R_S$ from Saturn. The radius is 247 km (1 $R_E$) and the mass is $7.0 \times 10^{19}$ kg. A main composition of atmosphere is water vapor [*Waite et al.*, 2006]. An interesting characteristic of Enceladus is a plume from the south pole. Ground-based observations revealed that the Saturn's E ring was concentrated at the orbit of Enceladus [*Baum et al.*, 1981]. Some scientists suggested that the inferred short lifetimes of the E ring particles implied a continuous supply from Enceladus, and geyser-like activity on Enceladus [*Haff et al.*, 1983; *Pang et al.*, 1984]. The neutral OH cloud discovered by the Hubble Space Telescope [*Shemansky et al.*, 1993] also required a strong source near Enceladus [*Jurac et al.*, 2001]. Cassini Ultraviolet Imaging Spectrograph (UVIS) instrument discovered that neutral O emission concentrated near the orbit of Enceladus [*Esposito et al.*, 2005]. The Cassini Imaging Science Subsystem (ISS) images found the large disruptions of the surface [*Porco et al.*, 2006], and a large perturbation of the magnetic field was seen around the south pole [*Dougherty et al.*, 2006]. These data indicated that Enceladus has a significant atmosphere and gases are continuously ejected (Fig.1.2). The detail composition of the south pole water plume was detected by the Cassini Ion and Neutral Mass Spectrometer (INMS) [*Waite et al.*, 2006]. The main component is $H_2O$, which is more than 90%, and others are $N_2$ or CO, $CO_2$, $CH_4$, $NH_3$,
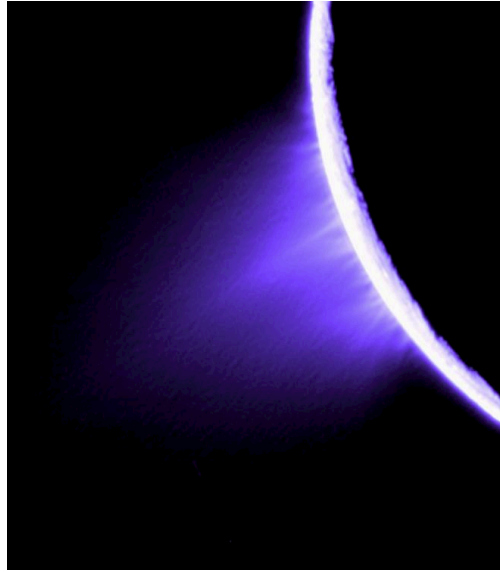
Figure 1.2: Enceladus plume available at http://saturn.jpl.nasa.gov/photos/ [Credit: *NASA/JPL/Space Science Institute*].
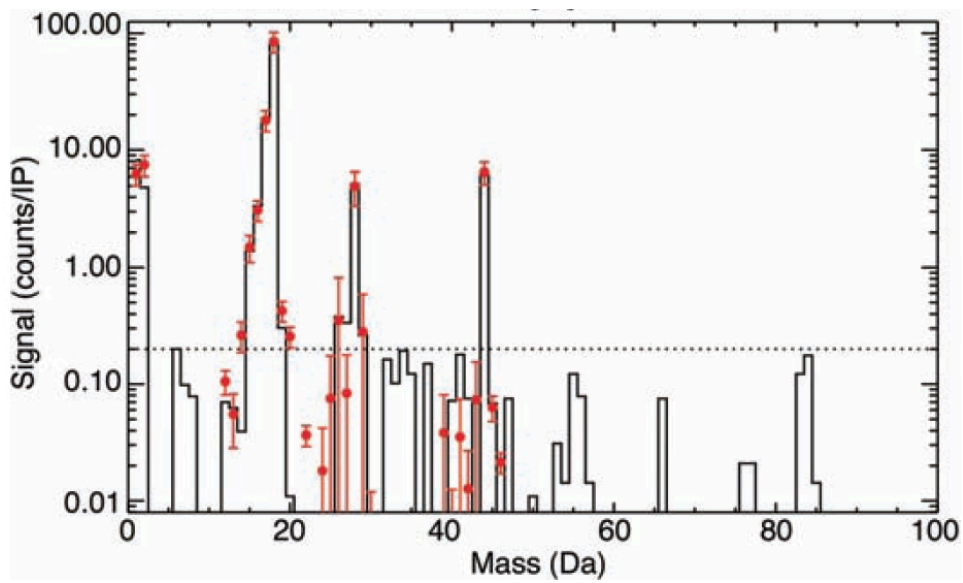


Figure 1.3: Composition of Enceladus plume [*Waite et al.*, 2006].

$C_2H_2$, HCN and $C_3H_8$ (Fig.1.3). The Cassini Cosmic Dust Analyzer (CDA) also detected a large dust grains above the south pole [*Spahn et al.*, 2006]. From these data Enceladus' south pole plume is actively erupting the plume of ice grains, water vapor and other gases, and the plume is supplying the E ring and the neutral torus.

The E ring is located between 3 and 8 $R_S$ and one of the most extensive planetary ring in our solar system. The icy moon was early on proposed to be the dominant source of ring particles since the maximum edge-on brightness occurs near Enceladus' mean orbital distance [*Baum et al.*, 1981]. In-situ observations of Voyager and Cassini provided the more information about the E ring. The CDA onboard Cassini investigated the local dust properties such as the spatial and size distribution of the ring particles [*Kempf et al.*, 2008]. They suggested that the vertical ring structure around Enceladus' orbit agreed well with a Gaussian with a full-width-half-maximum (FWHM) of ∼4200 km for grains exceeding 0.9 $\mu$m and the peak dust density to range between $1.6 \times 10^{-1}$ m$^{-3}$ and $2.1 \times 10^{-1}$ m$^{-3}$ for grains larger 0.9 $\mu$m. The Cassini Plasma Spectrometer (CAPS) detected the composition of ions in the E ring region. The composition is mainly $H_XO^+$ and the mixing ratio is about 80% [*Young et al.*, 2005]. The ejected gas and grains are extending in the inner magnetosphere [*Persoon et al.*, 2005].

## 1.2    Electromagnetic environment in Saturn's system

### 1.2.1    Ionosphere

The structure of Saturn's ionosphere has been observed by the method of radio occultation [e.g., *Kliore et al.*, 2004]. This method can obtain the vertical structure of the total electron density. Pioneer 11 and Voyager 1 and 2 provided the total electron density profiles at Saturn's ionosphere [e.g., *Kliore et al.*, 1980; *Tyler et al.*, 1981, 1982; *Lindal et al.*, 1985]. Recently, Cassini observed the density profiles at various latitudes [*Kliore et al.*, 2009] and the electron density which is the average between dawn and dusk are shown in Fig.1.4. At low and high latitude the maximum densities were about $10^9$ m$^{-3}$

and $10^{10}$ m$^{-3}$ at about 2000 km from 1 bar level respectively.

The first numerical model for the Saturn's ionosphere was constructed by *McEloy* [1973]. He only used photoionized/photodissociated and charge-exchange reactions of the hydrogen group in his model. Reactions between ions and hydrocarbons were introduced by *Atreya and Donahue* [1975]. At that time these models were not consistent with the observations from Pioneer 11 or Voyager 1 and 2. The density from models was one order of magnitude lager than the occultation observations. Therefore, they considered the loss of H$^+$ due to the vibrationally excited H$_2$ [*McElroy*, 1973] and H$_2$O from the rings and icy moons [*Connerney and Waite*, 1984].

*Moses and Bass* [2000] calculated the coupled 1 dimensional continuity equations for a set of 46 ions and 63 neutrals components which included water groups and magnesium ions in Saturn's upper atmosphere. A recent model is the Saturn-Thermosphere-Ionosphere-Model (STIM) [*Müller-Wodarg et al.*, 2006]. It is a global circulation model of Saturn's upper atmosphere and the ion densities were calculated with this model [*Moore et al.*, 2004, 2006, 2008; *Mendillo et al.*, 2005; *Moore and Mendillo*, 2005, 2007]. Fig.1.5 shows the ion densities below 3000 km of 1 bar level from STIM [*Moore et al.*, 2008]. The maximum of ion density was about $10^{10}$ m$^{-3}$ at the altitude of 1000 km and the component was H$_3^+$. The ion density decreased with increasing the altitude and main component changed to H$^+$ at the altitude of 1800 km.

*Waite* [1981] predicted that the plasma temperature would become 1000-10000 K due to the joule heating and heat flow from upper boundary. The first recent models on high latitude was solved from below the peak to an altitude of one Saturn radius for yielding densities, fluxes and temperatures of H$_3^+$ and H$^+$ [*Glocer et al.*, 2007]. The peak of ion temperature was about 1500 to 3000 K. The second recent models used STIM [*Moore et al.*, 2008]. Fig.1.6 shows the ion and electron temperature below 3000 km at each local time. They calculated the plasma temperature in the low- and mid-latitude, and the electron temperature at topside was about 500 K.
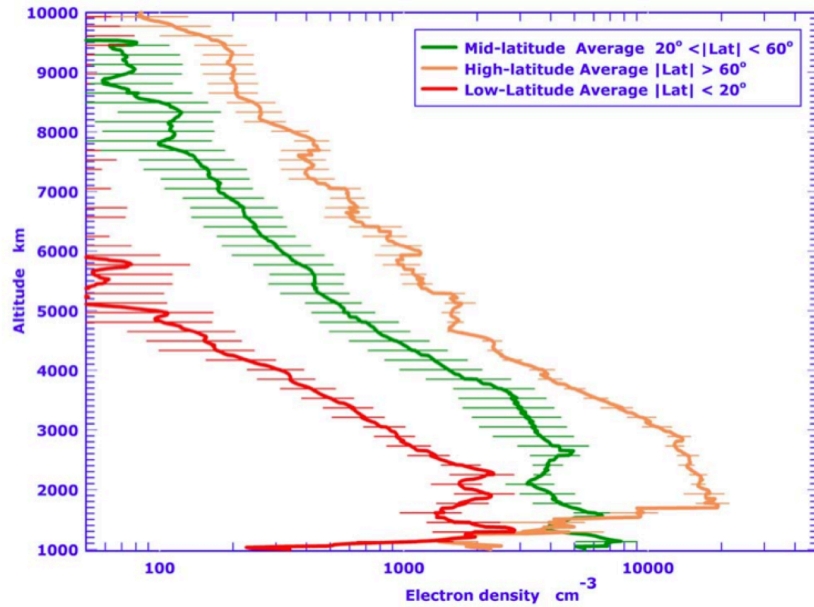
Figure 1.4: Electron density from occultations of Cassini [*Kliore et al.*, 2009].
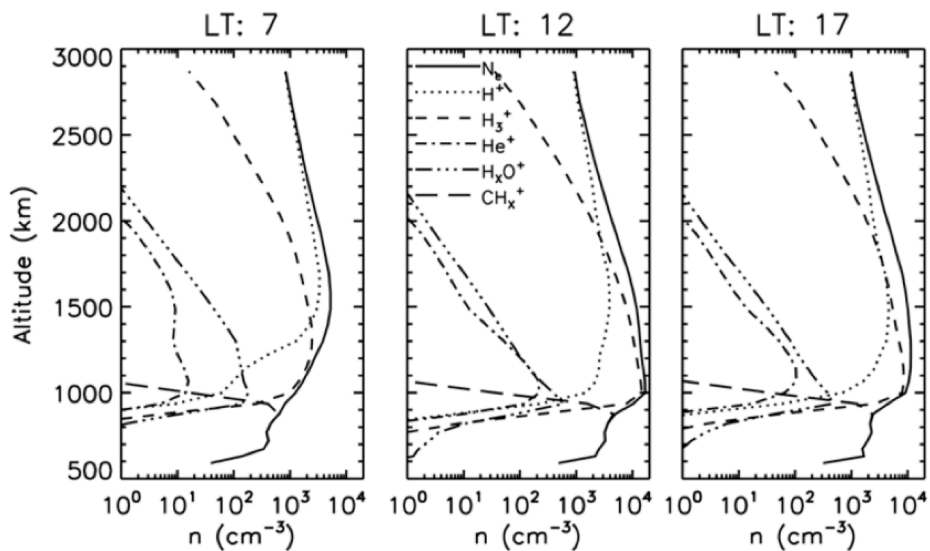


Figure 1.5: Ion density from modeling in Saturn's ionosphere [*Moore et al.*, 2008].
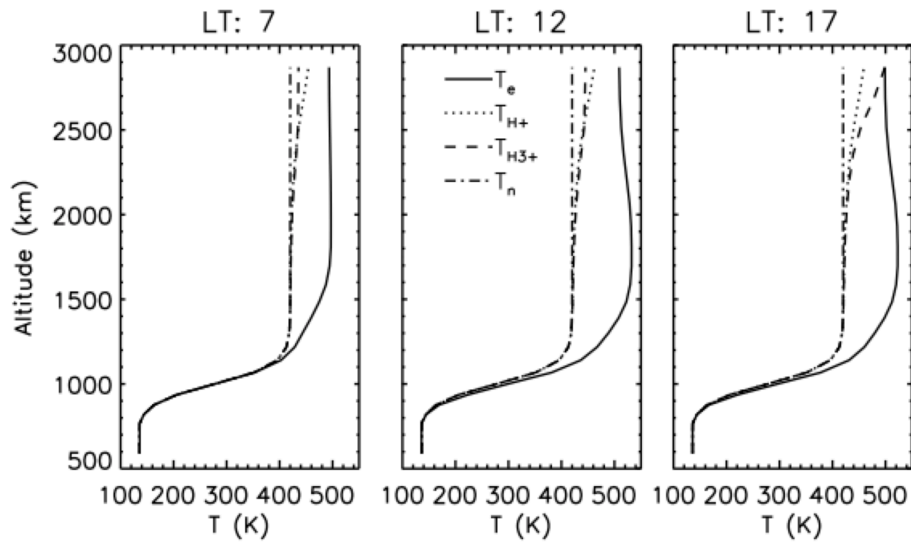
Figure 1.6: Plasma temperature from modeling in Saturn's ionosphere [*Moore et al.*, 2008].

## 1.2.2    Inner magnetosphere

Saturn's inner magnetosphere is quite different from Jovian or Earth's inner magneto-sphere. A major difference is that the Saturn's system has the large sources of the plasma and grains such as icy satellites and rings in the inner magnetosphere. Enceladus is expelling gases and grains from the south pole. The gases are ionized by the solar EUV or impacts of the energetic electrons, and the grains and the ionized plasma are extending in the inner magnetosphere. In this section, the plasma and dust environment in the inner magnetosphere is presented.

### 1.2.2.1    Plasma environment

*Persoon et al.* [2005, 2006, 2009, 2013] gave the electron density profile in the Saturn's inner magnetosphere (2 to 10 $R_S$) from the Cassini Radio Plasma Wave Science (RPWS) [*Gurnett et al.*, 2004]. They used the upper hybrid frequency observed by the RPWS for estimating the electron density. Fig.1.7 shows the latest electron density profile in the inner magnetosphere. Panel a shows the radial distribution plot of the equatorial densities over the 7 year period. The peak density was about 100 cm$^{-3}$ around 4 $R_S$ and

it decreased along each power-law. Panel b shows the equatorial density measurements averaged in non-overlapping $L$-shell bins of 0.2. There was a peak in the equatorial density around 4 $R_S$. The hybrid power-law equation was used to fit the equatorial distribution across the full range of $L$-shell values. Inside 4 $R_S$ the electron density was proportional to $R^{4.0}$, while it was proportional to $R^{-4.8}$ outside 4 $R_S$. Fig.1.8 shows a electron density
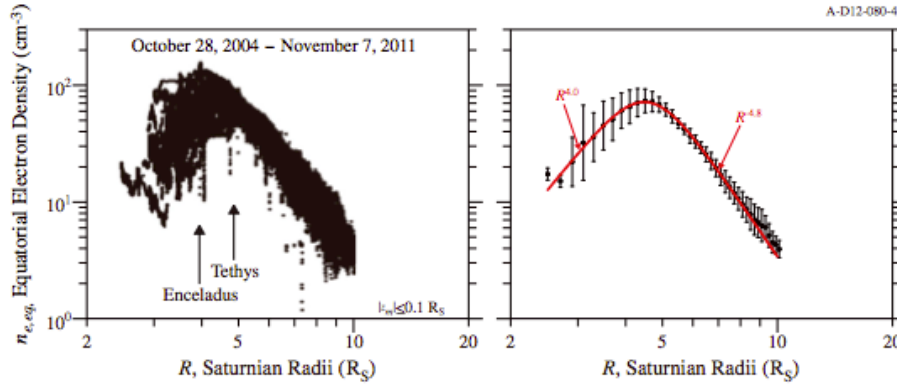


Figure 1.7: Electron density profile from 2.6 to 10.0 $R_S$. (a)Radial distribution plot of the equatorial densities. (b) Plot of the equatorial density measurements averages in non-overlapping $L$-shell bins of 0.2 [*Persoon et al.*, 2013].

contour plot in the meridian plane from 2.6 to 10 $R_S$. The densest part of the plasma torus extended from 2.6 to $\sim$8 $R_S$ with a north-south extension of $\pm 1$ $R_S$, and the value was more than 10 cm$^{-3}$.

The ion densities in Saturn's inner magnetosphere were measured by the CAPS and the RPWS/Langmuir Probe (LP). Fig.1.9 shows density profiles of the three ion species (top, H$^+$; center, H$_2^+$; bottom, W$^+$), with constraints that latitude is within $\pm 5°$ of the equatorial plane and only points for which the co-rotation direction is within the instrument field of view are included, observed by the CAPS [*Thomsen et al.*, 2010]. The large black dots show the means for the values within 1-$R_S$ $L$ bins and are plotted at the center of each bin. The H$^+$ density was about 1 cm$^{-3}$, the H$_2^+$ density was about 0.4 cm$^{-3}$, and the W$^+$ density was about 50 cm$^{-3}$ at 5 $R_S$. The ion densities decreased as $L$ was large. Fig.1.10 shows the ratio of the densities of ions with (top) $m/q = 2$, which is H$_2^+$ in the inner magnetosphere or possibly He$^{2+}$ in the outer magnetosphere, and (bottom) W$^+$ to H$^+$ as a function of radial distance. The density ratio H$_2^+$/H$^+$ increased as the
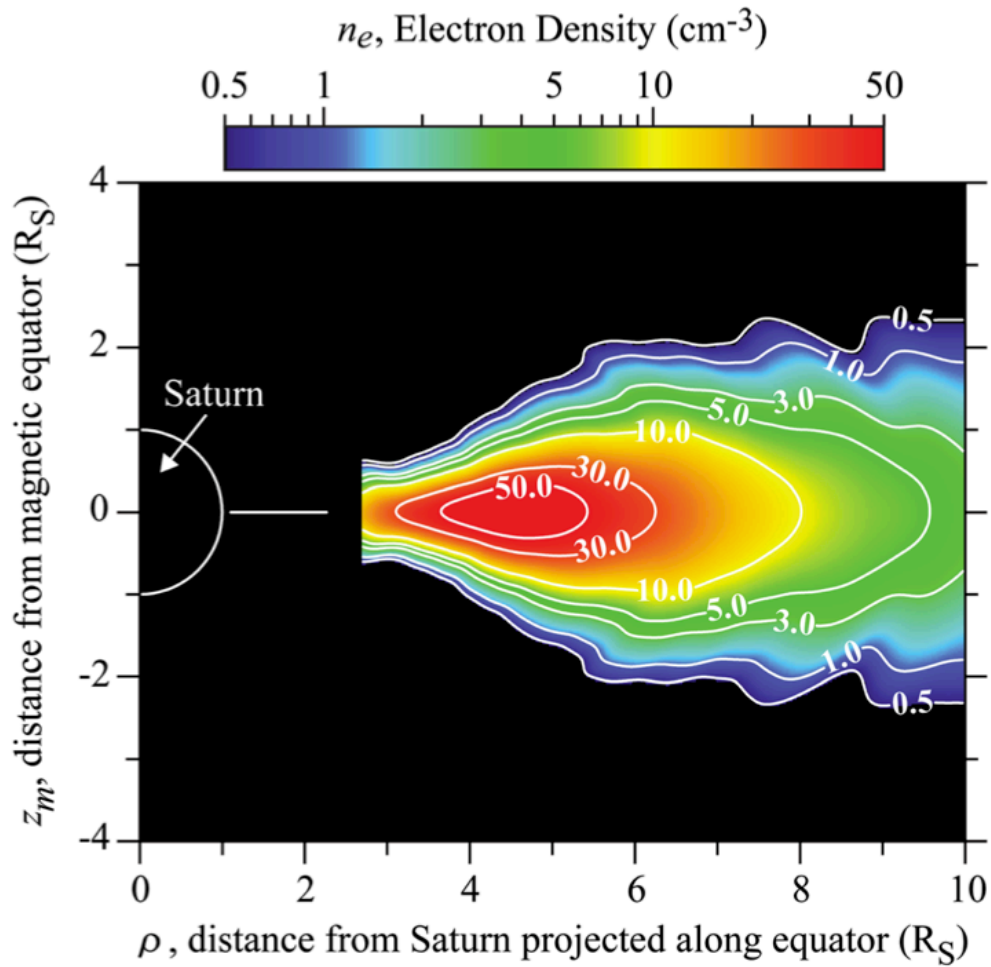
Figure 1.8: A electron density contour plot in the meridian plane [*Persoon et al.*, 2013].

radial distance was large and the maximum was at 20.2 $R_S$ on Titan's orbit. It may mean that Titan is an important source for $H_2^+$ in the outer magnetosphere. The maximum of the density ratio $W^+/H^+$ was at 4-5 $R_S$ around Enceladus' orbit and the value was larger than 10. The ratio decreased as the radial distance was larger, however, the value was generally larger than 1 within 10 $R_S$.
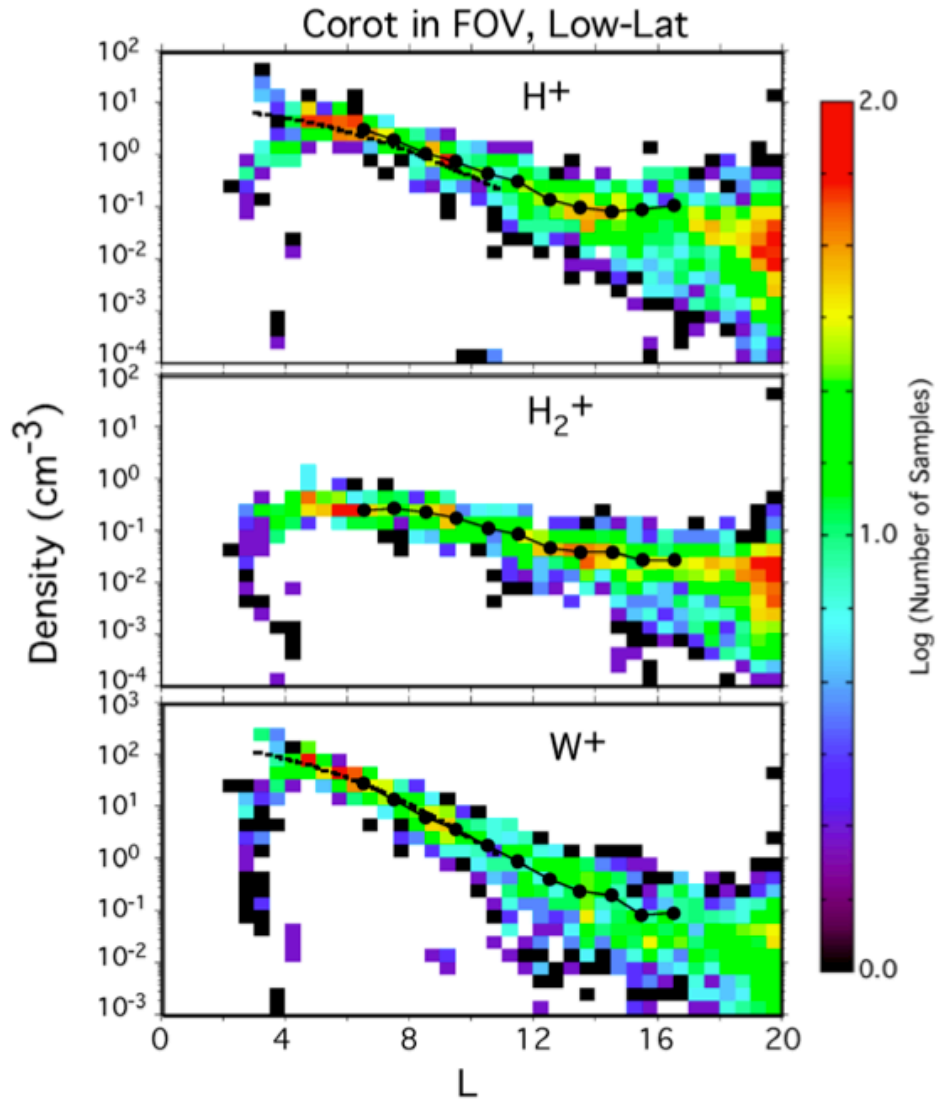


Figure 1.9: Occurrence distribution of derived densities for the three ion species (top, $H^+$; center, $H_2^+$; bottom, $W^+$) as a function of radial distance from Saturn [*Thomsen et al.*, 2010].

*Holmberg et al.* [2012] gave the total ion density from the RPWS/LP. Fig.1.11 panel a shows the derived equatorial ion densities near equatorial plane, $|Z| < 0.5$ $R_S$ as a function
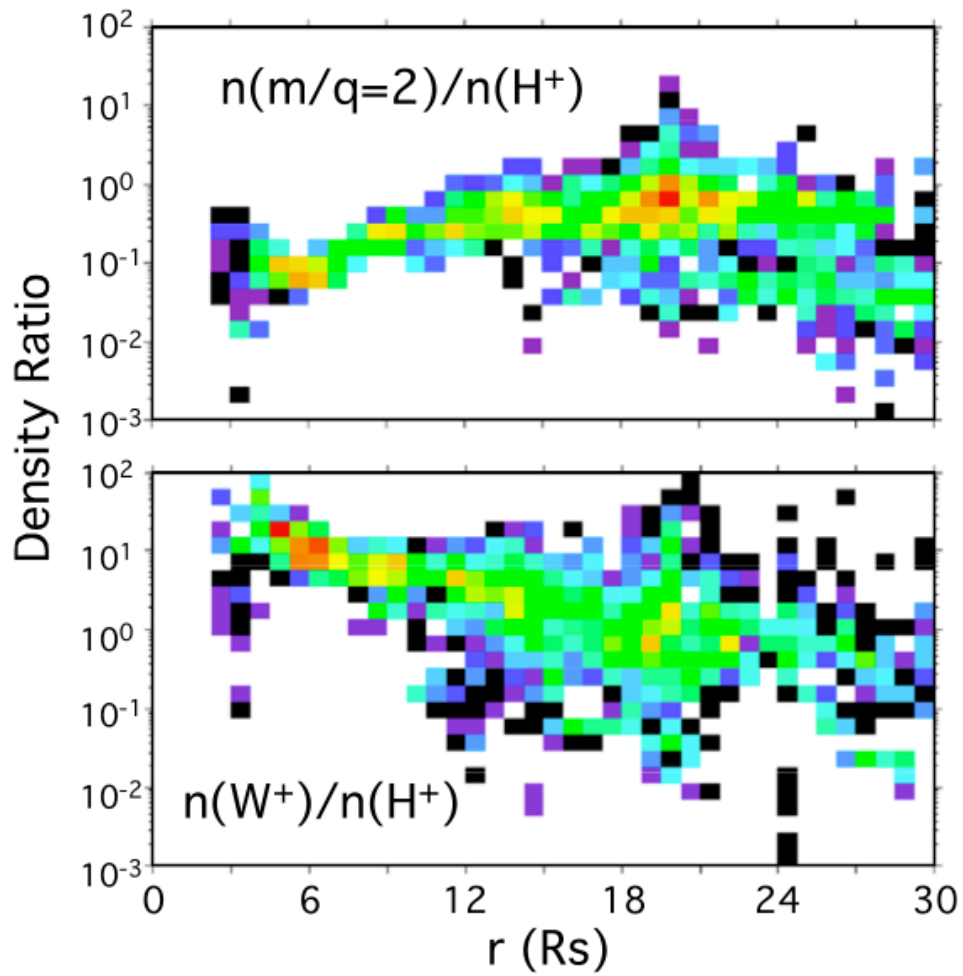
Figure 1.10: Occurrence distribution of the ratio of densities of ions with (top) $m/q = 2$ and (bottom) $W^+$ to $H^+$ as a function of radial distance [*Thomsen et al.*, 2010].

of the distance from Saturn. The highest densities were observed at the Enceladus' orbit and it was more than 200 cm$^{-3}$. The density decreased as the radial distance was large. Panels b and c show the radial distance and the density region divided into small bins (0.1 R$_S$ and 2.5 cm$^{-3}$), giving the density contribution from each bin. Panel b gives the number of data points for each bin, while panel c gives the probability of the specific bin normalized for each 0.1 R$_S$ bin. The black line of panel b shows the power-law fit, $n_{eq} = 2.2 \times 10^4 \, (1/R)^{3.63}$, given by *Persoon et al.* [2005] using electron densities derived from upper hybrid frequency data. The magenta line also shows the fitting of the ion density data derived by *Thomsen et al.* [2010] and the power-law fit is $n_i = 1.38 \times 10^6 \, (1/L)^{5.68}$. This fitting showed a good agreement in the region $7 < R < 12$ R$_S$, however, it started to deviate for $R < 7$ R$_S$. A better correlation was found with the presented exponential fit $n_i = 627 \exp(-0.517L)$ [*Thomsen et al.*, 2010], see red line of panel b. A good agreement was also found with the fit from *Persoon et al.* [2005] in the region 5-12 R$_S$.

The ion velocities were also observed by the CAPS and the RPWS/LP in the inner magnetosphere. Fig.1.12 shows the $L$ dependence of the azimuthal velocity for H$^+$, H$_2^+$ and W$^+$, selected according to the low latitude observed by the CAPS. The black solid lines in the three frames show the equatorial co-rotation velocity. The ion velocity of each species was 20-70% of the ideal co-rotation velocity. These results were consistent with those reported in the same $L$ range on the nightside by *McAndrews et al.* [2009] and the Voyager 2 values reported by *Richardson* [1998], while were ∼20-50% of those derived from INCA anisotopies by *Kane et al.* [2008].

Fig.1.13 shows the ion velocities observed by the RPWS/LP as a function of radial distance from Saturn in R$_S$ for Rev 003-133 excluding Rev 80 and 81. Panel a shows the location of individual data points, panels b and c show the number of data points and the probability of each 0.1 R$_S$ and 2.5 km/s bin. The red line gives the co-rotation speed and the green line gives the Keplerian speed. The fit $v_{i,\theta} = 1.5R^2 - 8.7R + 39$, derived from the data in the region $3.1 < R < 6.7$ R$_S$, is shown as the black line of panel b. The fit (black line) of panel c gives the velocities derived by *Wilson et al.* [2009]. Their data implied that
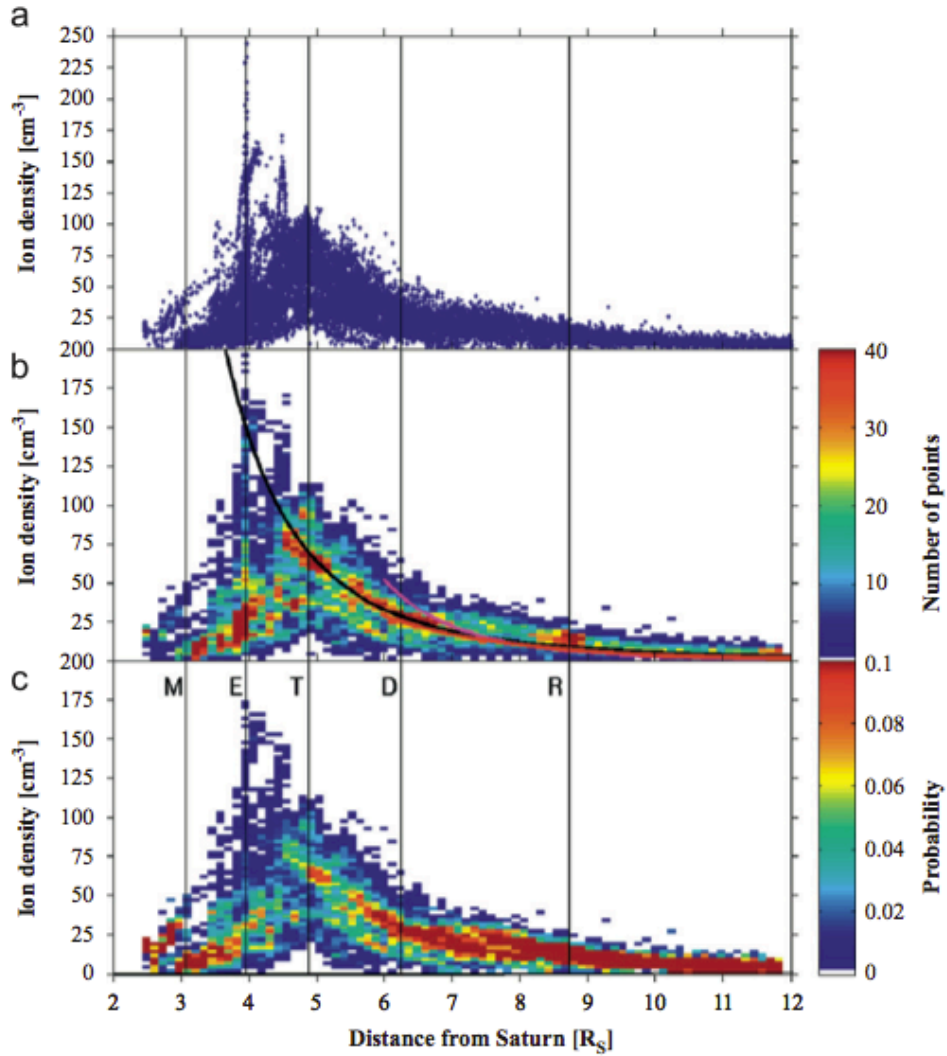
Figure 1.11: The derived equatorial ion densities as a function of radial distance from Saturn in $R_S$ for Rev 003-133 [*Holmberg et al.*, 2012].
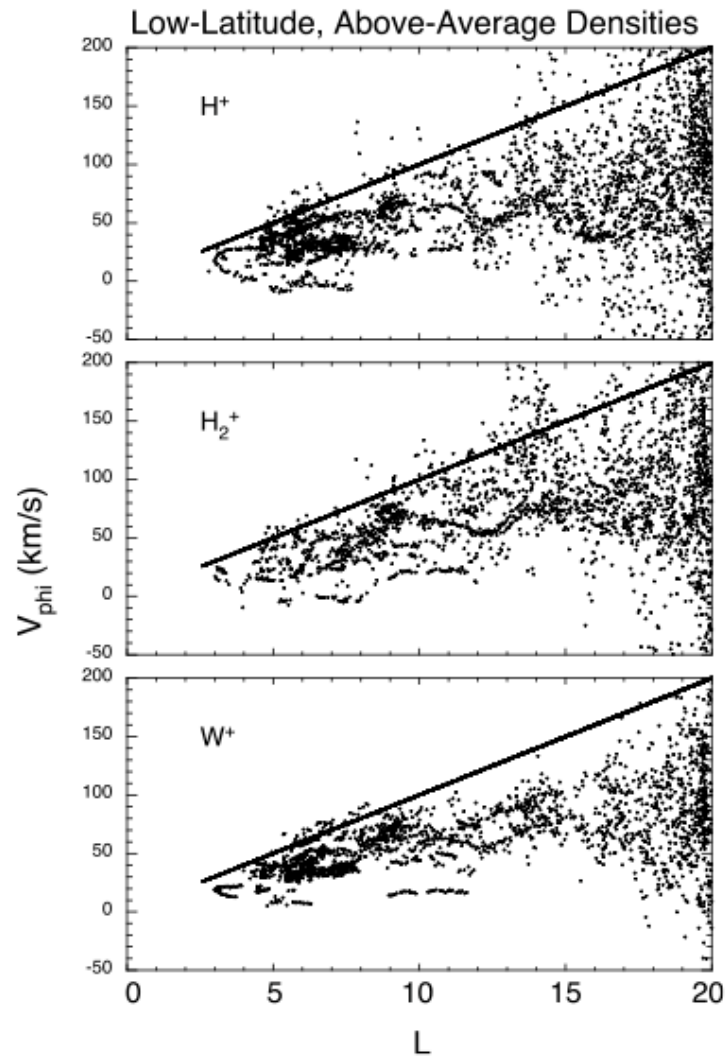
Figure 1.12: Azimuthal flow speeds derived independently from the three different species for measurements obtained at latitudes less than $5°$ [*Thomsen et al.*, 2010].

the deviation from the rigid co-rotation starts at around 3 R$_S$, a conclusion which was also suggested by *Wilson et al.* [2009]. The average ion velocity measured by *Holmberg et al.* [2012] was about 68% of the co-rotation speed at around 5 R$_S$. This was also a good agreement with the speeds presented by *Thomsen et al.* [2010], who estimated the average velocities to vary between ∼50% and 70% of the full co-rotation speed.
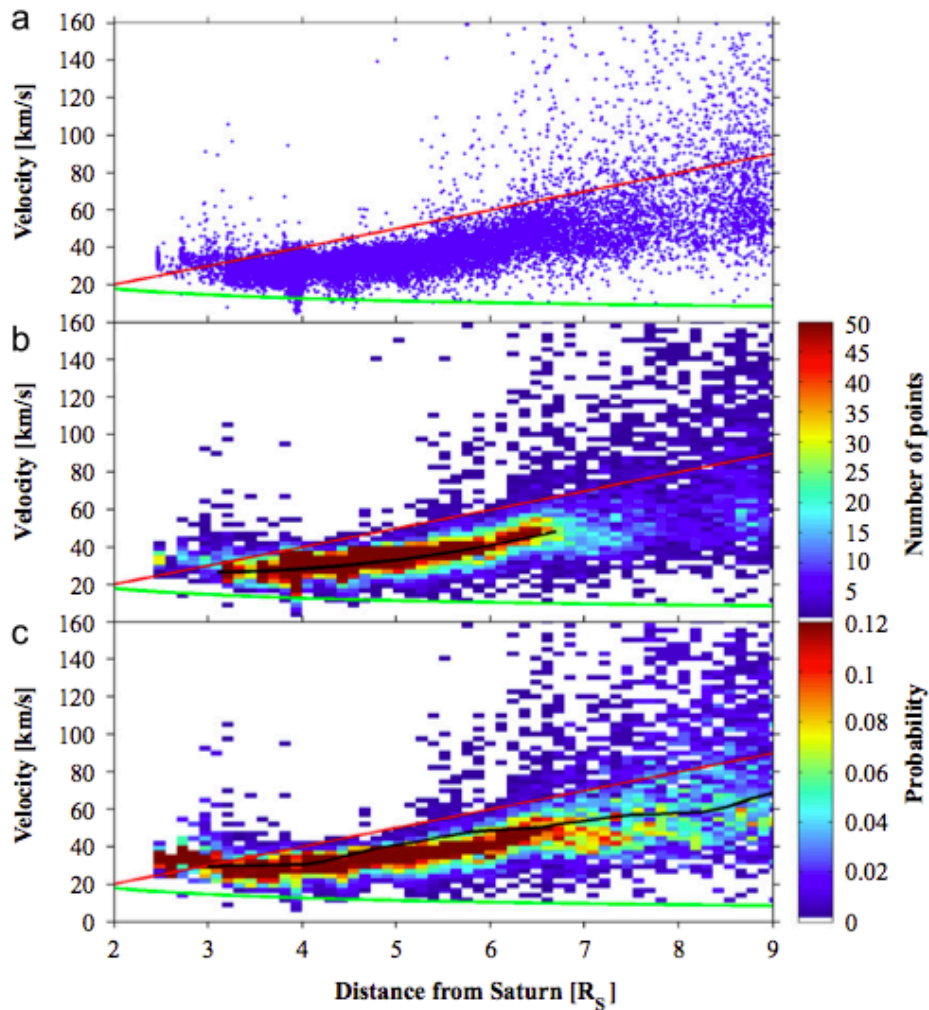


Figure 1.13: The derived ion velocities as a function of radial distance from Saturn in R$_S$ for orbits 003-133 [*Holmberg et al.*, 2012].

### 1.2.2.2   Dusty plasma environment

In space, the dust and plasma are interacting via exchange of charge, mass, momentum and energy. The dust coexists with plasma and forms a "dusty plasma" [e.g., *Mendis,*

1979; *Goertz*, 1989].  The dust is charged positively or negatively in plasma, and thus the charge neutrality is determined by the electrons, the ions and the charged dust.  In Saturn's magnetosphere, a large amount of negatively charged dusts can be existence, especially inside 7 $R_S$ [*Horányi et al.*, 2004; *Kempf et al.*, 2008].  Fig.1.14 shows the
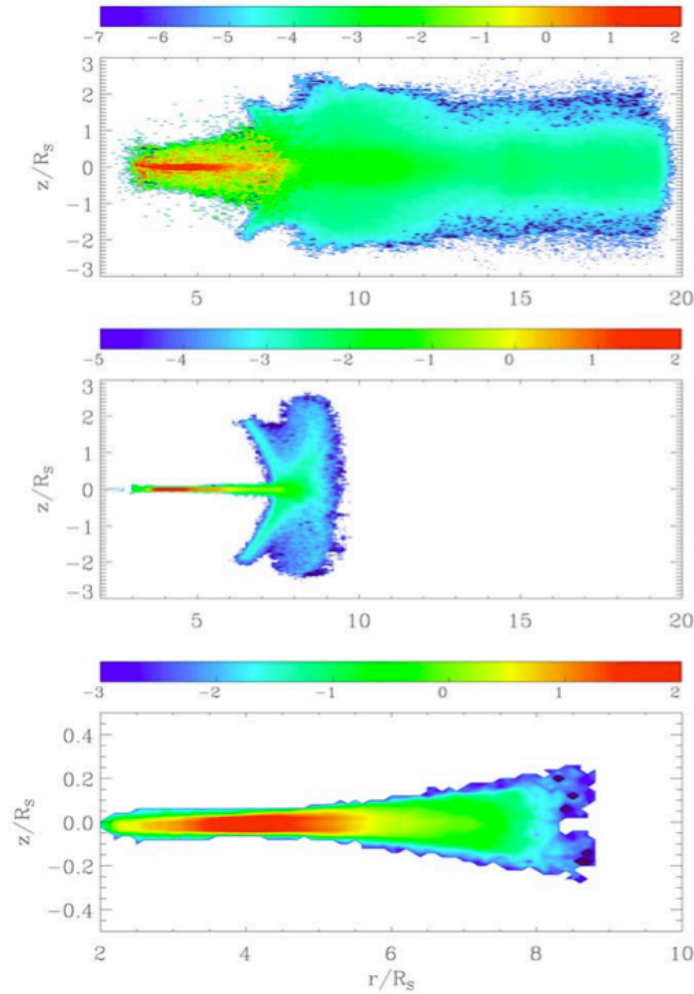


Figure 1.14: The azimuthally averaged density distribution of grains with radii: (top) $0.1 < r_\mu < 0.5$; (middle) $0.5 < r_\mu < 1$; and (bottom) $1 < r_\mu < 3$ [*Horányi et al.*, 2008].

density distributions in the E ring of various particle size ranges by numerical simulations [*Horányi et al.*, 2008]. All grains were released from Enceladus with an initial southward velocity of 100 m/s. The color scale is logarithmic, and in each case normalized to 100, corresponding to maximum number densities of 7; 1.2; and 0.3 m$^{-3}$. Particles with $r_\mu < 0.5$ populated the entire region between the outskirts of the A ring and the orbit of Titan, with a large vertical extent of about 0.5 $R_S$ at Enceladus, and reaching beyond

2.5 $R_S$ outside the orbit of Rhea. The spatial distribution of particles with radii $r_\mu < 1$ exhibited a structural change at $\sim$7 $R_S$, due to the transition from negative to positive charges. Particles with $r_\mu > 1$ remained confined to the E ring, and do not reach beyond $\sim$9 $R_S$.

*Wahlund et al.* [2009] observed the plasma parameters in the inner magnetosphere by the Cassini LP. They detected plasma densities, the electron temperature, the spacecraft potential corresponding to the dust surface potential, and the ion speeds during three orbits. Fig.1.15 and Fig.1.16 show the summary plot of the LP data during Rev17 and 26
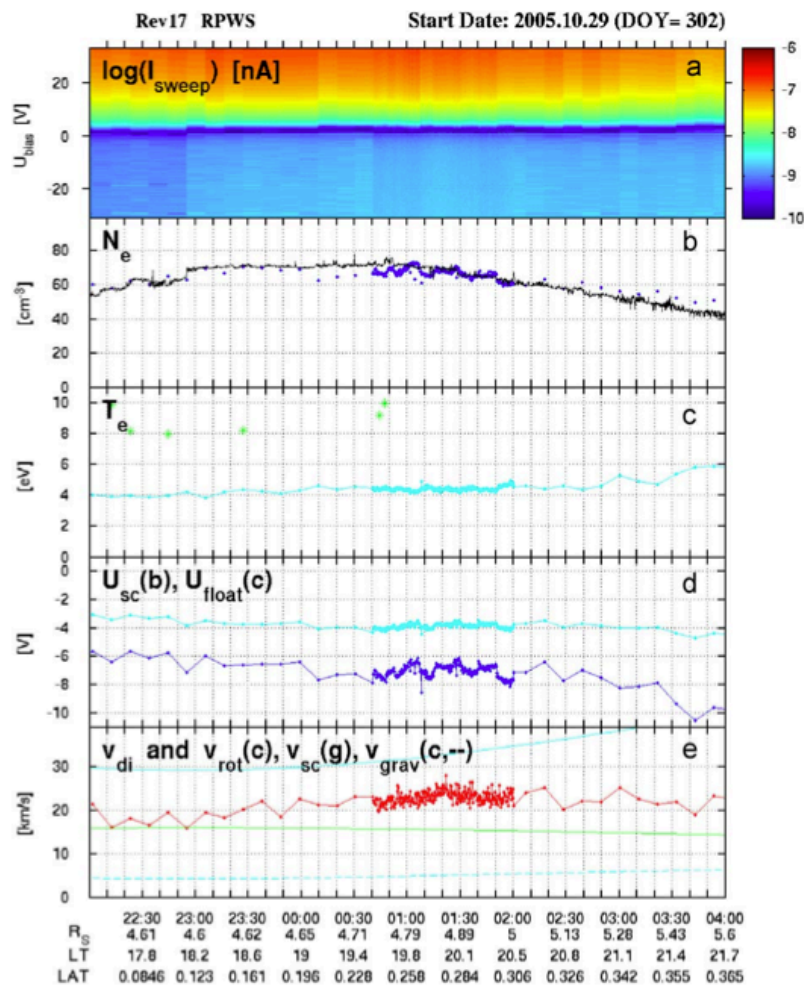


Figure 1.15: Summary plot of the Langmuir probe data around the $\delta n/n$ interferometer event during Rev17, 00:30-02:00 UT [*Wahlund et al.*, 2009].

[*Wahlund et al.*, 2009]. Panel a shows the raw sweep data showing the electron sampling
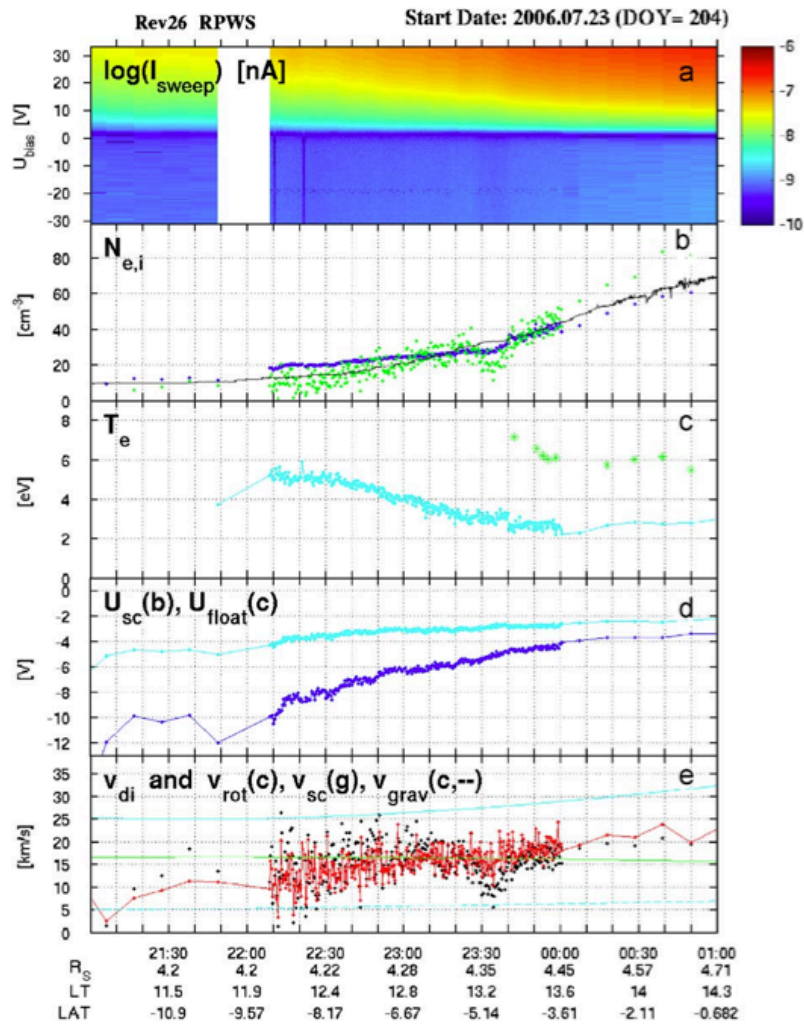
Figure 1.16: Summary plot of the Langmuir probe data around the $\delta n/n$ interferometer event during Rev26, 22:10-00:00 UT [*Wahlund et al.*, 2009].

(positive bias) and ion sampling (negative bias), and panel b shows the electron density from the LP (blue dots) and the upper hybrid frequency emissions (black lines), the estimating ion density assuming the ions hit the probe with the spacecraft speed (green line), and the ion density from the LP (red dots). The electron density was 60-70 cm$^{-3}$ during Rev 17, and significantly lower, 15-40 cm$^{-3}$ during Rev 26. Panel c shows two components of electron temperature (cold: cyan, hot: green) and they were estimated to be 4 eV (Rev 17) and 2-5 eV (Rev 26). Panel d shows the floating potential (cyan line) and the spacecraft potential (blue line). The spacecraft potential was -6 to -8 V (Rev 17) and -10 to -4 V (Rev 26). Dust grains in this region should be charged to similar potentials, and even though they consist of significantly different materials, they are exposed to the same charging mechanisms as the Cassini spacecraft [*Wahlund et al.*, 2009]. Panel e shows the ion drift speed (red line), the co-rotation speed (cyan solid line), the Keplerian speed (cyan dashed line), and the spacecraft speed (green line). The ion drift speed was between the co-rotation speed and the Keplerian speed, and it was consistent with the ion speed of *Holmberg et al.* [2012].

Fig.1.17-Fig.1.19 shows the LP thermal plasma characteristics from E02 to E06 encounters [*Wahlund et al.*, 2009; *Morooka et al.*, 2011]. Every flyby showed that the ion density was increasing and the electron density was decreasing when Cassini approached Enceladus. The ratio of the electron density to the ion density was about 0.4 during E02 encounter and it became less than 0.1 for E03-E06 encounters. They suggested that a large amount of dusts was existence around E ring region and most of dusts were charging negatively. On the other hand, the ion speeds were less than the ideal co-rotation speed in E02-E06 encounters, and it was almost the Keplerian speed around the closest approach. *Holmberg et al.* [2012] also investigated the ion speed in the inner magnetosphere, and the ion speed was between the co-rotation speed and the Keplerian speed. From above results *Wahlund et al.* [2009], *Morooka et al.* [2011] and *Holmberg et al.* [2012] proposed that the ion is affected by the charged dust, and thus the ion speed is less than the ideal co-rotation speed by the dust-plasma interaction.
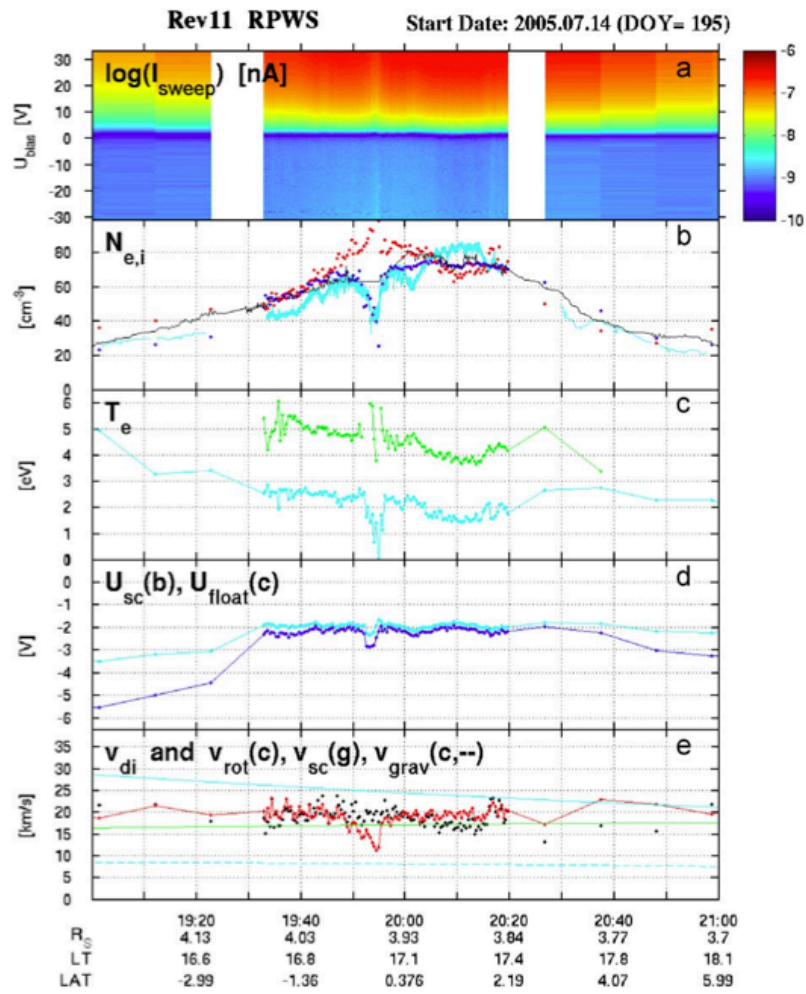
Figure 1.17: Summary plot of the Langmuir probe data around the $\delta n/n$ interferometer event during E02 flyby [*Wahlund et al.*, 2009].
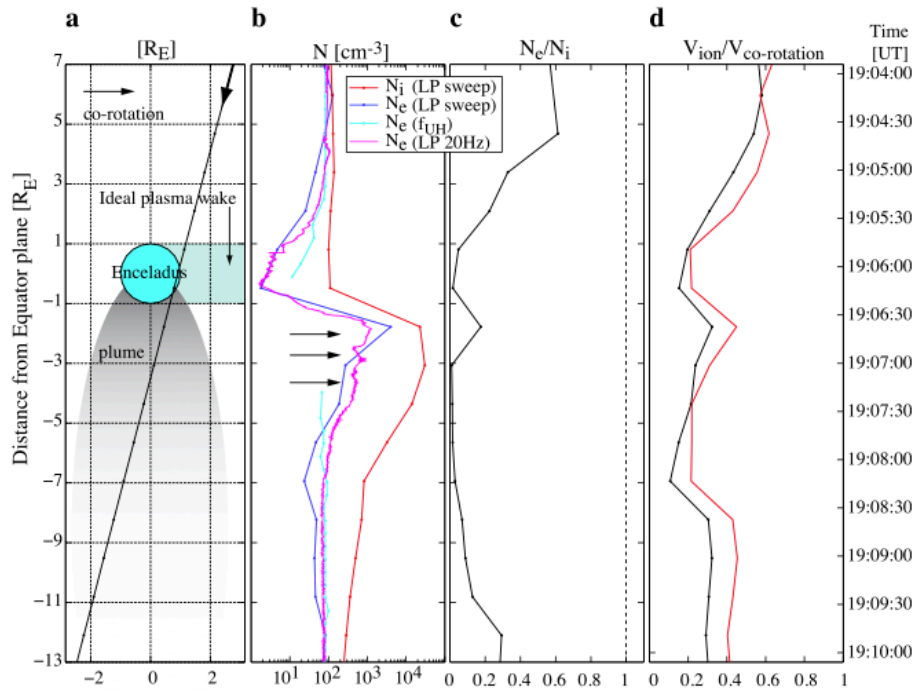
Figure 1.18: Flyby geometry and derived cold plasma parameters of the Enceladus E03 encounter [*Morooka et al.*, 2011].
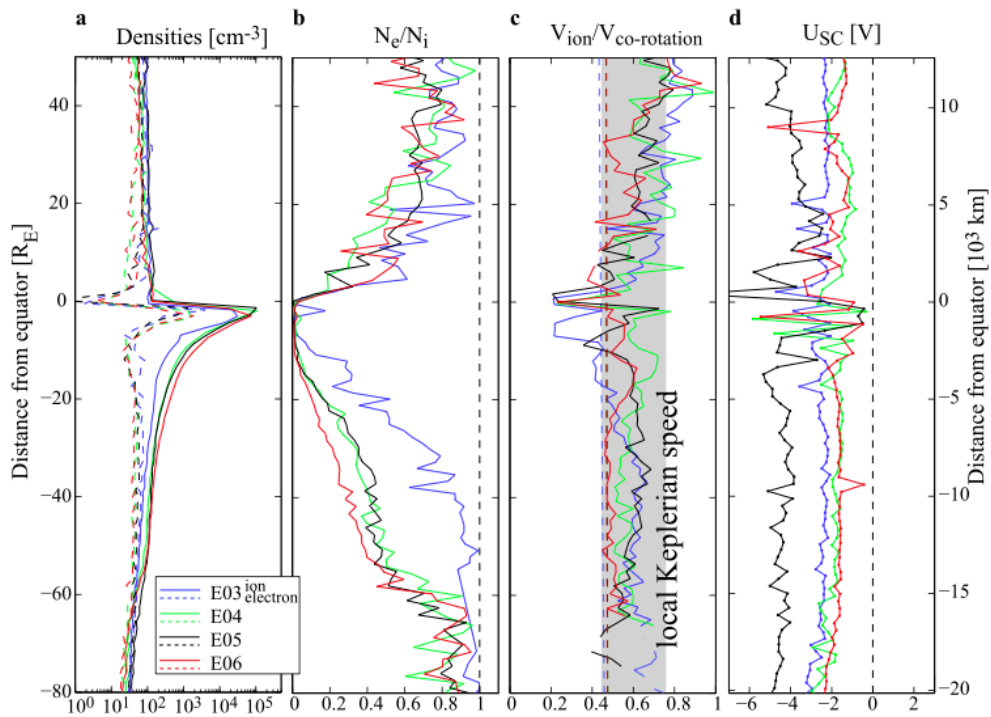


Figure 1.19: Plasma disk characteristics around a wide region around the E ring and Enceladus. The four Enceladus encounters E03-E06 had similar trajectories past the moon, and the cold plasma parameters have similar consistent characteristics [*Morooka et al.*, 2011].

# 1.3 Cassini

Cassini was launched from Cape Canaveral on 15 October 1997, and the weight is 2125 kg. Instruments onboard Cassini are classified in terms of three principal instruments, which are the optical remote sensing, the electric-magnetic field, particles and wave observations, and the microwave remote sensing.

- Optical remote sensing

    - Composite Infrared Spectrometer (CIRS)

    - Imaging Science Subsystem (ISS)

    - Ultraviolet Imaging Spectrograph (UVIS)

    - Visible and Infrared Mapping Spectrometer (VIMS)

- Electric-magnetic field, particles and wave observation

    - Cassini Plasma Spectrometer (CAPS)

    - Cosmic Dust Analyzer (CDA)

    - Ion and Neutral Mass Spectrometer (INMS)

    - Magnetometer (MAG)

    - Magnetospheric Imaging Instrument (MIMI)

    - Radio and Plasma Wave Science (RPWS)

- Microwave remote sensing

    - Radar

    - Radio Science (RSS)

Cassini made a flyby of Jupiter on 30 December 2000 and was inserted in Saturn's orbit on 1 July 2004.
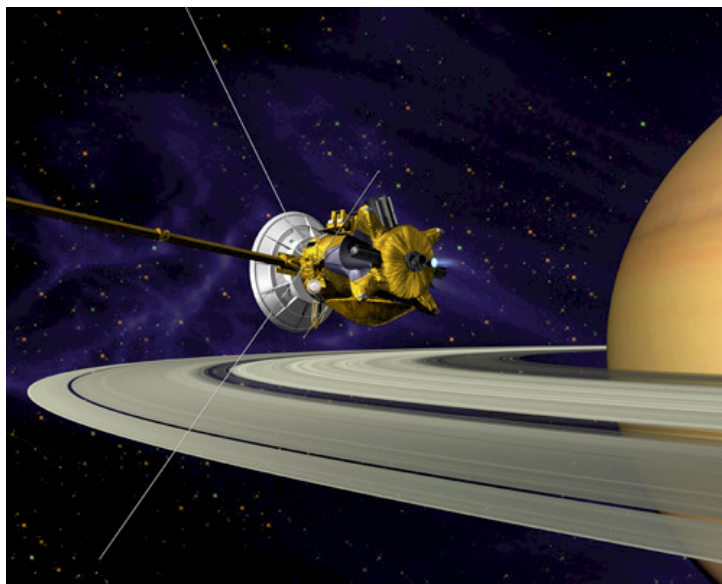
Figure 1.20: Cassini available at http://saturn.jpl.nasa.gov/photos/ [Credit: *NASA/JPL/Space Science Institute*].

# 1.4    Structure of this thesis

The plasma environment in Saturn's ionosphere and the dust and plasma environment in the inner magnetosphere was reviewed in previous sections. Saturn's inner magnetosphere in our solar system is interesting for the plasma and dust interaction. In our earth's magnetosphere, the dust is provided from the moon. However, the dust doesn't affect mostly the magnetospheric plasma due to the small amount of dust compared to Jupiter and Saturn.

*Wahlund et al.* [2009] and *Morooka et al.* [2011] suggested the dust-plasma interaction in Saturn's inner magnetosphere from the observation of cold plasma characteristics. However, it is difficult to clarify the dust-plasma interaction with only observations. The author tried to clarify the dust-plasma interaction in the inner magnetosphere from the analyses of the cold plasma data in the Enceladus plume and the numerical model in the inner magnetosphere and ionosphere.

In this thesis, the physics of dusty plasma in Saturn's system is mainly treated. The dusty plasma distribution of the Enceladus plume is shown in Section 2. The occurring condition of the dust-plasma interaction in the inner magnetosphere is shown in Section 3, the relationship of the dusty plasma with the ionospheric plasma is discussed in Section 4 and 5, and the conclusions are shown in Section 6.

# Chapter 2

# Enceladus plume observed by Cassini RPWS/LP

## 2.1  Introduction

The Enceladus' cryovolcanos near the south pole form the plume which is composed of the water vapor and ice dust [e.g., *Porco et al.*, 2006; *Spahn et al.*, 2006; *Waite et al.*, 2006]. The dust and the neutral gases expelled from Enceladus are considered as a main source of the E ring and the Enceladus torus [*Horányi et al.*, 2004; *Kurth et al.*, 2006; *Kempf et al.*, 2008], and after the ionization by the solar EUV and the charge exchanges they become a plasma source of the Saturn's magnetosphere [*Smith et al.*, 2010]. An interesting feature is that the dust grains of the plume are negatively charged [e.g., *Horányi et al.*, 2004] and their kinetics is electromagnetically coupled to the ambient plasma [*Wahlund et al.*, 2009; *Farrell et al.*, 2009; *Shafiq et al.*, 2011; *Morooka et al.*, 2011]. A large amount of the electrons are attached to the small grains and the dust plays an important role in plasma as a negative charge carrier. The situation is so called "the dusty plasma" [e.g., *Fortov et al.*, 2005] and possibly affects the electrodynamics of the extended plasma disk of the Kronian magnetosphere [*Holmberg et al.*, 2012; *Sakai et al.*, 2013].

The Cassini Radio Plasma Wave Science (RPWS) Langmuir Probe (LP) observations of several Enceladus flybys have been analyzed to investigate the horizontal and vertical characteristics of the dust and ion properties of the Enceladus' plume. *Morooka et al.*

[2011] used the data from the four Enceladus flybys performed in 2008 (E03, 04, 05, and 06) and showed the altitudinal profile of the electron and the ion densities, which were consistent in all flybys. The ion density became the maximum value of $10^5$ cm$^{-3}$ at the altitude of 0.8 R$_E$ from the south pole and gradually decreased with increasing the altitudes. Near the plume, a significant amount of the electron density has been missing ($n_e/n_i \ll 0.1$, where $n_e$ is electron density and $n_i$ is ion density). The ion velocity was slower than the ideal co-rotation speed and became close to the Keplerian speed, which indicates a strong electromagnetic coupling of the dust and the plasma. They suggested that the most of the negative charges are carried by the small sized ($< 0.1\mu$m) grains that are unable to be observed by the dust detector (CDA) [*Kempf et al.*, 2008]. *Shafiq et al.* [2011] estimated the plume dust density by using the electrons and ion densities obtained by the LP during the E03 flyby and showed that the total density of the negatively charged dust grains can be up to 100 cm$^{-3}$ if one assumes a certain dust size distribution of 30 nm to 10 $\mu$m. The observation of the Cassini Plasma Spectrometer (CAPS) / Electron Spectrometer (ELS) actually supported the existence of the negative/positive dust grains of small (a few nm) size [*Hill et al.*, 2012].

Several more flybys (E07, 08, 11, 17 and 18) are used and our results are compared with the plasma parameters reported by *Morooka et al.* [2011]. In the following sections, the Langmuir probe analysis method to derive the plasma parameters is described in Section 2. The obtained plasma parameters are shown in Section 3, the derived dust and plasma characteristics of the plume are discussed in Section 4, and our results are concluded in Section 5.

## 2.2   RPWS/LP analysis methods

The RPWS/LP instrument onboard the Cassini spacecraft is used and the thermal plasma and dust characteristics are observed. A full description of the RPWS instrument can be found in *Gurnett et al.* [2004]. The RPWS/LP consists of a titanium sphere, 5 cm in diameter, with a titanium nitride coating and is situated 1.5 m from the spacecraft main

body (Fig.2.1). The LP instrument can measure the current generated from the attracted plasma particles by sweeping the probe-biased voltages normally between -32 and 32 V. One sweep takes less than 0.25 s and performed every 24 s during the flybys used in this study.
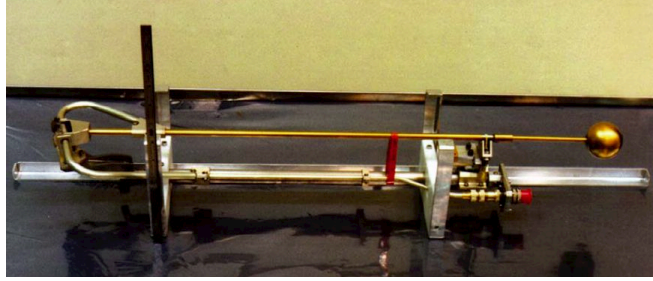


Figure 2.1: Cassini RPWS/LP [*Gurnett et al.*, 2004].

The electron parameters are based on a three-electron component theoretical fit to the positive LP voltage sweeps. One electron component corresponds to the spacecraft photoelectrons, while the others give the values of the electrons in the ambient plasma. The electron current can be usually expressed by an Orbital Motion Limited (OML) approximation [e.g., *Mott-Smith and Langmuir*, 1926], however, the sheath theory [*Bettinger and Walker*, 1965] is also considered in the analysis for the region where the Debye length can be small compare to the probe size. The electron current can at times be written as

$$I_e = I_{e0} \left(1 - \chi_e\right) \tag{2.1}$$

where

$$I_{e0} = -A_{LP} n_e q_e \sqrt{\frac{k_B T_e}{2 \pi m_e}} \tag{2.2}$$

is the random current, $A_{LP}$ is the probe area, $n_e$ is the electron density, $q_e$ is the electron charge, $k_B$ is the Boltzmann constant, $T_e$ is the electron temperature, $m_e$ is the mass of electron and

$$\chi_e = \frac{q_e \left(U_{bias} + U_1\right)}{k_B T_e} \tag{2.3}$$
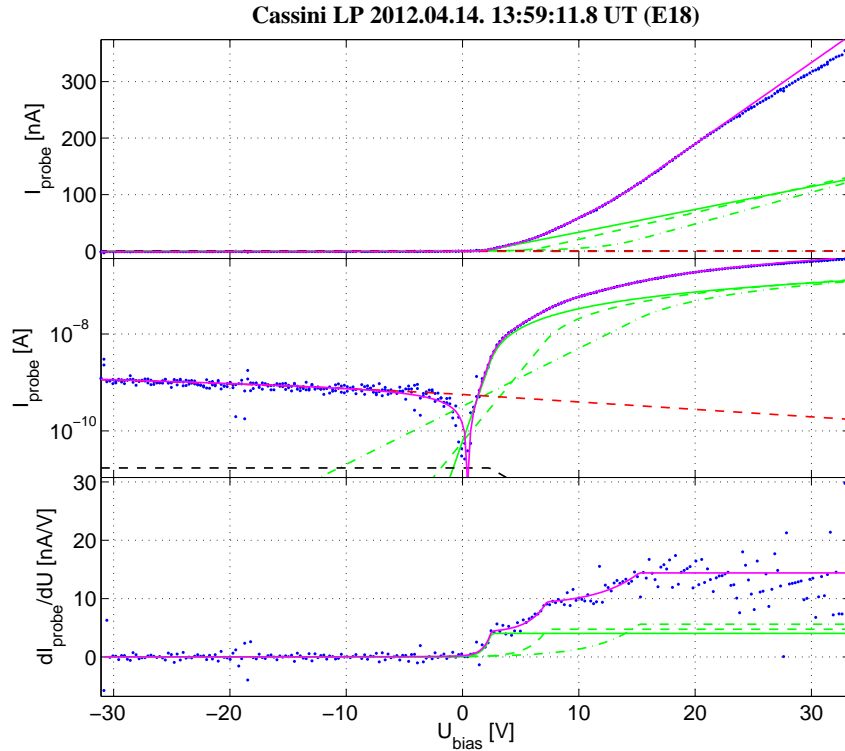
Figure 2.2: Current-voltage characteristics of a bias voltage sweep of the LP obtained during E18. The same data are shown in linear (panel a), absolute logarithmic (panel b), and panel c shows the derivative of the current. Blue dots are the LP data. The three electron populations are used to fit the positive bias side (green lines). Red dashed line shows the fitted ion current, and black dashed line shows photoelectron current from the probe. Magenta line shows the total theoretical current fitted to the data.

where $U_{bias}$ is the applied bias voltage and $U_1$ is the spacecraft potential (in case of spacecraft photoelectrons), or the characteristic potential of the electron population in the plasma (in case of ambient plasma electrons). $k_B T_e \gg m_e v_e^2 / 2$ is assumed and the electron current is rewritten as

$$I_e \approx I_{e0} \left[ 1 - \frac{q_e (U_{bias} + U_1)}{k_B T_e} \right] \qquad (2.4)$$

Fig.2.2 shows an example of a voltage sweep from E18 with a superimposed theoretical fit (magenta line). The same data is represented in linear (panel a), logarithmic (panel b) and the derivative ($dI/dU$, panel c).

The negative voltage part gives information on the ion drift speed [e.g., *Fahleson et al.*, 1974; *Holmberg et al.*, 2012], ion number density, average ion mass and integrated solar

EUV intensity. The ion current is given by

$$I_i = I_{i0} \left( 1 + \chi_i \right) \qquad (2.5)$$

where $I_{i0}$ is the random current. $k_B T_i \ll m_i v_i^2 / 2$ is assumed and the random current is written as

$$I_{i0} = -A_{LP} n_i q_i \frac{|v_i|}{4} \qquad (2.6)$$

and

$$\chi_i = \frac{q_i \left( U_{bias} + U_1 \right)}{m_i v_i^2 / 2} \qquad (2.7)$$

where $n_i$ is the ion density, $q_i$ is the ion charge, $v_i$ is the ion velocity and $m_i$ is the ion mass. If $b$ is defined as

$$b = - \left[ \frac{\partial I_i}{\partial U} \right] = - \frac{I_{i0} q_i}{\frac{m_i v_i^2}{2}}, \qquad (2.8)$$

it is possible to infer the ion density and velocity from the following proportionalities:

$$-I_{i0} b \propto n_i^2, \qquad (2.9)$$

$$-I_{i0} / b \propto v_i^2. \qquad (2.10)$$

## 2.3 Observations

### 2.3.1 Cassini trajectories

Five (E07, E08, E11, E17 and E18) encounters that are occurred in 2009, 2011 and 2012 (see Table 2.1) has been analyzed. During these flybys, Cassini passed across the plume in different altitudes from the surface. Thus, comparing these orbits makes possible to determine the vertical structure of the dust and plasma of the Enceladus plume. Fig.2.3 shows the trajectories of the Cassini flybys, plotted in the X-Y (panel a) and X-Z (panel b) planes of the Enceladus co-rotation coordinate system. In this system the X points the
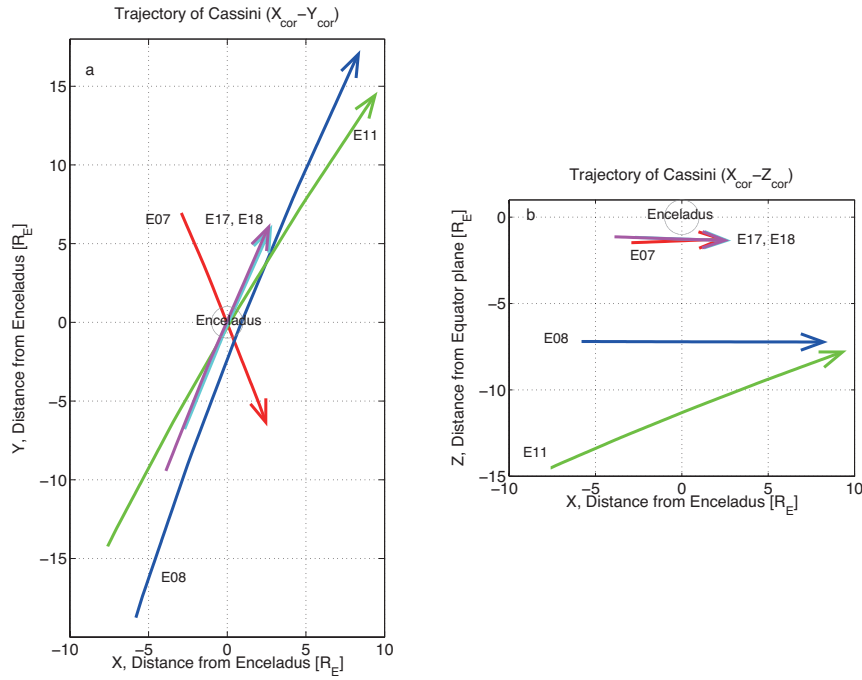
Figure 2.3: Cassini trajectories in the Enceladus co-rotation coordinate. Positive direction of X is the ideal co-rotation direction and Y points Saturn. Panel a shows in the X-Y plane and panel b is in the X-Z plane. Red line is E07, blue is E08, green is E11, cyan is E17 and magenta is E18, respectively.

ideal co-rotational direction of the plasma flow, Y points the planet, and the Z is fixed so that it completes the right hand orthogonal set. Enceladus radii $R_E$ is 252 km here. The Cassini traveled across the plume at Z = -1.3 $R_E$ during E07, E17 and E18, middle altitudes at Z = -7.3 $R_E$ in E08, and high altitudes at Z = -11 $R_E$ in E11.

Table 2.1: The altitude of plume crossings and time of the closest approach.

| Enceladus flybys | The distance from equatorial plane, -Z [$R_E$] | Time of the closet approach (UT) |
|---|---|---|
| E07 | 1.37 | 07:42, 02 November 2009 |
| E08 | 7.26 | 02:10, 21 November 2009 |
| E11 | 11.04 | 22:31, 13 August 2010 |
| E17 | 1.27 | 18:30, 27 March 2012 |
| E18 | 1.27 | 14:02, 14 April 2012 |

## 2.3.2  Low altitudes results

Fig.2.4 shows the plasma parameters in E07 (from 07:39:03UT to 07:44:57UT, 2nd November 2009), E17 (18:27:08UT to 18:32:52 UT, 27th March 2012), and E18 (13:58:46UT to 14:04:30UT, 14th April 2012). The obtained parameters are plotted along the ideal co-rotating direction, X. Among the analyzed five flybys, these three orbits had the closest approaches (CA) in low altitudes at Z = -1.3 $R_E$ ($\sim$99 km). The distance to Enceladus for each flyby is shown in Table 2.1. Panel a of Fig.2.4 shows an examples of the LP sweep currents. One can see that the ion current (negative bias voltage side) increases significantly near the closest approach (07:41:50 UT).

Panel b shows the ion (red, blue and green lines) and the electron densities (magenta, cyan and yellow lines) derived from the LP sweeps. In the background plasma disk region (X < −0.5, X $\gtrsim$ 1$R_E$) the ion density was observed to be constant ($\sim$50 cm$^{-3}$). The ion density has increased to $\sim$10$^4$ cm$^{-3}$ at X < |0.5|$R_E$, and this high ion density region is regarded as the plume (gray hatch). The plume size was about 1.5 $R_E$ in X at Z = -1.3 $R_E$. During this period, one can notice that the electron density is smaller than the ion density, and the density ratio of the electron and the ion ($n_e/n_i$) at the CA was about 10$^{-2}$ (Panel c). The electron density depletion can be due to the electron attachment to the dust as suggested by the previous observations [*Farrell et al.*, 2009; *Wahlund et al.*, 2009; *Morooka et al.*, 2011].

The electron temperature (panel d) was between 1 and 2 eV outside the plume as shown by *Wahlund et al.* [2009] and *Gustafsson and Wahlund* [2010]. It decreased as the spacecraft approaches to the plume, and was 1 eV or less. The temperature started to increase into the plume and became 2-5 eV at the CA. This might be due to the photoelectron escaped from plume gas by solar radiation. The temperature of the photoelectron would be about 10 eV [*Cravens et al.*, 2011] and the temperature gradually decreases by particle collisions. This could have caught the photoelectron that the temperature decreased slightly by collisions.
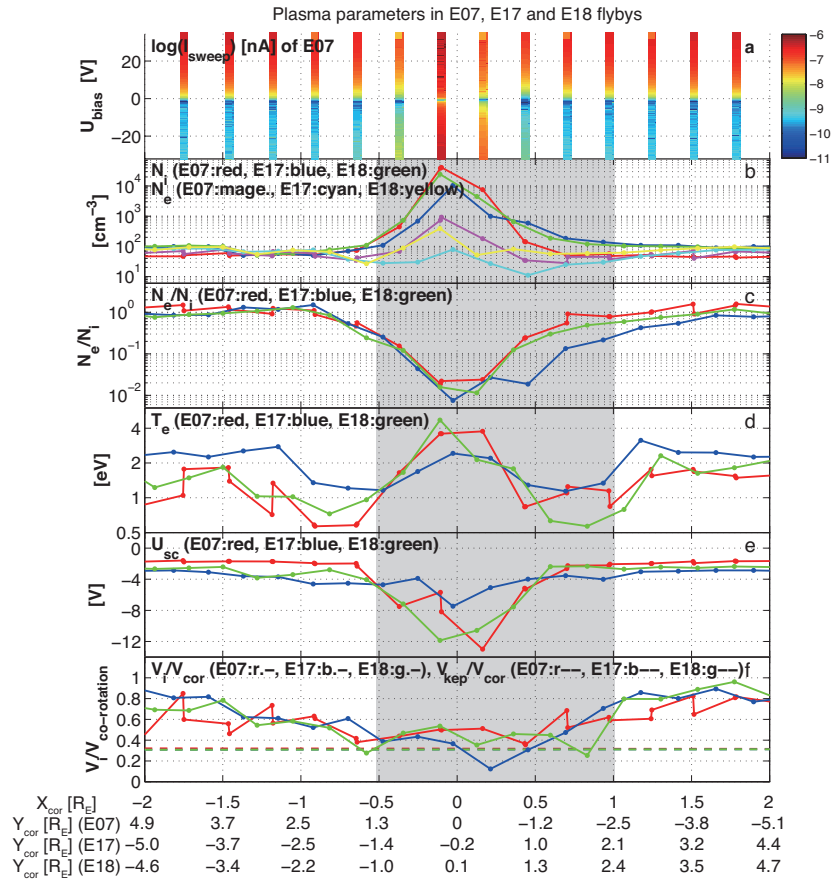
Figure 2.4: The plasma parameters near Enceladus during E07, E17 and E18 encounters. The gray hatch shows the identified plume region. (a) The raw sweep data showing the electron (positive bias) and ion (negative bias) currents of E07. (b) Ion and electron densities derived from the LP. The ion densities are shown in red (E07), blue (E17) and green (E18) lines. The electron densities are shown in magenta (E07), cyan (E17) and yellow (E18) lines. (c) The density ratio of the electron to the ion. Red is E07, blue is E17, and green is E18. (d) The electron temperature. The colors are same as panel c. (e) The spacecraft potential. The colors are in the same order as panel c. (f) The ion speed relative to the co-rotation speed (dot-dash lines). The dashed lines show the Keplerian speed relative to the co-rotation. The colors are same as panel c.

The spacecraft potential of the probe (panel e), which is regarded as the proxy to the dust potential, was about -2 V outside the plume. The negative value of the spacecraft potential is consistent with the values of previous studies in the E ring [*Horányi et al.*, 2004; *Wahlund et al.*, 2009; *Morooka et al.*, 2011]. Inside the plume it was much less than -2 V and became about -10 V. It is indicated that a large amount of negative particles, which are electrons or negative dusts, are existence near the center of plume.

Panel f shows the ion speed relative to the ideal co-rotation speed. Note that the LP measured ion speeds are relative speed to the spacecraft. The co-rotation speed and Keplerian speed relative to the spacecraft were 23.6-25.0 km/s and 7.4-7.7 km/s, respectively during the flybys. The ion speeds were generally smaller than the co-rotation velocity during the whole observed region and have a trend that becomes close to the Keplerian speed (plotted in dashed line in panel f) as the spacecraft approaches to the moon. The ion speed outside the plume was consistent with the results by *Holmberg et al.* [2012] showing that the ion velocity was between the co-rotation and Keplerian in E ring.

### 2.3.3   High altitudes results

Fig.2.5 shows the results for E08 (from 01:57:04UT to 02:18:35UT, 21st November 2009) and E11 (from 22:20:09UT to 22:37:39UT, 13th August 2010) encounters. The obtained parameters are plotted with a format similar to Fig.2.4. These two orbits had the closest approaches in high altitudes at Z = -7.3 $R_E$ ($\sim$1500 km) and Z = -11.0 $R_E$ ($\sim$2500 km). The distance to Enceladus for each flyby is also shown in Table 2.1.

Panel a of Fig.2.5 shows an examples of the LP sweep currents taken from E08. One can see that the ion current (negative bias voltage side) gradually increases from about two minutes before the closest approach (02:08:00 UT). The high ion densities region of the plume were observed at -0.5 $R_E$ < X < 2 $R_E$ (panel b, gray hatch) which is broader than that in low altitude case (Fig.2.4). For both encounters the ion densities outside the plume were $\sim$50 cm$^{-3}$. The ion density increases near the moon and become $\sim$120 cm$^{-3}$ (more than twice as the one outside the plume). The plume size was about 3 $R_E$ in X at
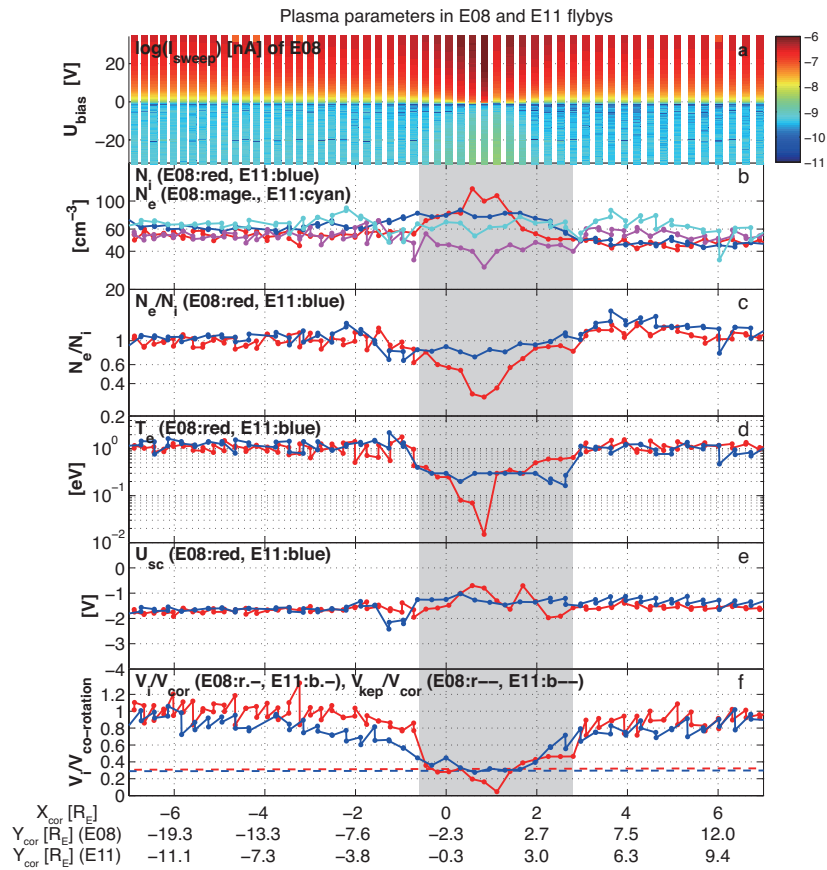
Figure 2.5: The plasma parameters near Enceladus during E08 and E11 encounters. Each panel format is the same as Fig.2.4. Panel a is the raw sweep data of E08. The red (magenta) line shows E08 and the blue (cyan) line shows E11.

Z = -7.3 $R_E$. The ratio $n_e/n_i$ was found to be about 0.4 in the plume, while it was almost 1 outside the plume (panel c).

The spacecraft potential was negative about -1 V during E08 and E11. The ion speed was nearly the co-rotation speed outside the plume and close to Keplerian speed in the plume.

## 2.4   Discussion

Five Enceladus encounters that passed across the Enceladus southern plume in different altitudes was analyzed to investigate the plume's plasma structures. The ion density near Enceladus was generally higher than the ion densities in the background plasma disk. On the other hand the electron density was about 1% of the ion densities near Enceladus. The observed electron was about a few eV in the plasma disk, and it increased to about 4 eV near Enceladus. The spacecraft potential of the LP was generally negative in the plasma disk and near Enceladus. The ion speed was nearly Keplerian speed near Enceladus. All the above characteristics were consistent with the previous observations near Enceladus and the E ring [*Wahlund et al.*, 2009; *Morooka et al.*, 2011] indicating the existence of the small charged dust grains and the collective coupling between the charged dust and plasma. In addition to the above results, several other different plasma characteristics of the plume were found. In the following discussion the height dependence of the plume plasma, the plume size, and some other dust and plasma characteristics obtained in this study will be described.

### 2.4.1   Plasma height dependence of the plume

As Fig.2.4 and Fig.2.5, ion densities of the background plasma disk were averagely 50 cm$^{-3}$. Therefore, the plume is defined as the region with the ion density larger than 50 cm$^{-3}$ and estimated the size and the height dependence of the plume.

At Z = -1.3 $R_E$, the plume was centered at [X, Y] = [0, 0] and its diameter was about 3.8 $R_E$ (Fig.2.4). The plume diameter increases to ∼5.6 $R_E$ at Z = -7.3 $R_E$ and ∼8.4 $R_E$ at Z = -11 $R_E$. On the other hand, the plume was not symmetric to the axis of [X, Y] = [0, 0] all the time. At Z = -7.3 $R_E$ the plume region starts at X = -0.5 $R_E$ and ends at X = 2.0 $R_E$, and Z = -11 $R_E$ the plume starts at X = -0.5 $R_E$ and ends at X = 2.8 $R_E$ (Fig.2.5).

Fig.2.6 shows the summary of the plume location obtained in this study. The ion densities are plotted along the Cassini trajectories in X-Z (panel a) and X-Y (panel b) planes of the Enceladus co-rotation coordinate system. A gray hatch shows the identified plume region. The blue and pink boxes in panel b are the observed plume at low and high altitudes, respectively. It is clear that the plume extends to 3 $R_E$ toward the downstream at higher altitudes. This may be indicating that the plume ions are affected by the co-rotational electric field and drifting in the direction.

Inside the plume the ions had densities maxima around the center of the plume for all flyby. Fig.2.7 shows the altitude dependence of the average dust and plasma densities near the plume center. Overall, it was obtained that the plume characteristics become weaker as the distance from Enceladus' surface increase. The ion density was about $10^4$ cm$^{-3}$ at low altitudes (Z = -1.3 $R_E$) and decreased to about 100 cm$^{-3}$ at Z = -7.3 $R_E$, and became 80 cm$^{-3}$ at Z = -11 $R_E$ (red line in panel a). The ratio $n_e/n_i$ was about $10^{-2}$ at the low altitudes while it increases up to 0.3-0.7 at high altitudes (panel b). The electron temperature was about 4 eV at low altitudes because of the photoelectron escaped from plume gas by solar radiation. On the other hand, it decreased to about 0.1 eV at high altitudes. It could be since the temperature gradually decreases by particle collisions. The spacecraft potential was about -10 V into the plume at low altitudes, and it increased to a few V negative at high altitudes. At low altitudes a large amount of negative particles could be existence near the center of plume. The ion speed didn't have the vertical dependences and it was near Keplerian speed inside the plume.

From this study, the plume has found down to Z = -12 $R_E$. The observation from the other flybys showed that the plume could extend to Z = -7.3 $R_E$ [*Morooka et al.*, 2011].
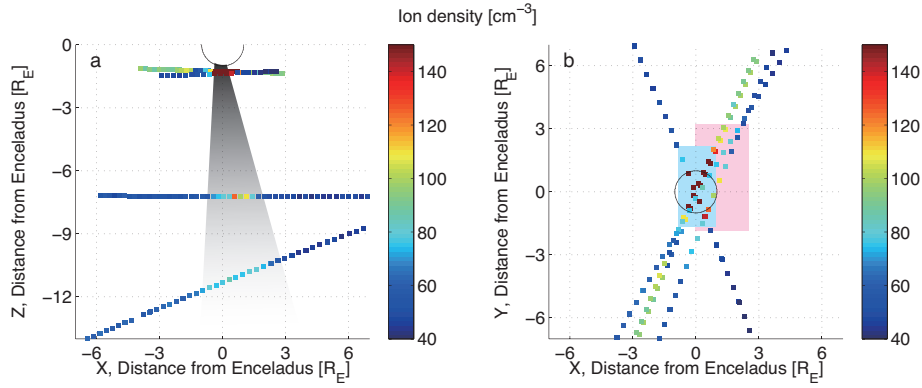
Figure 2.6: The schematic picture of the plume location obtained in this study. The ion densities are shown along the Cassini trajectories of E07, E08, E11, E17 and E18 in the Enceladus co-rotation coordinate. Panel a shows in the X-Z plane and panel b shows in the X-Y plane. (a) The black hatch shows the identified plume region. (b) The blue and pink boxes are the observed plume at low and high altitudes, respectively.

Comparing the parameters obtained in this study and the ones in the previous studies (E03, E04, E05, and E06, see Figure 5 in *Morooka et al.*, [2011]), the ion densities in this study was an order of magnitude smaller than the ion densities observed during 2008. One reason could be the time dependence of the neutral production of the plume. It is reported that the neutral water-vapor density of the plume in E03 measured by the Cassini Ion and Neutral Mass Spectrometer (INMS) was four times larger than the neutral density in E05. The neutral density in E07 was found to be similar to the neutral density in E03 [*Dong et al.*, 2011].
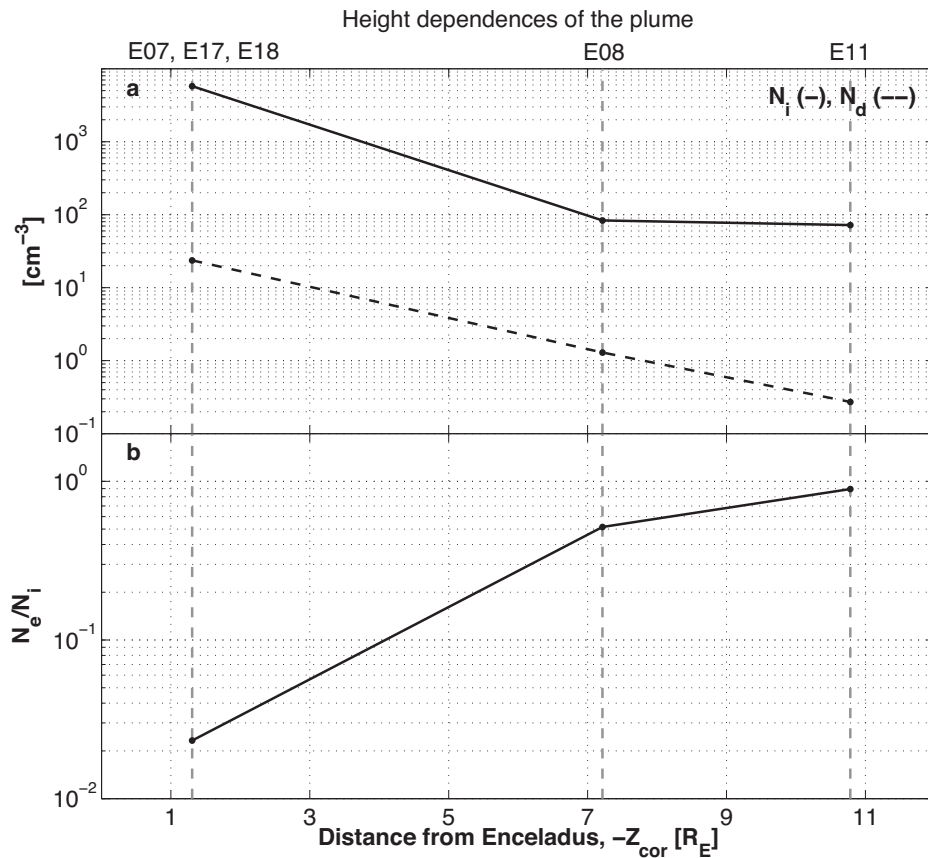
Figure 2.7: The height dependences of the averaged dust and plasma densities in the plume center. The average density was calculated from each density in the plume. (a) The ion (red) and dust (blue) density. (b) The ratio of the electron density to the ion density.

## 2.4.2   Dust density in the plume

Using the parameters obtained by the LP analysis (the electron and ion densities, the spacecraft potential) and a model of the dust size distribution, the dust densities are able to be estimated [*Yaroshenko et al.*, 2009]. The dust density $n_d$ is given by

$$n_d = \frac{e\,(n_i - n_e)}{4\pi\varepsilon_0 U_{SC} r_{min}} \left(\frac{2 - \mu}{1 - \mu}\right) \tag{2.11}$$

where $e$ is the charge quantity of ions and electrons; $\mu$ is the spectral index functioning and $r_{min}$ is the minimum of dust radius. $\mu$ is used as 4 and $r_{min}$ as 30 nm. The blue line in panel a of Fig.2.7 shows the calculated average dust density in the plume. One can see that the dust densities decrease as increasing the altitudes. The dust density was about 20 cm$^{-3}$ at Z = -1.3 R$_E$. It decreased to about 1 cm$^{-3}$ at Z = -7.3 R$_E$ and became 0.3 cm$^{-3}$ at Z = -11 R$_E$.

Comparing the nano-sized grain's density observed by the CAPS/ELS and Ion Beam Spectrometer (IBS), the LP estimated charged dust densities were larger than the densities reported by *Hill et al.* [2012]. This indicates that a large amount of the negative charge carrier could be the dust with size between a few nm and sub $\mu$m. The CAPS can only measure the nano-sized dust [*Jones et al.*, 2009].

## 2.5   Conclusion

To investigate the structure and characteristics of the plasma properties of the Enceladus plume, the Cassini RPWS/LP data of five flybys that across the plume in different altitudes were analyzed. The plume characteristics derived from this study are summarized as follows:

The horizontal diameter of the plume was about 3.8 R$_E$ at the low altitudes (Z = -1.3 R$_E$) and increased to about 8.4 R$_E$ at high altitudes (Z = -11 R$_E$). The plume extends at least to 12 R$_E$ southward. At the high altitudes the plume extended to about 3 R$_E$ in the downstream. This may be indicating that the plume ions are affected by the co-rotation

electric field and drifting in the direction.

Outside the plume, both the electron and the ion densities were about 50 cm$^{-3}$. The ion densities were generally higher in the plume than the background plasma. They are two orders of magnitudes larger (the maximum was about 10$^4$ cm$^{-3}$) than the background at low altitudes (Z = -1.3 R$_E$). At high altitudes above 7.3 R$_E$ they were only slightly higher than the outside plume plasma densities. The electron density was, on the other hand, smaller than the background plasma density and the ion density. The density ratio of the electron to the ion was especially small at low altitudes and became $n_e/n_i \sim 0.01$. This is consistent with the previous observations of the Enceladus plume indicating that the electrons are attached to the negatively charged dust grains [*Farrell et al.*, 2009; *Jones et al.*, 2009]. The dust density was estimated to be about 20 cm$^{-3}$ using the observed density differences of the electron and the ion and assuming a certain dust distribution with size of > 30 nm.

The electron temperature was a few eV outside the plume. At low altitudes it became hotter ($\sim$4 eV) in the plume, and it decreased to about 0.1 eV at higher altitudes. The hotter photoelectron escaped from the neutral gas of the plume was observed at low altitudes, and the electron cooled by collisions was found at high altitudes.

The dust surface potential was generally negative in whole observed region. It became much less than a few V negative at low altitudes. This could be since a large amount of negative charge carrier is existence near Enceladus. The ion speed was near Keplerian speed in the plume.

Comparing with the results from the earlier observations by *Morooka et al.* [2011] the observed parameters were different. The general plasma densities of the plume in this study were smaller than the densities obtained by *Morooka et al.* [2011]. This can be due to the temporal activity of the tiger stripe.

# Chapter 3

# Modeling of the inner magnetosphere

## 3.1   Introduction

Plasma in Saturn's magnetosphere is co-rotating due to the rapid rotation of the planet [e.g., *Blanc et al.*, 2005]. However, the magnetosphere can be slowed from the co-rotation speed due to, for instance, mass loadings [e.g., *Hill*, 1979; *Saur et al.*, 2004]. Past observations using the particle detectors on Voyager and Cassini showed that around 5 $R_S$ (1 $R_S$ = 60,268 km), the plasma speeds are almost the ideal co-rotation speed and gradually decrease to 70-80% of that speed at 7 $R_S$ [*Bridge et al.*, 1981, 1982; *Richardson*, 1986, 1998; *Wilson et al.*, 2008, 2009]. Observations using the Langmuir Probe (LP) on board the Cassini spacecraft showed that part of the ion bulk speeds are close to the Keplerian speed in Saturn's E ring [*Wahlund et al.*, 2009], which is consistent with the presence of small (nano to micro size) dust particles. These dust particles are negatively charged inside 7 $R_S$ and are expected to contribute to the electrodynamics of the plasma disk structure [*Horányi et al.*, 2004; *Kempf et al.*, 2008]. Near Enceladus, which is a major source of the E ring dust, the electron density is significantly less than the ion density and the ion speeds are near Keplerian within a large region [*Morooka et al.*, 2011]. The ion beam spectrometer of the Cassini Plasma Spectrometer (CAPS/IBS) on board Cassini also observed that the ions slow to 50-90% of the ideal co-rotation speed [*Thomsen et al.*,

2010].

In the latest observations by the LP, data collected from February 2005 to June 2010 (Rev 003-133) were used [*Holmberg et al.*, 2012]. They showed the ion speeds are much less than the ideal co-rotation speed in the inner magnetosphere. The speeds were 50-70% of the ideal co-rotation speed. As suggested by *Wahlund et al.* [2009], the charged dust particles in the E ring were related to the lower ion speeds. Some ion speeds were also smaller than the Keplerian speed around 4 $R_S$. This could happen if the ions were related to Enceladus [*Shafiq et al.*, 2011]. The ion speeds found here were less than those reported by *Wilson et al.* [2008] and *Thomsen et al.* [2010] from the CAPS data. *Wilson et al.* [2008] found ion speeds around 80% of the ideal co-rotation speed between 5 and 10 $R_S$, and *Thomsen et al.* [2010] found ion speeds of 50-90% of the ideal co-rotation speed. This could be owing to the difference in the measured particle energy range in measurement methods between the LP and the CAPS/IBS.

In this chapter, the results of modeling ion speeds in the inner magnetosphere by using a multi-species fluid model taking into account the dust-plasma interaction and mass loadings is reported.

## 3.2    Model

### 3.2.1    A multi-species fluid model

The ion and dust velocities are calculated by using a multi-species fluid model (i.e., protons, water group ions, charged dusts and electrons) to investigate the effect of dust on ion speed.

$$\frac{\partial \rho_k}{\partial t} + \nabla \cdot (\rho_k \boldsymbol{v}_k) = S_k - L_k, \tag{3.1}$$

$$\frac{\partial \rho_k \boldsymbol{v}_k}{\partial t} + \nabla \cdot (\rho_k \boldsymbol{v}_k \boldsymbol{v}_k) = n_k q_k \left( \boldsymbol{E} + \boldsymbol{v}_k \times \boldsymbol{B} \right) - \nabla p_k - \rho_k \boldsymbol{g}$$
$$- \sum_l \rho_k \nu_{kl} \left( \boldsymbol{v}_k - \boldsymbol{v}_l \right) + \sum_l S_{k,l} \boldsymbol{v}_l - L_k \boldsymbol{v}_k. \tag{3.2}$$

Here, subscript $k$ indicates proton $(p)$, water group ion $(w)$, dust $(d)$, or electron $(e)$; $\rho_k$ is $m_k n_k$; $\boldsymbol{v}_k$ is velocity; $m_k$ is mass; $q$ is charge quantity (i.e., $e$ is the charge quantity of ions and electrons, and $q_d$ is that of dust); $\boldsymbol{E}$ is the electrical field vector; $\boldsymbol{B}$ is the magnetic field vector; $\nu_{kl}$ is the general collision frequency considering collisions among the ions, dust, electrons, and neutral gases; where $n_k$ is the number density. The ion production rate is given by

$$S_{k,l} = m_s \kappa n_s n_l + m_k n_l \int_0^\infty \sigma_k F \, d\lambda, \tag{3.3}$$

where $\kappa$ is the reaction rate of the production, $\sigma_k$ is the scattering cross section, $F$ is the density of photons, and $\lambda$ is wavelength. The total ionization frequency of water group ions is

$$\int_0^\infty \sigma_k F \, d\lambda = 1.184 \times 10^{-8} \; [\mathrm{s}^{-1}], \tag{3.4}$$

which is converted to a Saturn value based on an Earth value [*Schunk and Nagy*, 2009]. The mass loading of dust is zero since it is negligibly small. The ion loss term is given by

$$L_{k,l} = m_k \alpha n_k n_l \tag{3.5}$$

where $\alpha$ is the reaction rate of the loss. Finally, from equations (3.1) and (3.2),

$$\rho_k \frac{\partial \boldsymbol{v}_k}{\partial t} + \rho_k \left( \boldsymbol{v}_k \cdot \nabla \right) \boldsymbol{v}_k = n_k q_k \left( \boldsymbol{E} + \boldsymbol{v}_k \times \boldsymbol{B} \right) - \nabla p_k - \rho_k \boldsymbol{g}$$
$$- \sum_l \rho_k \nu_{kl} \left( \boldsymbol{v}_k - \boldsymbol{v}_l \right) - \sum_l S_{k,l} \left( \boldsymbol{v}_k - \boldsymbol{v}_l \right) \tag{3.6}$$

can be obtained. The equation (3.6) is used for the ion speed calculations in the Saturn's inner magnetosphere. The ions generated by the charge exchange are $H^+$, $H_2O^+$, $H_3O^+$, $OH^+$ and $O^+$. The chemical equations and the reaction rates are listed in Table 3.1.

Table 3.1: Ion chemical reactions and rates used in this study.

| Reactions | Rates [m$^3$s$^{-1}$] | References |
|---|---|---|
| $H^+ + H_2O \rightarrow H + H_2O^+$ | $2.60 \times 10^{-15}$ | *Burger et al.* [2007]; *Lindsay et al.* [1997] |
| $O^+ + H_2O \rightarrow O + H_2O^+$ | $2.13 \times 10^{-15}$ | *Burger et al.* [2007]; *Dressler et al.* [2006] |
| $H_2O^+ + H_2O \rightarrow H_2O + H_2O^+$ | $5.54 \times 10^{-16}$ | *Burger et al.* [2007]; *Lishawa et al.* [1990] |
| $H_2O^+ + H_2O \rightarrow OH + H_3O^+$ | $3.97 \times 10^{-16}$ | *Burger et al.* [2007]; *Lishawa et al.* [1990] |
| $OH^+ + H_2O \rightarrow OH + H_2O^+$ | $5.54 \times 10^{-16}$ | *Burger et al.* [2007]; *Itikawa and Mason* [2005] |
| $H_2O + e \rightarrow H_2O^+ + 2e$ | | *Burger et al.* [2007]; *Itikawa and Mason* [2005] |
| $H_2O + e \rightarrow OH^+ + H + 2e$ | $10^{-18}$ (total) | *Burger et al.* [2007]; *Itikawa and Mason* [2005] |
| $H_2O + e \rightarrow H_2O^+ + 2e$ | | *Burger et al.* [2007]; *Itikawa and Mason* [2005] |
| $H_2O + e \rightarrow H^+ + OH + 2e$ | $10^{-22}$ | *Burger et al.* [2007]; *Itikawa and Mason* [2005] |

Collision frequencies are given by

$$\nu_{id} = n_d \left\{ 4\pi \left[ \frac{q_d e}{4\pi\varepsilon_0 m_i \left(|\boldsymbol{v}_i - \boldsymbol{v}_d|^2 + v_{thi}^2\right)} \right]^2 + \pi r_d^2 \right\} \sqrt{|\boldsymbol{v}_i - \boldsymbol{v}_d|^2 + v_{thi}^2}, \qquad (3.7)$$

$$\nu_{ed} = \frac{2\sqrt{2\pi}}{3} n_d v_{the} r_d^2 \left( \frac{e\phi_s}{k_B T_e} \right)^2 2\ln \left( \frac{2k_B T_e}{e\phi_s r_d} \lambda_D \right), \qquad (3.8)$$

$$\nu_{ei} = 54.5 \times 10^{-6} \frac{n_i}{T_i^{3/2}}, \qquad (3.9)$$

$$\nu_{in} = \left(2.6 \times 10^{-15}\right) \left(n_n + n_i\right) A^{-1/2}, \qquad (3.10)$$

$$\nu_{en} = \left(5.4 \times 10^{-16}\right) n_n T_e^{1/2}, \qquad (3.11)$$

$$\nu_{dn} = n_n \pi r_n^2 \sqrt{|\boldsymbol{v}_d - \boldsymbol{v}_n|^2 + v_{thd}^2}, \qquad (3.12)$$

$$\nu_{wp} = 1.27 \frac{\mu}{M_w} \frac{n_p}{T_i^{3/2}}, \qquad (3.13)$$

$$\nu_{kl} = \frac{m_l n_l}{m_k n_k} \nu_{lk}, \qquad (3.14)$$

where subscript $i$ identifies the component of protons and water group ions respectively, $r_d$ is the dust radius, $\phi_s$ is the dust surface potential, $v_{thi}$ is the ion thermal velocity, $v_{the}$ is the electron thermal velocity, $v_{thd}$ is the dust thermal velocity, $n_n$ is the neutral number density, $A$ is the mass of the neutral gas in atomic mass unit, $M_w$ is the mass of the water group ion in atomic mass units, $\mu$ is the reduced mass between the proton and the water group ion in atomic mass units, and $n_p$ is the proton number density. The model of $\nu_{ed}$ was introduced by *Khrapak et al.* [2004]. The Debye length of a dusty plasma is given by

$$\lambda_D = \sqrt{\frac{\varepsilon_0 k_B T_e}{n_e e^2}}. \qquad (3.15)$$

The magnetospheric electric fields are affected through the magnetosphere-ionosphere

coupling. The electric field $\boldsymbol{E}$ is given by

$$\Sigma_i \left( \boldsymbol{E}_{cor} - \boldsymbol{E} \right) = \boldsymbol{j} D, \tag{3.16}$$

where $\Sigma_i$ is the ionospheric Pedersen conductivity, $\boldsymbol{E}_{cor}$ is the co-rotational electric field, and $D$ is the thickness of the dust distribution in z-direction (Fig.3.1). $\boldsymbol{j}$ is the magnetospheric Pedersen current density given by

$$\boldsymbol{j} = en_p \boldsymbol{v}_p + en_w \boldsymbol{v}_w - en_e \boldsymbol{v}_e - q_d n_e \boldsymbol{v}_d \tag{3.17}$$
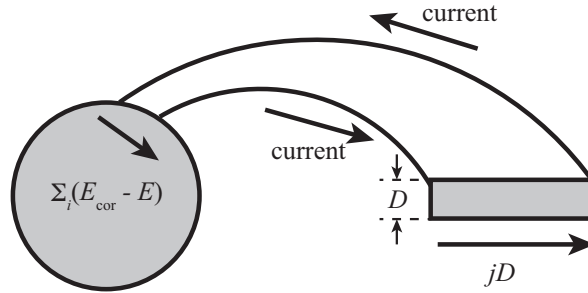


Figure 3.1: A cartoon of an electric circuit connecting between magnetosphere and ionosphere [*Sakai et al.*, 2013].

### 3.2.2 Parameters

Density distributions of electrons, protons, dust particles, and neutral particles are shown in Fig.3.2. The densities depend on the distance from Saturn ($R_S$). Black solid lines indicate electron density, black dashed lines indicate ion density, black dashed-dotted lines indicate proton density, grey solid lines indicate dust density, and grey dashed lines indicate neutral density in each panel. The density distributions of electrons were increasing with distance from Saturn inside 5 $R_S$ and were decreasing with distance from Saturn outside 5 $R_S$ [*Persoon et al.*, 2005, 2009]. The maximum densities for electrons are $4 \times 10^7$

m$^{-3}$ [*Persoon et al.*, 2005, 2009] at about 4 R$_S$. On the other hand, density distributions of neutral gases are decreasing with distance from Saturn. The maximum densities for neutrals are $6.5 \times 10^8$ m$^{-3}$ [*Smith et al.*, 2010] at 2 R$_S$. The dust density, $n_d$, is free parameters. The ion speeds are calculated in two cases: (a) $n_d = 3.2 \times 10^4$ m$^{-3}$, (b) $n_d = 6.4 \times 10^4$ m$^{-3}$ at 2 R$_S$. The number density of water group ion is derived from charge neutrality:

$$n_w = n_e + \frac{q_d}{e} n_d - n_p. \tag{3.18}$$
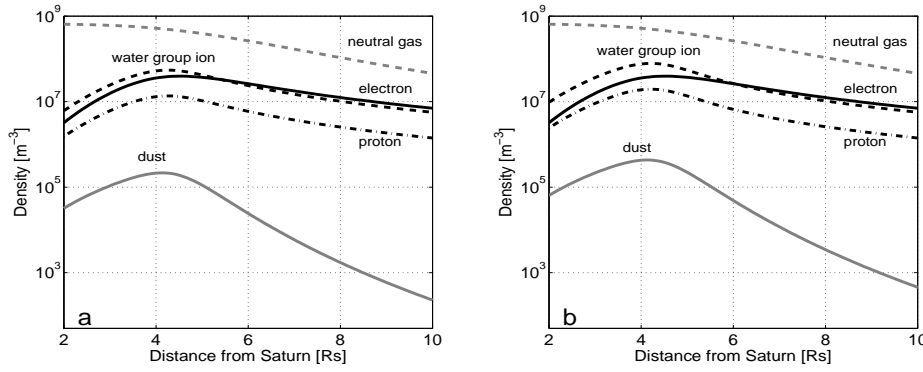


Figure 3.2: Density profiles. Black solid line indicates electron density, black dashed line indicates water group ion density, black dashed-dotted line indicates proton density, and grey solid line indicates dust density, and grey dashed line indicates neutral density. (a) $n_{d,r=2R_S} = 3.2 \times 10^4$ m$^{-3}$; (b) $n_{d,r=2R_S} = 6.4 \times 10^4$ m$^{-3}$ [reproduced from *Sakai et al.*, 2013].

The ratio of $n_p$ to $n_w$ is 20%. The thickness of the dust distribution, $D$, is used in three cases: $D = 1, 2$, and 3 R$_S$ (Table 3.2). The radius of dust is $r_d = 10^{-7}$ m. The Cosmic Dust Analyzer (CDA) can investigate the dust particles size of about 0.8 mm [*Kempf et al.*, 2008]. The smaller size and high-density dust was more important in electrodynamics than micro size and low-density dust. Therefore, 0.1 $\mu$m as the grain radius was used. The charged quantity of dust is

$$q_d = 4\pi\varepsilon_0 r_d \phi_s \ [\text{C}]. \tag{3.19}$$

Each thermal energy is 2 eV since newly created ions from e.g., photo-ionization would initially have a small energy [*Wahlund et al.*, 2009; *Gustafsson and Wahlund*, 2010], the

dust surface potential is -2 V [*Wahlund et al.*, 2005]. The equilibrium spacecraft potential with respect to plasma estimated using the LP includes components from cold and hot electrons as well as effects from secondary and photoelectron emissions and is considered to be a reasonable proxy for grain surface potential for grains of all sizes above about 50 nm [*Shafiq et al.*, 2011]. Moreover, the LP observations [*Wahlund et al.*, 2005] during Saturn orbit insertion (SOI) inbound pass is consistent with the electrostatic equilibrium potential of the dust grains in Saturn's inner magentosphere measured by the CDA [*Kempf et al.*, 2006]. The mass of water group ions and neutral gases are 18 $m_p$. The mass of dust is

$$m_d = \frac{4\pi \rho r_d^3}{3} \; [\text{kg}] \tag{3.20}$$

since the bulk density of dust made from water ice is given by $\rho = 10^3$ kg m$^{-3}$, and the ionospheric conductivity $\Sigma_i$ is 1 S [*Cowley and Bunce*, 2003]. *Cowley and Bunce* [2003] indicated that the conductivity was of the order of ~1 S or less in the middle latitude ionosphere.

### 3.2.3    Boundary condition

The steady-state solutions of proton, water groups ion and dust speeds are calculated. A grid size is 0.1 R$_S$ from 2 to 10 R$_S$ in radial direction. Initial speeds of each ion are the co-rotation speed and initial speed of dust is the Keplerian speed. Speeds at 2 R$_S$ of each ion are fixed to the co-rotation speed and gradients of each ion speed at outer boundary are zero. On the other hand, dust speed at 2 R$_S$ is the Keplerian speed and gradient of dust speed at outer boundary is zero. It is assumed that the electron has the co-rotation speeds from 2 to 10 R$_S$.

## 3.3    Results

The observations from LP revealed that ion speeds are much smaller than the co-rotation speed and a large amount of cold ions interact with negatively charged dust particles

[*Holmberg et al.*, 2012].
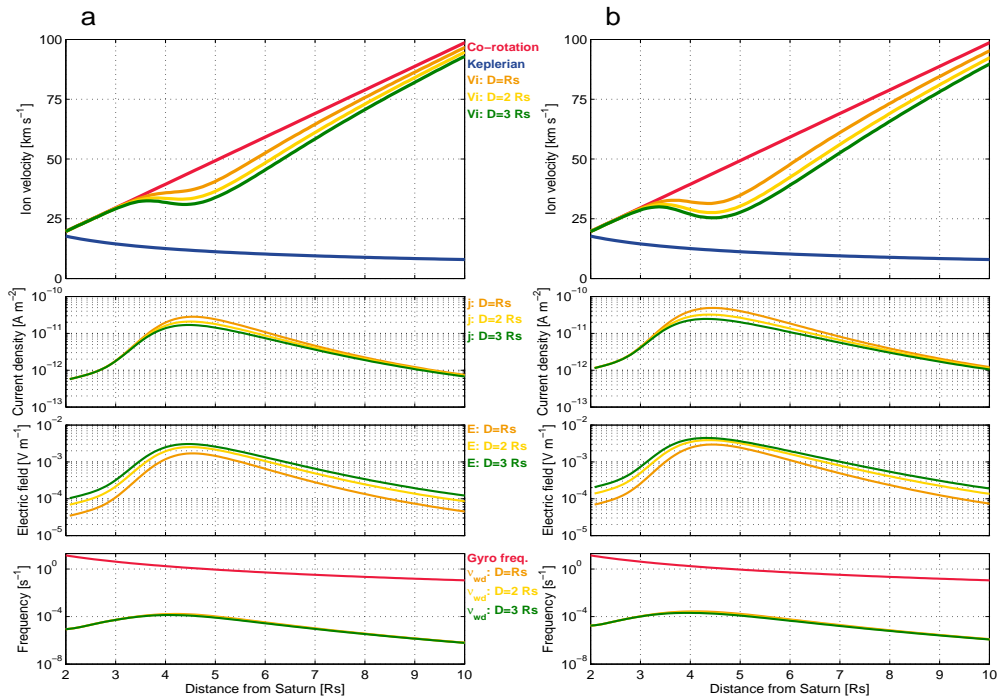


Figure 3.3: Modeling results. (a) $n_{d,r=2R_S} = 3.2 \times 10^4$ m$^{-3}$, (b) $n_{d,r=2R_S} = 6.4 \times 10^4$ m$^{-3}$. (top) Ion velocity profile. Red line indicates the ideal co-rotation speed, and blue line indicates the Keplerian speed. Orange, yellow and green lines indicate ion velocities calculated when the thickness of dust distribution, $D$, is 1 R$_S$, 2 R$_S$ and 3 R$_S$, respectively. (second) Total current density profile. Orange, yellow and green lines indicate current density calculated when the thickness of dust distribution is 1 R$_S$, 2 R$_S$ and 3 R$_S$, respectively. (third) Electric field generated by the difference of motion among ions, electrons and dusts. Orange, yellow and green lines indicate a magnetospheric electric field calculated when the thickness of dust distribution is 1 R$_S$, 2 R$_S$ and 3 R$_S$, respectively. (bottom) Ion-dust collision frequency profile. Red line indicates ion cyclotron frequency for water group. Orange, yellow and green lines indicate ion-dust collision frequencies calculated when the thickness of dust distribution is 1 R$_S$, 2 R$_S$ and 3 R$_S$, respectively [reproduced from *Sakai et al.*, 2013].

To explain these results, the effect of coulomb collisions between the ions and dust particles, the mass loading, the charge exchange and the magnetospheric electric field are investigated. The parameters are the density and thickness of the dust distribution. Fig.3.3a shows the relationship of distance from Saturn with ion speed, current density, generated magnetospheric electric field and frequency. The red line indicates the ideal co-

rotation speed, and the blue line indicates the Keplerian speed; furthermore, the orange, yellow and green lines indicate the ion speed when the thickness of dust distribution, $D$, is 1 $R_S$, 2 $R_S$ and 3 $R_S$, respectively. The second panels show the current density; the colors denote the same meaning as in the top panels. The third panels show the electric field generated by the difference of motions among ions, electrons and dusts; the colors denote the same meaning as in the top panels. The bottom panels show the frequency profile. The red line in the bottom panels indicates the ion cyclotron frequency and the other line indicates the ion-dust collision frequency, $\nu_{wd}$. Fig.3.3a is the case of $n_{d,r=2R_S} = 3.2 \times 10^4$ m$^{-3}$ (Case 1, 3 and 5 in Table 3.2) and Fig.3.3b is the case of $n_{d,r=2R_S} = 6.4 \times 10^4$ m$^{-3}$ (Case 2, 4 and 6 in Table 3.2).

Table 3.2: Modeling parameters.

|        | Dust density at 2 $R_S$ [m$^{-3}$] | Thickness of dust distribution |
|--------|-------------------------------------|--------------------------------|
| Case 1 | $3.2 \times 10^4$, panel (a) in Fig.3.2 | 1 $R_S$ |
| Case 2 | $6.4 \times 10^4$, panel (b) in Fig.3.2 | |
| Case 3 | $3.2 \times 10^4$, panel (a) in Fig.3.2 | 2 $R_S$ |
| Case 4 | $6.4 \times 10^4$, panel (b) in Fig.3.2 | |
| Case 5 | $3.2 \times 10^4$, panel (a) in Fig.3.2 | 3 $R_S$ |
| Case 6 | $6.4 \times 10^4$, panel (b) in Fig.3.2 | |

Ion speeds are the ideal co-rotation speed within about 3 $R_S$ in all cases (Fig.3.3). However, the ion speeds start to decrease from the ideal co-rotation speed around 3 $R_S$. The ion speeds are 50-90% of the ideal co-rotation speed less than about 5 $R_S$ (top panel in Fig.3.3). On the other hand, the ion speeds are close to the ideal co-rotation speed larger than about 5 $R_S$ since the dust density is less than that in the inner region (Fig.3.3). The generated electric field is $10^{-4}$ to $10^{-2}$ V m$^{-1}$ within about 6 $R_S$. However, it is about $10^{-5}$-$10^{-4}$ V m$^{-1}$ outside of 5 $R_S$ (third panel in Fig.3.3). The magnetospheric electric field is smaller than the co-rotational electric field when current flows in the magneto-sphere. Therefore, the ion speeds decrease from the ideal co-rotation speed. However, the local current density is not relevant to the thickness of dust distribution, $D$ (middle panel in Fig.3.3). The magnetospheric electric field is determined by the magnetosphere-ionosphere coupling. A current flowing the ionosphere is equivalent to the magnetospheric

current from the conservation law of current. The thickness of dust distribution is important parameter for a total current flowing the magnetosphere since the total current depends on $D$. The generated magnetospheric electric field is smaller when $D$ is large. The green lines in Fig.3.3 are about 80% of the orange lines around 5 $R_S$ (top panel in Fig.3.3). For the generated magetospheric electric field, the green line is larger than the orange line (third panel in Fig.3.3). Therefore, the ion speeds also depend on $D$ and they are smaller when $D$ is large. The generated magnetospheric electric field also depends on each density since the magnetospheric total current is determined by each density, especially ion density. The ion density increases when dust density increases (see equation (3.17)). It means that the variation of the dust density is important for the electric field. The ion speeds in Fig.3.3b (corresponding to Case 2, 4 and 6) are less than those in Fig.3.3a (Case 1, 3 and 5). Therefore, the ion speeds are smaller when the dust density is larger. On the other hand, the collisions between ions and dust particles do not have a direct effect on ion speed because $\nu_{wd}$ is much smaller than the ion cyclotron frequency (red line of bottom panel in Fig.3.3).

From these results, the ions interact with the dusts through magnetosphere-ionosphere coupling when the thickness of the dust distribution and the dust density is large. The ions are slowing from the ideal co-rotation speed.

## 3.4   Discussion

The ion speeds were calculated by using a multi-species fluid model. Our calculations show that the ion speed becomes smaller than the ideal co-rotation speed as a result of coulomb collisions with dust and mass loading, and the magnetosphere-ionosphere coupling is considerably important through the ion-dust collision in Saturn's inner magnetosphere. Ion observations by the LP onboard the Cassini indicated that ion speed increases as the distance from Saturn increases [*Holmberg et al.*, 2012]. The ion speeds in the plasma disk are 50-70% of co-rotation speed within 7 $R_S$.
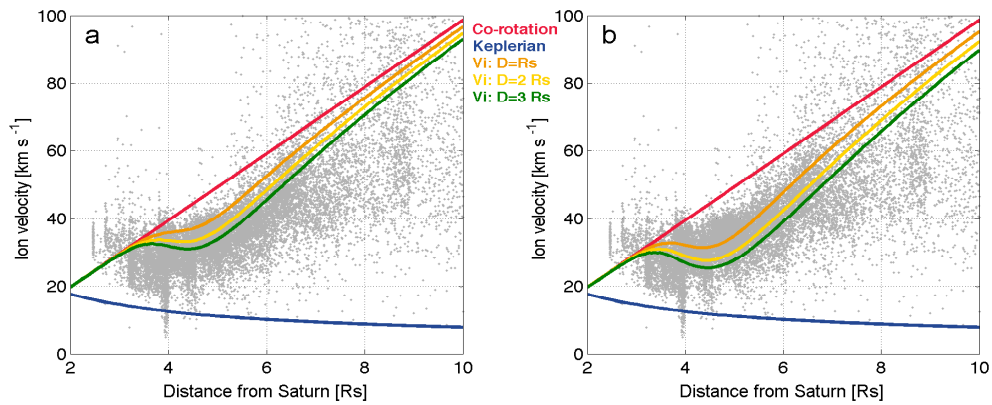
Figure 3.4: Comparisons between modeling results and RPWS/LP observations. (a) $n_{d,r=2R_S} = 3.2 \times 10^4$ m$^{-3}$, (b) $n_{d,r=2R_S} = 6.4 \times 10^4$ m$^{-3}$. Ion velocities are superposed on the LP observations from *Holmberg et al.* [2012]. Grey dots are observation points, red line indicates the ideal co-rotation speed, and blue line indicates the Keplerian speed. Orange, yellow and green lines indicate ion velocities calculated when the thickness of dust distribution, $D$, is 1 R$_S$, 2 R$_S$ and 3 R$_S$, respectively [reproduced from *Sakai et al.*, 2013].

Our modeling results are consistent with LP observations when the dust density is large (Fig.3.4b). Our results are also consistent with observations even if the dust density is small if the thickness of dust distribution, $D$, is large (green line in Fig.3.4a). The ion speeds strongly depend on the magnetospheric electric field. The magnetospheric electric field is governed by the inner magnetospheric total Pedersen current, and the Pedersen current is generated by the collisions and the mass loading. The Pedersen current flows along the magnetic field line and weaken the dynamo electric field in Saturn's ionosphere. Accordingly, the magnetospheric electric field is smaller than the co-rotational electric field and the ion speeds are less than the ideal co-rotation speed. The magnitude of the Pedersen current is dependent on each density and $D$. Higher Pedersen current flows in the inner magnetosphere when each density or $D$ is large. Since more density is needed when $D$ is small, it is suggested that the maximum of dust density is larger than $\sim 10^5$ m$^{-3}$ in Saturn's inner magnetosphere (Fig.3.4).

*Morooka et al.* [2011] reported that the ion speeds are nearly the Keplerian speed and that the densities of ions and dust are large in the vicinity of Enceladus. The ion and dust densities are much larger in this region due to the Enceladus plume. Under this condition, the total current due to ion-dust collision is much larger than that in other regions since the current is proportional to the densities. It is noted that the ion speed approaches the Keplerian speed when the dust density is larger than about $10^6$ m$^{-3}$.

*Wahlund et al.* [2009] suggested the existence of two ion populations: one co-rotating with the planetary magnetosphere and another moving at near Keplerian speed around Saturn. Hot ions (ca. 10-50 eV) are co-rotating without being trapped by dust, and cold ions (a few electron volts) are slowed from the co-rotation speed by the dust drag. The LP observations of particles of a few electron volts obtained much lower ion speeds, including values less than 50% of the ideal co-rotation speed. On the other hand, from CAPS observations of particles of a few hundred electron volts, ion speeds are 50-80% of the ideal co-rotation [*Wilson et al.*, 2008, 2009; *Thomsen et al.*, 2010]. Taken together, the results from CAPS and LP observations show that two ion populations exist in Saturn's inner magnetosphere, as suggested by *Wahlund et al.* [2009].

In other models, co-rotational lag has an effect outside the inner magnetosphere [*Hill*, 1979; *Saur et al.*, 2004]. *Saur et al.* [2004] accounted for radial mass transport and magnetospheric conductance in their model. Their results were ion speeds less than the ideal co-rotation beyond 5 $R_S$. Our results show that the ion speeds are the ideal co-rotation speed within 3 $R_S$, which is consistent with the results of *Saur et al.* [2004] within 3 $R_S$.

*Kurth et al.* [2006] reported a vertical distribution of dust near Enceladus' orbit using the RPWS. The thickness of dust distribution is about 15,000 km ($\sim$0.25 $R_S$). On the other hand, a ratio of an electron density to an ion density ($n_e/n_i$) in *Morooka et al.* [2011] is less than one between the -80 and 50 $R_E$ (1 $R_E$ = 251.8 km is the radius of Enceladus), which is corresponding to about 0.6 $R_S$. However, the thickness of dust distributions was estimated between 1 and 3 $R_S$ since the density profile of the vertical direction higher than 50 $R_E$ and lower than 80 $R_E$ is not reported and $n_e/n_i$ is not one at -80 and 50 $R_E$. If the thickness of dust distribution is 1 $R_S$, the maximum of dust density needs at least $10^5$ m$^{-3}$. Moreover, a more accurate treatment of the dust and the ionosphere could affect our results. The reality is a dust distribution with a size, mass and charge. The ionospheric conductivity could also affect the generated magnetospheric electric field. Therefore, it is necessary to consider the dust distribution and the ionospheric conductivity in the next study.

Many observations have found strong planetary rotational modulation of Saturn's magnetospheric plasma despite the nearly parallel alignment of the magnetic dipole and the planetary axis [*Gurnett et al.*, 2007; *Kurth et al.*, 2008]. This modulation causes the magnetodisc plasma to wobble with respect to the E ring [*Goertz et al.*, 1981]. The interaction between dust and ions in the E ring will be enhanced once each planetary spin axis, showing the longitude dependence of ion and dust parameters [Figure 8 in *Morooka et al.*, 2011]. *Kurth et al.* [2008] showed a clear relationship between the Cassini spacecraft potential of the plasma disk and longitude of the Saturn Longitude System. *Gurnett et al.* [2007] also reported that the plasma and magnetic fields in the Saturn's plasma disk rotate in synchronism with the time-variable modulation period of Saturn's kilometric

radio emission. The longitudinal dependence of parameters, e.g., ion speed and density, may be important in explaining the planetary rotational modulations.

## 3.5   Summary

The ion drift speed was calcualted by using a multi-species fluid model (i.e., protons, water group ions, electrons, and charged dust) in order to examine the effect of dust on ion speed. In agreement with the LP observations, the modeling results showed that the ion speeds are less than the co-rotation speed. The ion speeds are possibly less than the co-rotation speed as a result of the magnetospheric electric field generated through ion-dust collisions.

Dust-plasma interaction occurs through magnetosphere-ionosphere coupling. The inner magnetospheric total current along a magnetic field line weakens the dynamo electric field in Saturn's ionosphere. The ion speeds are Keplerian due to the large total current when the ion and dust densities are large. The dust-plasma interaction is significant when the thickness of the dust distribution is large and/or the density of ions and dusts is high.

The constant ionospheric conductivity, 1 S, was given in this chapter. However, the variation of the conductivity would be important for the electric field. The ionospheric Pedersen conductivity will be calculated in next chapter.

# Chapter 4

# Modeling of the ionosphere

## 4.1   Introduction

The plasma density in the ionosphere is evaluated to estimate the ionospheric Pedersen conductivity in this chapter.

The electron density in the Saturn's ionosphere was measured by the radio occultation of Pioneer 11, Voyager 1 and 2, and Cassini spacecraft. These observations showed that the peak density of the electron was about $10^{10}$ m$^{-3}$ at the altitude of about 1500 km [*Kliore et al.*, 1980; *Tyler et al.*, 1981, 1982; *Lindal et al.*, 1985; *Nagy et al.*, 2006; *Kliore et al.*, 2009] and the electron density decreased to about $10^8$ m$^{-3}$ at the altitude of 10000 km [*Nagy et al.*, 2006; *Kliore et al.*, 2009]. In some models the electron density of topside was consistent with the density from radio occultation [e.g., *Moses and Bass*, 2000; *Moore et al.*, 2006, 2008], and the plasma temperature of topside was about 500 K [*Moore et al.*, 2008]. The models of *Moore et al.* [2006, 2008] included the constant flux of neutral water which was emitted from Enceladus and diffused in the magnetosphere. The Saturn's moon Enceladus is expelling gases which is mainly composed of water from its south pole [*Porco et al.*, 2006; *Waite et al.*, 2006] and supplying the plasma to the inner magnetosphere [*Smith et al.*, 2010]. *Moore et al.* [2006, 2008] considered that the neutral gases in the inner magnetosphere are affecting the ionosphere. In their ionospheric model, the plasma density and temperature was calculated below only the altitude of 4000 km.

The ionospheric Pedersen conductivity was estimated in previous some studies [*Connerney et al.*, 1983; *Cheng and Waite*, 1988; *Saur et al.*, 2004; *Cowley et al.*, 2004; *Moore et al.*, 2010]. The conductivity estimated by *Connerney et al.* [1983] and *Cheng and Waite* [1988] varied from ∼0.1 S to ∼100 S. These values however did not explain the slippage of Saturn's atmosphere [*Eviatar and Richardson*, 1986; *Cheng and Waite*, 1988; *Huang and Hill*, 1989]. *Saur et al.* [2004] estimated the conductivity from the azimuthal velocity measurements of the Voyager spacecraft. They assumed a low value of 0.014 S and 0.035 S for the conductivity. *Cowley et al.* [2004] also estimated the conductivity from the co-rotational deviation and they gave ∼1 S. *Moore et al.* [2010] estimated it from the plasma density in the ionosphere and found the latitudinal variation of the conductivity.

In this chapter, the plasma densities, velocities and temperatures calculated by a MHD model including the magnetospheric effects are reported and the relationship between the conductivity and the dust-plasma interaction, and the importance of the magnetosphere-ionosphere coupling in Saturn's system are discussed.

## 4.2    Model

### 4.2.1    Continuity, Momentum, and Energy Equations

The plasma densities, velocities and temperatures in the Saturn's ionosphere are calculated by using a MHD model to investigate the influence of the magnetospheric plasma. The quasistatic state solution are evaluated. The orthogonal dipolar coordinates, which was first introduced by *Dragt* [1961], are used and the physical quantities are calculated at $L = 5$ (Lat.=63.4). The ion densities and velocities are simulated by the following equations:

$$\frac{\partial \rho_i}{\partial t} + \frac{1}{A} \frac{\partial \left( A \rho_i v_{i,||} \right)}{\partial s} = S_i - L_i \tag{4.1}$$

$$\rho_i \frac{\partial v_{i,||}}{\partial t} + \rho_i v_{i,||} \frac{\partial v_{i,||}}{\partial s} = n_i e E_{||} - \frac{\partial p_i}{\partial s} - \rho_i g - \sum_k \rho_i \nu_{ik} \left( v_{i,||} - v_{k,||} \right) \tag{4.2}$$

where $v_{i,||}$ is the ion field-aligned velocity; $m_i$ is the ion mass; $e$ is the charge quantity; $E_{||}$ is the electrical field of field-aligned direction; $\nu_{il}$ is the ion collision frequency among the electrons, neutral gases, dusts and other components of ions; $n_i$ is the ion number density; $\rho_i$ is $m_i n_i$; $A$ is the cross-sectional area of magnetic flux tube; $S_i$ is the ion production rate; $L_i$ is the ion loss rate. The calculated ion components are $H^+$, $H_2^+$, $H_3^+$, $He^+$, $H_2O^+$ and $H_3O^+$. The chemical reactions are listed in Table 4.1 and Table 4.2. The ion temperature is given by

$$T_i = T_e \tag{4.3}$$

where $T_i$ is the ion temperature and $T_e$ is the electron temperature. The electron temperature is written as,

$$\frac{\partial T_e}{\partial t} - \frac{2}{3}\frac{1}{A}\frac{\partial}{\partial s}\left(A\kappa_e \frac{\partial T_e}{\partial s}\right) = Q_e \tag{4.4}$$

where $\kappa_e$ is the thermal conductivity and $Q_e$ is the electron heating rate. The electron number density is given by,

$$n_e = \sum_i n_i - \frac{q_d}{e}n_d \tag{4.5}$$

where $q_d$ is the charged quantity of dusts and $n_d$ is the dust density. It is assumed that the negative charged dusts are existence in the inner magnetosphere [e.g., *Horányi et al.*, 2004]. The field-aligned electric field is derived from the approximation of the electron momentum equation and it is expressed by,

$$E_{||} = -\frac{1}{en_e}\frac{\partial p_e}{\partial s}. \tag{4.6}$$

## 4.2.2 Magnetospheric Effects and Boundary Conditions

The magnetospheric plasma density and temperature are given to investigate how the magnetospheric plasma affects the ionosphere. The electron density is $3.7 \times 10^7$ m$^{-3}$ [*Persoon et al.*, 2009; *Sakai et al.*, 2013] and the dust density is $1.1 \times 10^5$ m$^{-3}$ in the magnetosphere [*Sakai et al.*, 2013]. The two magnetospheric plasma components are assumed in the inner magnetosphere and they are the proton and the water group ion.

The magnetospheric ion density is derived from the electron and dust density, and the water group ion density is $4.2 \times 10^7$ m$^{-3}$ and the proton density is $1.0 \times 10^7$ m$^{-3}$ at $L = 5$. The magnetospheric electron temperature is 2 eV [*Wahlund et al.*, 2009; *Gustafsson and Wahlund*, 2010; *Sakai et al.*, 2013]. The ion-dust collision is also included in our model [*Sakai et al.*, 2013].

The atmospheric pressure 1 mbar is used as the altitude of 0 km. At the lower boundary of 2 km altitude the ion densities are in chemical equilibrium,

$$S_i = L_i \tag{4.7}$$

and the electron temperatures are the same as the neutral temperature.

## 4.3 Atmospheric Model

### 4.3.1 Background Atmosphere and Ion Chemistry

Fig.4.1 shows the density (panel a) and temperature (panel b) profiles of the background atmosphere. The neutral mixing ratio of H and He is from *Moses and Bass* [2000] and *Moses et al.* [2000], and H$_2$O from *Moore et al.* [2009]. The neutral temperature model suggested by *Gérard et al.* [2009] is given and the equinox is assumed in this model.

Chemical reactions for six ion components (H$^+$, H$_2^+$, H$_3^+$, He$^+$, H$_2$O$^+$ and H$_3$O$^+$) are solved. The chemical reactions are listed in Table 4.1 and Table 4.2. The loss of H$^+$ by reactions with vibrationally excited H$_2$ ($\nu \geq 4$) is taken in our model [*Moses and Bass*, 2000].
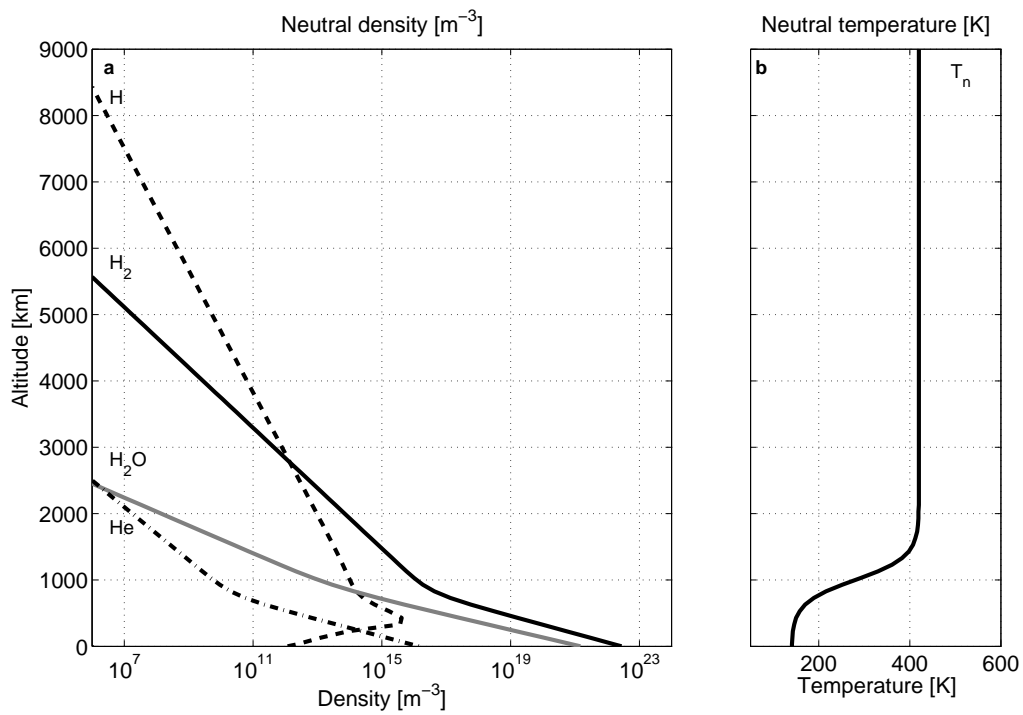
Figure 4.1: Background atmospheric (a) density and (b) temperature. Black dashed line shows H, black solid line shows $H_2$, black dashed-dotted line shows He and grey solid line shows $H_2O$.

Table 4.1: Photoionization and ion recombination reactions.

| Chemical reaction | Rate coefficients | References |
|---|---|---|
| $\mathrm{H} + h\nu \to \mathrm{H}^+ + e^-$ | | *Moses and Bass* [2000] |
| $\mathrm{H}_2 + h\nu \to \mathrm{H}^+ + \mathrm{H} + e^-$ | | *Moses and Bass* [2000] |
| $\mathrm{H}_2 + h\nu \to \mathrm{H}_2^+ + e^-$ | | *Moses and Bass* [2000] |
| $\mathrm{He} + h\nu \to \mathrm{He}^+ + e^-$ | | *Moses and Bass* [2000] |
| $\mathrm{H}_2\mathrm{O} + h\nu \to \mathrm{H}^+ + \mathrm{OH} + e^-$ | | *Moses and Bass* [2000] |
| $\mathrm{H}_2\mathrm{O} + h\nu \to \mathrm{H}_2\mathrm{O}^+ + e^-$ | | *Moses and Bass* [2000] |
| $\mathrm{H}^+ + e^- \to \mathrm{H}$ | $1.9 \times 10^{-16} T_e^{-0.7}$ | *Moses and Bass* [2000]; *Kim and Fox* [1994] |
| $\mathrm{H}_2^+ + e^- \to 2\mathrm{H}$ | $2.3 \times 10^{-12} T_e^{-0.4}$ | *Moses and Bass* [2000]; *Kim and Fox* [1994] |
| $\mathrm{H}_3^+ + e^- \to \mathrm{H}_2 + \mathrm{H}$ | $7.6 \times 10^{-13} T_e^{-0.5}$ | *Moses and Bass* [2000]; *Kim and Fox* [1994] |
| $\mathrm{H}_3^+ + e^- \to 3\mathrm{H}$ | $9.7 \times 10^{-13} T_e^{-0.5}$ | *Moses and Bass* [2000]; *Kim and Fox* [1994] |
| $\mathrm{He}^+ + e^- \to \mathrm{He}$ | $1.9 \times 10^{-16} T_e^{-0.7}$ | *Moses and Bass* [2000]; *Kim and Fox* [1994] |
| $\mathrm{H}_2\mathrm{O}^+ + e^- \to \mathrm{O} + \mathrm{H}_2$ | $3.5 \times 10^{-12} T_e^{-0.5}$ | *Moses and Bass* [2000]; *Millar et al.* [1997] |
| $\mathrm{H}_2\mathrm{O}^+ + e^- \to \mathrm{OH} + \mathrm{H}$ | $2.8 \times 10^{-12} T_e^{-0.5}$ | *Moses and Bass* [2000]; *Millar et al.* [1997] |
| $\mathrm{H}_3\mathrm{O}^+ + e^- \to \mathrm{H}_2\mathrm{O} + \mathrm{H}$ | $6.1 \times 10^{-12} T_e^{-0.5}$ | *Moses and Bass* [2000]; *Millar et al.* [1997] |
| $\mathrm{H}_3\mathrm{O}^+ + e^- \to \mathrm{OH} + 2\mathrm{H}$ | $1.1 \times 10^{-11} T_e^{-0.5}$ | *Moses and Bass* [2000]; *Millar et al.* [1997] |

Table 4.2: Charge exchange reactions.

| Chemical reaction | Rate coefficients | References |
|---|---|---|
| $H^+ + H_2 \rightarrow H_2^+ + H$ | see text | *Moses and Bass* [2000] |
| $H^+ + H_2 + M \rightarrow H_3^+ + M$ | $3.2 \times 10^{-41}$ | *Moses and Bass* [2000]; *Kim and Fox* [1994] |
| $H^+ + H_2O \rightarrow H_2O^+ + H$ | $8.2 \times 10^{-15}$ | *Moses and Bass* [2000]; *Anicich* [1993] |
| $H_2^+ + H \rightarrow H^+ + H_2$ | $6.4 \times 10^{-16}$ | *Moses and Bass* [2000]; *Anicich* [1993] |
| $H_2^+ + H_2 \rightarrow H_3^+ + H$ | $2.0 \times 10^{-15}$ | *Moses and Bass* [2000]; *Kim and Fox* [1994] |
| $H_2^+ + H_2O \rightarrow H_2O^+ + H_2$ | $3.9 \times 10^{-15}$ | *Moses and Bass* [2000]; *Anicich* [1993] |
| $H_2^+ + H_2O \rightarrow H_3O^+ + H$ | $3.4 \times 10^{-15}$ | *Moses and Bass* [2000]; *Anicich* [1993] |
| $H_3^+ + H_2O \rightarrow H_3O^+ + H_2$ | $5.3 \times 10^{-15}$ | *Moses and Bass* [2000]; *Anicich* [1993] |
| $He^+ + H_2 \rightarrow H^+ + H + He$ | $8.8 \times 10^{-20}$ | *Matcheva et al.* [2001]; *Perry et al.* [1999] |
| $He^+ + H_2 \rightarrow H_2^+ + He$ | $9.4 \times 10^{-21}$ | *Moses and Bass* [2000]; *Kim and Fox* [1994] |
| $He^+ + H_2O \rightarrow H^+ + OH + He$ | $1.9 \times 10^{-16}$ | *Moses and Bass* [2000]; *Anicich* [1993] |
| $He^+ + H_2O \rightarrow H_2O^+ + He$ | $5.5 \times 10^{-17}$ | *Moses and Bass* [2000]; *Anicich* [1993] |
| $H_2O^+ + H_2 \rightarrow H_3O^+ + H$ | $7.6 \times 10^{-16}$ | *Moses and Bass* [2000]; *Anicich* [1993] |
| $H_2O^+ + H_2O \rightarrow H_3O^+ + OH$ | $1.9 \times 10^{-15}$ | *Moses and Bass* [2000]; *Anicich* [1993] |

## 4.3.2   Electron Heating Rates

The electron heating rate $Q_e$ is given by the sum of the local heating and the non local heating:

$$Q_e = Q_{EUV} + Q_{coll} + Q_{joule} + Q_{ph,ionos} + Q_{ph,mag} \tag{4.8}$$

where $Q_{EUV}$ is the heating rate due to the photoelectron produced by the solar EUV radiation; $Q_{coll}$ is the heating rate due to the collision between electrons and neutral gases; $Q_{joule}$ is the joule heating; $Q_{ph,ionos}$ is the heating rate due to the ionospheric photoelectron at the altitude above about 1200 km; $Q_{ph,mag}$ is the heating rate due to the magnetospheric photoelectron. $Q_{EUV}$, $Q_{coll}$ and $Q_{joule}$ are the local heating and $Q_{ph,ionos}$ and $Q_{ph,mag}$ is the nonlocal heating. $Q_{EUV}$ is given by,

$$Q_{EUV} = \frac{2e}{3n_e k_B} \sum_n f_{ion} n_n E_{photo} \exp(-\tau) \tag{4.9}$$

where $f_{ion}$ is the ionization frequency; $E_{photo}$ is the energy of the photoelectron; $\tau$ is the optical depth; $n_n$ is the neutral density; $k_B$ is the Boltzmann constant. $Q_{coll}$ is given by [e.g., *Huba et al.*, 2000],

$$Q_{coll} = \sum_n \frac{2m_e m_n}{(m_e + m_n)^2} \nu_{en} (T_n - T_e) \tag{4.10}$$

where $m_e$ is the electron mass; $m_n$ is the mass of the neutral gas; $\nu_{en}$ is the collision frequency between the electron and the neutral gas; $T_n$ is the temperature of neutral gas. $Q_{joule}$ is given by,

$$Q_{joule} = \frac{2}{3k_B n_e} \sigma_p E_\perp^2 \tag{4.11}$$

where $\sigma_p$ is the local Pedersen conductivity and $E_\perp$ is the perpendicular electric field. $Q_{ph,ionos}$ is given by,

$$Q_{ph,ionos} = \frac{2}{3} \frac{B}{B_t} q_t \exp(-C \int n_e ds) \tag{4.12}$$

where $B$ is the strength of the local magnetic field; $B_t$ is the strength of the magnetic field at about 1200 km; $q_t$ is the heating rate per electron at about 1200 km; $ds$ is the

differential length along the magnetic field line; $C$ is the constant value and it is $3 \times 10^{-18}$ m$^2$ [e.g., *Nisbet*, 1968; *Millward et al.*, 1996; *Huba et al.*, 2000]. $Q_{ph,mag}$ is given by,

$$Q_{ph,mag} = \frac{2e}{3n_e k_B} \frac{E_{photo} q_{ph} \varepsilon}{l_e} \tag{4.13}$$

where $q_{ph}$ is the flux of the photoelectron; $\varepsilon$ is the heat efficiency; $l_e$ is the electron mean free path.

## 4.4 Results

The plasma densities, velocities and temperatures were calculated by using a MHD model including the magnetospheric effect. Fig.4.2 shows the plasma densities (panel a), the ion velocities (panel b), the plasma temperature (panel c), and the heating rate (panel d) at 12 LT below 10000 km. At the altitude of 10000 km the electron density was about $10^7$ m$^{-3}$ and increased to about $10^{10}$ m$^{-3}$ at the altitude of 1200 km (panel a). H$_X$O$^+$ was the dominant ion at the altitude below 1000 km, and its peak density was about $10^8$ m$^{-3}$. The dominant ion changed to H$_3^+$ as the altitude was high and the maximum density was about $5.4 \times 10^9$ m$^{-3}$ at the altitude of 1200 km. The H$^+$ velocity was accelerated in equatorial direction above 2000 km and it was about 15 km/s at the altitude of 10000 km. On the other hand, the H$_X$O$^+$ has downward velocity below 10000 km. This might depend on the difference of mass. The light components are blown to equatorial region by the centrifugal force, while the heavy components fall down due to the gravity of the planet. The electron temperature was 140 K at the lower boundary and it increased to 20000 K at the altitude of 10000 km (panel c). This is since the heating due to the heat flow significantly affects the electron temperature. The heat flow was dominant at the altitude above 2000 km. The heating due to collisions and the joule heating were important below 2000 km (panel d). A temperature peak below 1000 km was due to the joule and collision heating.

Fig.4.3-Fig.4.5 show the plasma parameters in each local time. Each panel is same as Fig.4.2. Fig.4.6 shows the diurnal variations of the electron density, temperature and the Pedersen conductivity. The electron density changed between about $10^8$ and $10^{10}$ m$^{-3}$
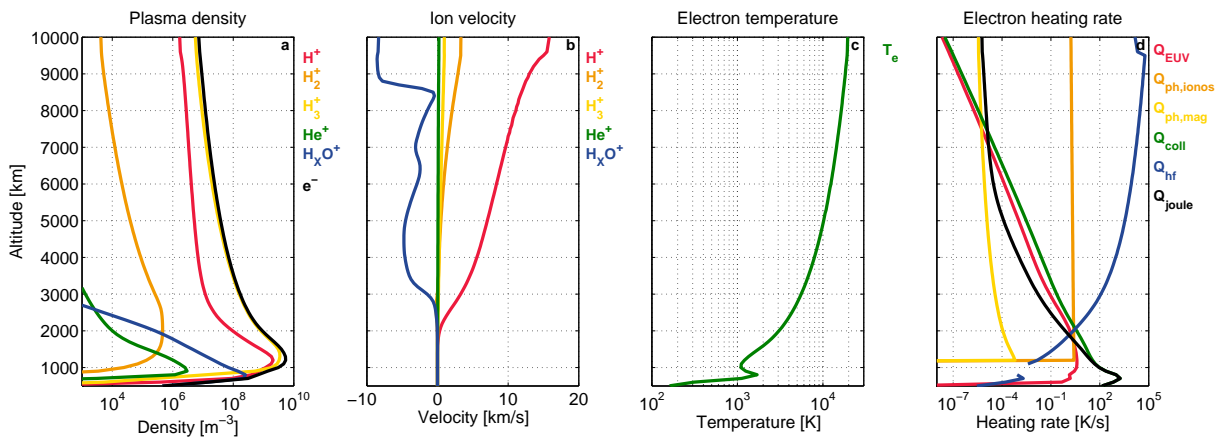
Figure 4.2: Plasma parameters in the mid-latitude at 12 LT. The plasma density profiles are shown in panel a. Red line is $H^+$, orange line is $H_2^+$, yellow line is $H_3^+$, green line is $He^+$, blue line is $H_XO^+$, and black line shows electron. The velocity profiles are shown in panel b, and colors are same as panel a. The electron temperature is shown in panel c (green line). The heating rates are shown in panel d. Red line shows the heating rate due to the solar EUV, orange line shows the heating rate due to the photoelectron from ionosphere, yellow line shows the heating rate due to the photoelectron due to magnetosphere, green line shows the heating rate due to the collision, blue line shows the rate due to the heat flow, and black line shows the joule heating.

below 2000 km and it became maximum around 14 LT (Fig.4.6 panel a). On the other hand, the electron density became maximum around 18 LT above 2000 km, and it became minimum around 6 LT at every altitude. The electron density decreased with increasing the altitude. The Pedersen conductivity showed same tendency as the electron density (Fig.4.6 panel c). It is the largest between 12 and 16 LT, and it decreases with increasing altitudes. The electron temperature didn't depend on the local time, however, it increased slightly around 12 LT because of the heating due to the photoelectron from ionosphere (Fig.4.6 panel b). The electron temperature increased with increasing the altitude, and it was about 2000 K at 2000 km and about 15000 K at 9000 km.
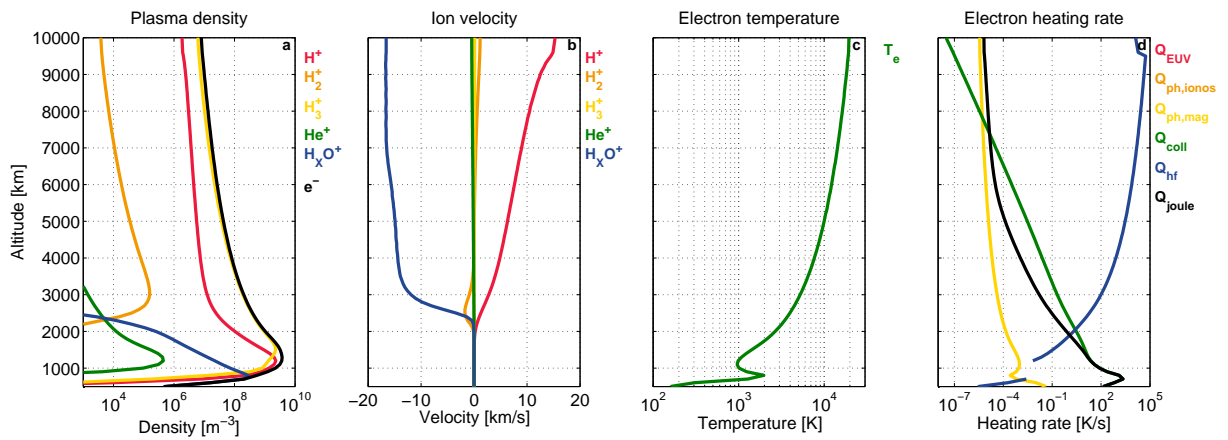


Figure 4.3: Plasma parameters in the mid-latitude at 18 LT. Each panel is same as Fig.4.2.
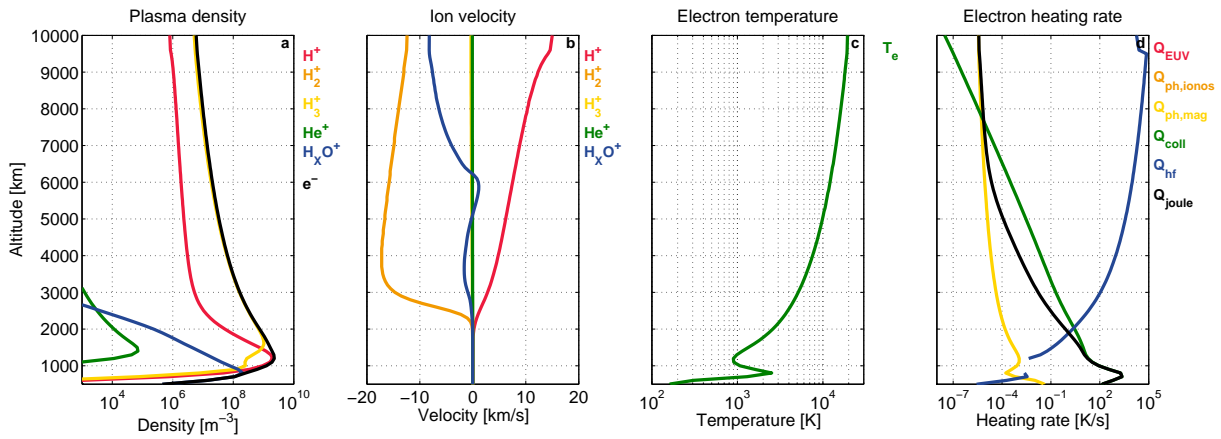
Figure 4.4: Plasma parameters in the mid-latitude at 0 LT. Each panel is same as Fig.4.2.
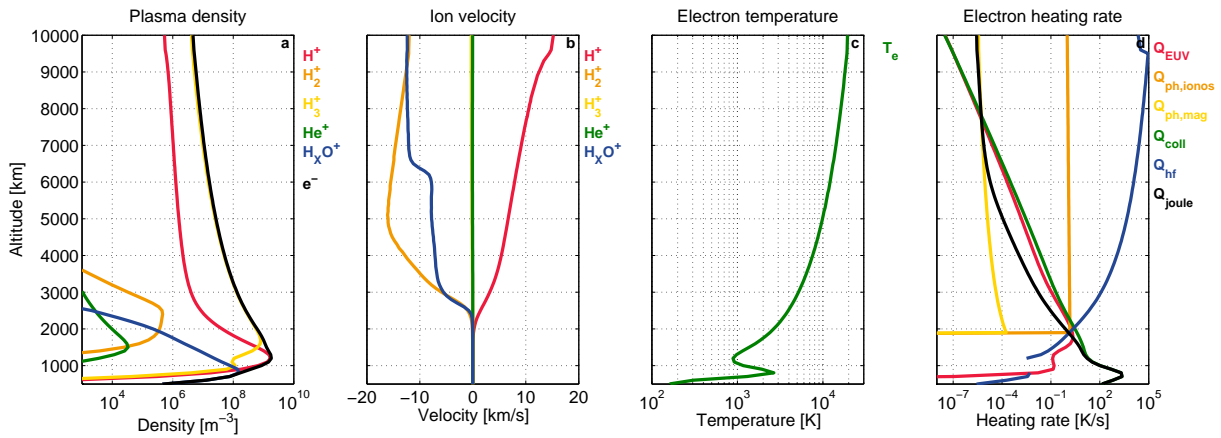
Figure 4.5: Plasma parameters in the mid-latitude at 6 LT. Each panel is same as Fig.4.2.
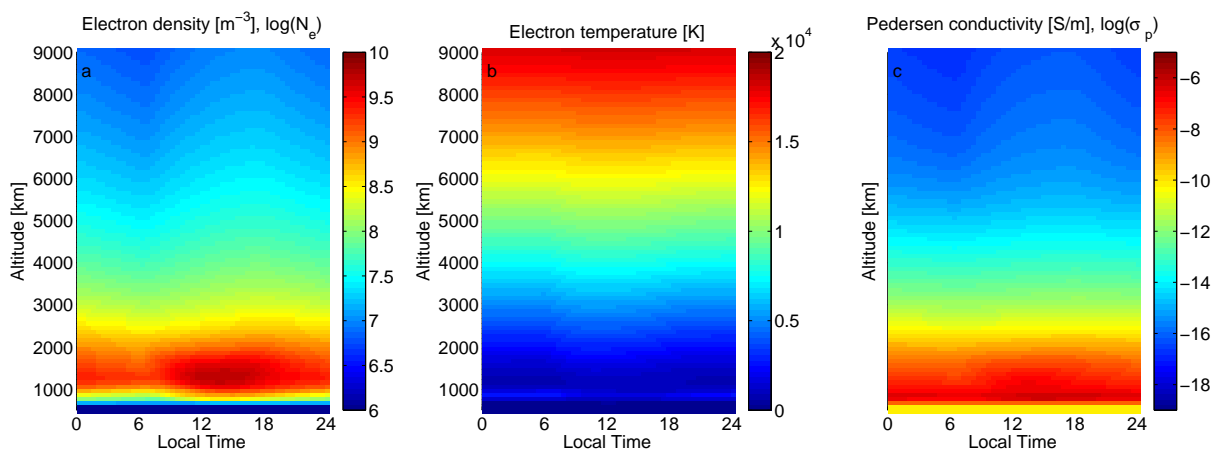
Figure 4.6: Diurnal variation of the electron density, temperature and Pedersen conductivity. (a) Electron density, (b) electron temperature and (c) Pedersen conductivity.

# 4.5   Discussion

The plasma density and temperature in the Saturn's ionosphere are calculated by using a MHD model including the effect of the inner magnetosphere. Our results showed that the plasma density has peak around the altitude of 1200 km, and it was about $10^{10}$ m$^{-3}$ and it decreased to about $10^7$ m$^{-3}$ at 10000 km. The temperature was about 2000 K at 2000 km and increased to about 20000 K at 10000 km, and it didn't almost depend on the local time.

The electron temperature from our modeling was much higher than the temperature of previous studies. At the altitude of 1000 km, it was about 300 K [*Moore et al.*, 2008], however, our temperature was about 1000 K and tripling of past models. This is due to the joule heating. The joule heating occurs when the electric field changes from the co-rotational field. The slippage from the co-rotational field estimated by ion speed observation and previous modeling [*Holmberg et al.*, 2012; *Sakai et al.*, 2013] was considered for the electric field term. The temperature above 2000 km was also much higher than the temperature of previous studies, and our result was higher temperature than 5000 K at the altitude around 3000 km. On the other hand, the temperature from previous models was about 500 K around 3000 km [*Moore et al.*, 2008] and it was one order lower as compared to our result. This is since the heat flow from the magnetosphere significantly affects the ionospheric plasma. The heat flow is remarkably contributing to the heating above 2000 km (Fig.4.2 panel d). Fig.4.7 shows that the electron temperature strongly depends on the joule heating and the heat flow. The temperature is low below 1000 km without the joule heating, and it is about 500 K at 1000 km (grey line). The temperature is also low above 1500 km without the heat flow, and it is about 12000 K at 10000 km (black dashed line). The joule heating at low altitudes and the heat flow at high altitudes are significantly contributing to the heating process.
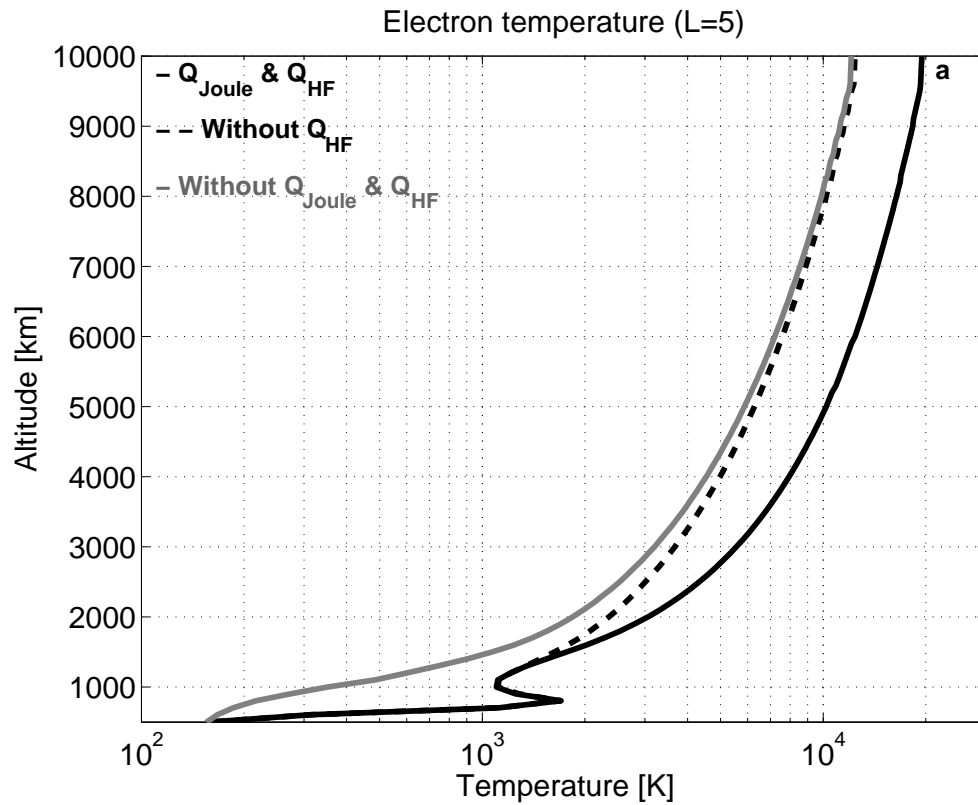
Figure 4.7: The dependence of the heating rate on the electron temperature. Black solid-line shows the temperature adding the Joule heating and heat flow, black dashed line shows the temperature without the heat flow, and grey solid line shows the temperature without the Joule heating and heat flow.

The ionospheric Pedersen conductivity was estimated from the plasma density. The Pedersen conductivity is given by

$$\sigma_p = \sum_i \frac{\nu_i}{\nu_{in}^2 + \omega_{ci}^2} + \frac{\nu_e}{\nu_{en}^2 + \omega_{ce}^2}, \tag{4.14}$$

$$\Sigma_i = \int \sigma_p ds \tag{4.15}$$

where $\nu_{kn}$ is the plasma-neutral collision frequency, $\omega_{ck}$ is the cyclotron frequency of each plasma component, and $\nu_i$ and $\nu_e$ is given by

$$\nu_i = \sum_n \nu_{in} \tag{4.16}$$

$$\nu_e = \sum_n \nu_{en}. \tag{4.17}$$

The conductivity was calculated in past models [*Connerney et al.*, 1983; *Cheng and Waite*, 1988; *Saur et al.*, 2004; *Cowley et al.*, 2004; *Moore et al.*, 2010]. However, those values didn't take in to account the slippage of Saturn's ionosphere [*Eviatar and Richardson*, 1986; *Cheng and Waite*, 1988; *Huang and Hill*, 1989], and they also didn't find the local time dependence. The local time variation of the Pedersen conductivity was evaluated by using equations (4.14) and (4.15). Fig.4.8 shows the local time variation of the Pedersen conductivity. The integrated values were less than 1 S at every time. It is similar to results of *Moore et al.* [2010]. The conductivity was the day, dusk, night and dawn in the order of largest to smallest, and the maximum was 0.77 S and the minimum value was 0.30 S. The Pedersen conductivity significantly depends on the plasma density in the ionosphere.
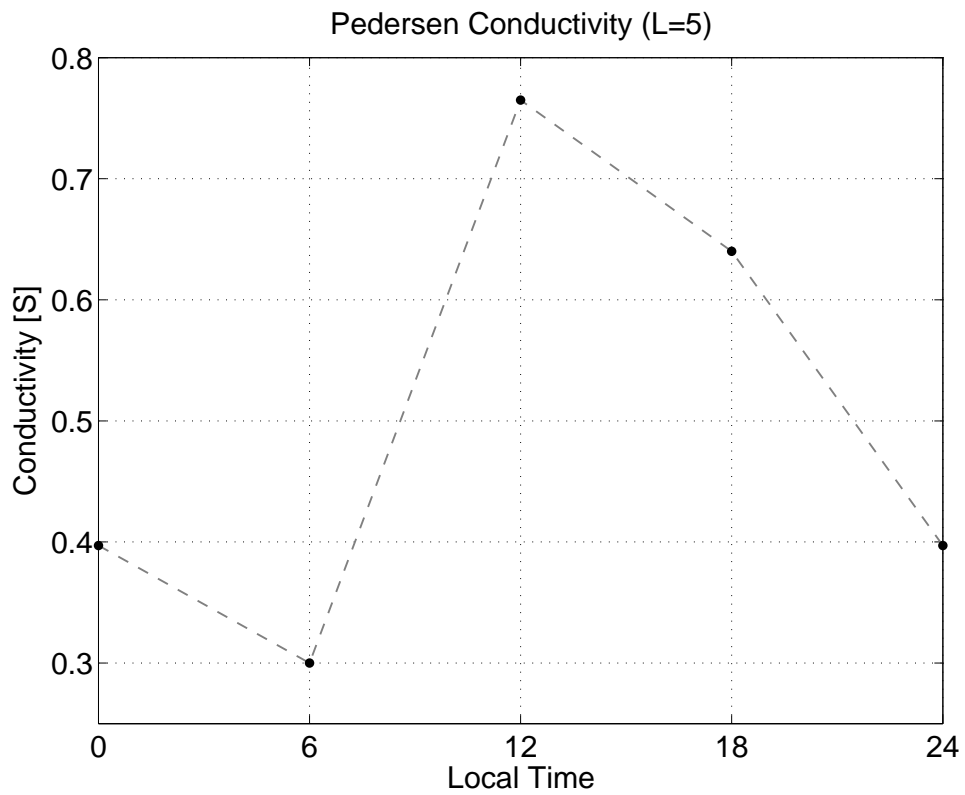
Figure 4.8: Diurnal variation of the Pedersen conductivity (L=5).

# 4.6   Summary

The plasma densities, velocities and temperatures were calculated by using a MHD model in order to investigate the ionospheric Pedersen conductivity. The plasma density was about $10^{10}$ m$^{-3}$ at the altitude of 1200 km, and it decreased to about $10^7$ m$^{-3}$ at the altitude of 10000 km. The dominant ion was H$_3^+$ between 1000 and 10000 km, and it was H$_X$O$^+$ below 1000 km. The H$^+$ has the upward velocity above 2000 km, while heavy ions have zero or downward velocity. This might be due to the difference of mass. The light ions are blown to equatorial region by the centrifugal force, while the heavy ions fall down due to the gravity of the planet at low altitudes. The electron temperature was 140 K at the lower boundary and it increased to 20000 K at the altitude of 10000 km. This is since the heat flow significantly affects the electron temperature. The electron temperature was about 2000 K at the altitude of 1000 km, and the heating due to collisions and the joule heating were important below 2000 km. The electron density changed between about $10^8$ and $10^{10}$ m$^{-3}$ below 2000 km and it became the maximum around 14 LT. Above 2000 km it became the maximum around 18 LT above 2000 km. The minimum is around 6 LT at every altitude. The electron density decreased with increasing the altitude. The electron temperature didn't basically depend on the local time, and it decreased with increasing the altitude. The conductivity was the day, dusk, night and dawn in the order of largest to smallest, and the maximum was 0.77 S and the minimum value was 0.30 S. The Pedersen conductivity significantly depended on the plasma density in the ionosphere.

The magnetospheric ion velocity can be calculated by using this conductivity. The Pedersen conductivities are also calculated in other latitudes, and the corresponding magnetospheric ion velocity will be shown in next chapter.

# Chapter 5

# Magnetosphere-ionosphere coupling

## 5.1   Introduction

The relationship between the dust-plasma interaction and the magnetosphere-ionosphere coupling is discussed from the magnetospheric ion speed in cosideration of the ionospheric conductivity in this chapter.

It is known that the Saturn's magnetospheric ion speed is slower than the co-roation speed. Past observation of Voyager and Cassini showed that the ion velocity was about 50-80% of the co-rotation speed in the inner magnetosphere [*Bridge et al.*, 1981, 1982; *Richardson*, 1986, 1998; *Wilson et al.*, 2008, 2009; *Wahlund et al.*, 2009; *Thomsen et al.*, 2010; *Morooka et al.*, 2011; *Holmberg et al.*, 2012]. Recent obserbations by the LP onboard Cassini especially showed that the ion speeds are close to the Keplerian velocity [*Wahlund et al.*, 2009; *Morooka et al.*, 2011; *Holmberg et al.*, 2012]. *Wahlund et al.* [2009] suggested that the charged dust particles in the E ring affect the plasma dynamics including the ion velocity.

In some models, the deviation from the co-rotation speed were explained in the middle magnetosphere [*Hill*, 1979; *Saur et al.*, 2004]. *Saur et al.* [2004] showed that it is accounted by radial mass transport and magnetospheric conductance in their model and the ion speeds are less than the co-rotation speed beyond 5 $R_S$. In the latest model, *Sakai et al.*

[2013] (Section 3 of this thesis) suggested that the ion speeds are less than the co-rotation speed as a result of the magnetospheric electric field generated through ion-dust collisions.

## 5.2 Magnetosphere-ionosphere coupling model

### 5.2.1 Ionospheric model

The ionospheric MHD model suggested in section 4.2 (eqs.(4.1)-(4.6)) was used. The plasma densities were calculated at $L$ =3 (Lat.=54.7), 5 (63.4), 7 (67.8) and 9 (70.5). The magnetospheric plasma density and temperature were evaluated to investigate how the magnetospheric plasma affects the ionosphere as with section 4.2.2. The densities are shown in Table 5.1 and Fig.3.2. The magnetospheric electron temperature is 2 eV at each $L$. The background neutral atmosphere profile given in section 4.3.1 (Fig.4.1) was used.

Table 5.1: Plasma densities in the equatorial region at each L.

|  | Electron [m$^{-3}$] | Dust [m$^{-3}$] | Proton [m$^{-3}$] | Water group ion [m$^{-3}$] |
|---|---|---|---|---|
| $L = 3$ | $1.6 \times 10^7$ | $1.1 \times 10^5$ | $6.1 \times 10^6$ | $2.4 \times 10^7$ |
| $L = 5$ | $3.7 \times 10^7$ | $1.1 \times 10^5$ | $1.0 \times 10^7$ | $4.2 \times 10^7$ |
| $L = 7$ | $1.8 \times 10^7$ | $5.9 \times 10^3$ | $3.7 \times 10^6$ | $1.5 \times 10^7$ |
| $L = 9$ | $9.2 \times 10^6$ | $5.9 \times 10^2$ | $1.9 \times 10^6$ | $7.4 \times 10^6$ |

### 5.2.2 Inner magnetospheric model

The ion velocities were calculated by using a multi-fluid model as with section 3.2 and a dominant equation was equation (3.6). The calculated Pedersen conductivity was substituted into $\Sigma_i$ of a equation (3.16). The density profile of Fig.3.2 as the magnetospheric plasma density, 2 eV as a temperature and 1 R$_S$ as a thickness of dust distribution, $D$ were used in this model.

## 5.3    Results

Fig.5.1-Fig.5.4 show the ionospheric plasma density profiles at each $L$ with respect to the local time. Fig.5.1 indicates 12 LT, Fig.5.2 indicates 18 LT, Fig.5.3 indicates 0 LT and Fig.5.4 indicates 6 LT, and the electron density was the highest at $L = 3$ and the peak density was $5.7 \times 10^9$ m$^{-3}$ at 12 LT. The density decreased as the distance from Saturn was large and the peak density was $4.1 \times 10^9$ m$^{-3}$ at $L = 9$. The electron density was the day, dusk, night and dawn in the order of largest to smallest.
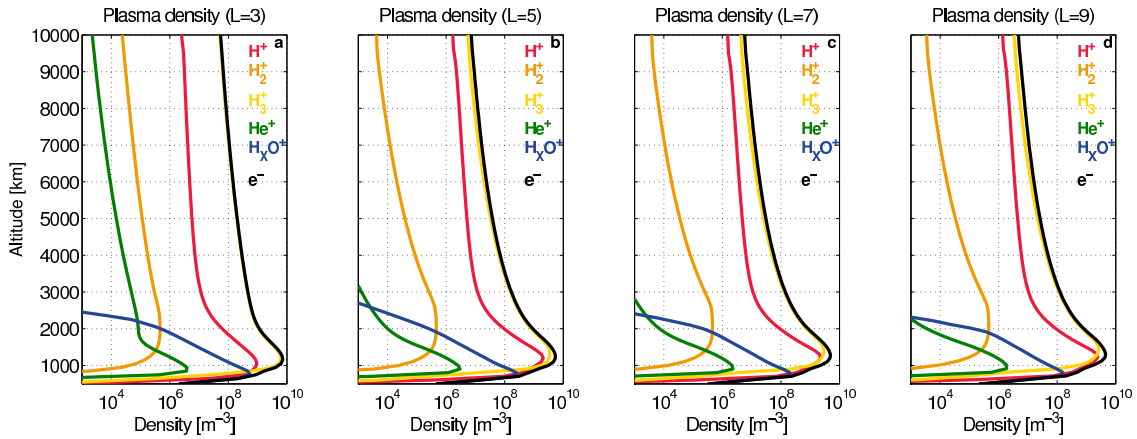


Figure 5.1: Plasma density profiles at 12 LT in each L. Red line indicates H$^+$, orange line indicates H$_2^+$, yellow line indicates H$_3^+$, green line indicates He$^+$, blue line indicates H$_X$O$^+$ and black line indicates electron. (a) L=3, (b) L=5, (c) L=7 and (d) L=9.

The ionospheric Pedersen conductivities were calculated at $L =$3, 5, 7 and 9 by using equations (4.14) and (4.15). Fig.5.5 shows the ionospheric integrated Pedersen conductivity estimated from the ionospheric plasma densities at $L =$3, 5, 7 and 9 and their fitting curves. The Pedersen conductivity depended on the local time and it was the largest on day time. This tendency is similar to the ionospheric plasma density profile. The Pedersen conductivity was also large when the distance from Saturn was small. At 12 LT it was 1.7 S at $L = 3$, 0.77 S at $L = 5$, 0.46 S at $L = 7$ and 0.37 S at $L = 9$. The fitting curves for the Pedersen conductivity in local time were estimated by the method of least squares since the Pedersen conductivities at each $L$ are needed to calculate the
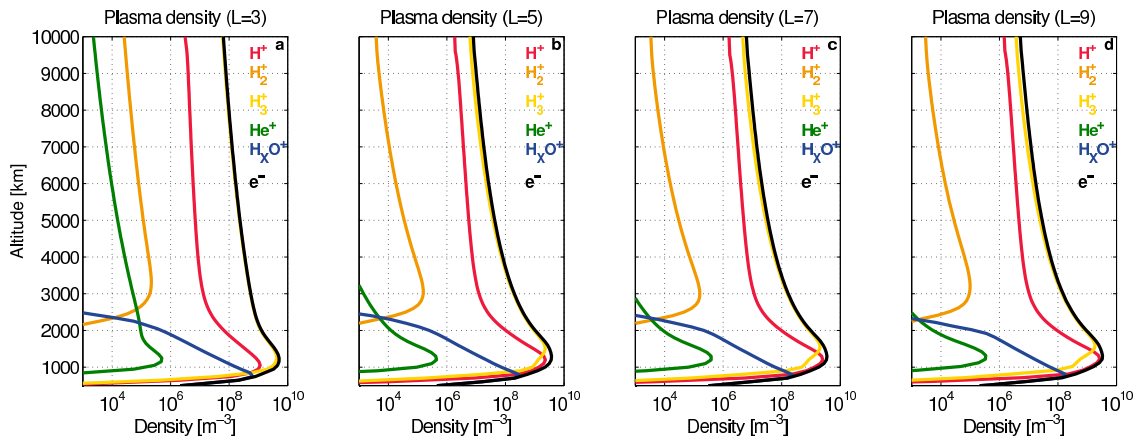
Figure 5.2: Plasma density profiles at 18 LT in each L. Colors are same as Fig.5.1.
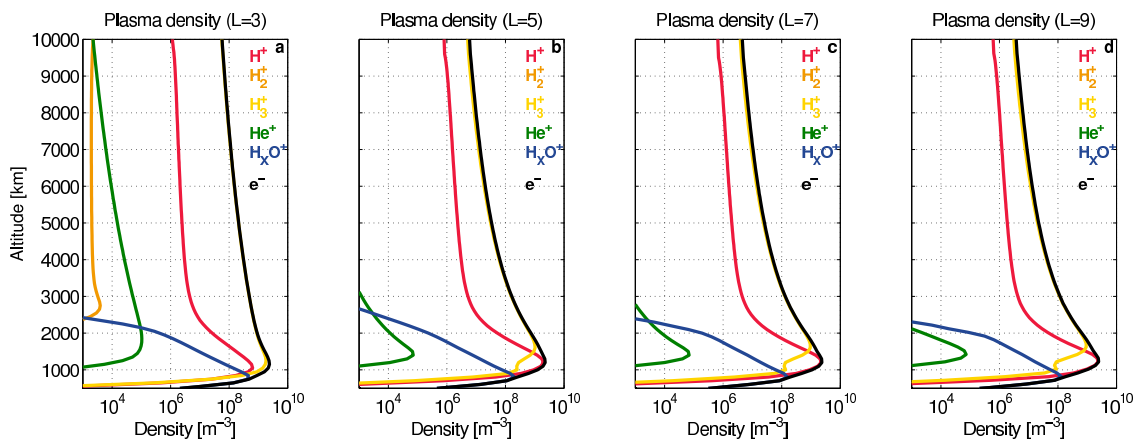
Figure 5.3: Plasma density profiles at 0 LT in each L. Colors are same as Fig.5.1.
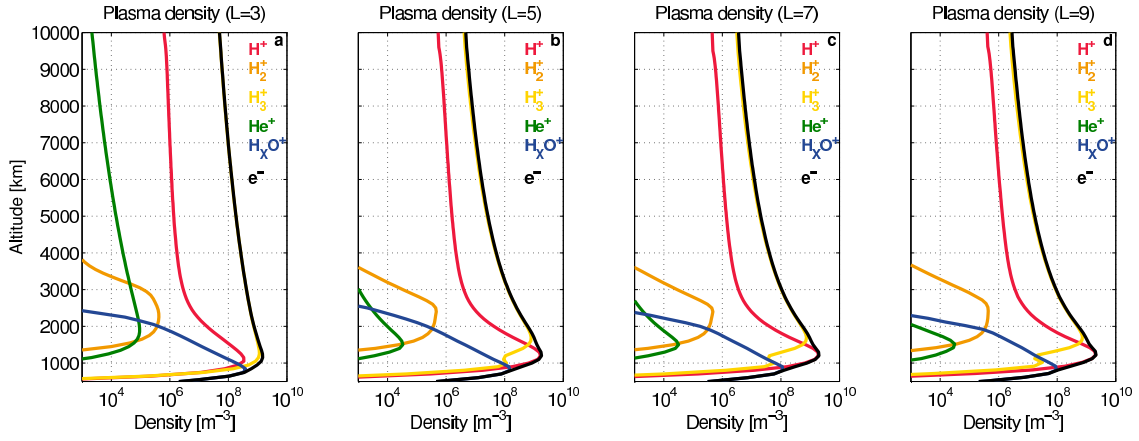
Figure 5.4: Plasma density profiles at 6 LT in each L. Colors are same as Fig.5.1.

ion velocity in the inner magnetosphere.

$$\Sigma_i \sim 7.1206 L^{-1.311} \qquad \text{at 12 LT} \tag{5.1}$$

$$\Sigma_i \sim 7.0260 L^{-1.377} \qquad \text{at 18 LT} \tag{5.2}$$

$$\Sigma_i \sim 4.6764 L^{-1.397} \qquad \text{at 0 LT} \tag{5.3}$$

$$\Sigma_i \sim 3.6729 L^{-1.418} \qquad \text{at 6 LT.} \tag{5.4}$$

The Pedersen conductivity varies with $L$ to the power of about -1.3. The ion velocity in the inner magnetosphere was calculated by fitting the function of the Pedersen conductivity.

The calculated ion velocity is almost the co-rotation speed within 3.5 $R_S$, and it starts to decrease from the ideal co-rotation speed outside 3.5 $R_S$ (Fig.5.6). The ion velocity is 60-80% of the ideal co-rotation speed in the plasma disk. This is since the magnetospheric electric field is smaller than the co-rotational electric field when the current due to the ion-dust collision flows in the inner magnetosphere. On the other hand, a small current flows within 3.5 $R_S$ because of less density and newly created electric field is also small. Thus, the ion velocty is the co-rotation speed within 3.5 $R_S$. The color of Fig.5.6 shows the difference of local time. The ion velocity is the fastest on day time and the slowest on dawn time. This is determined by the magnitude of Pedersen conductivity. On day time, the Pedersen conductivity is large, thus newly created magnetospheric electric field is
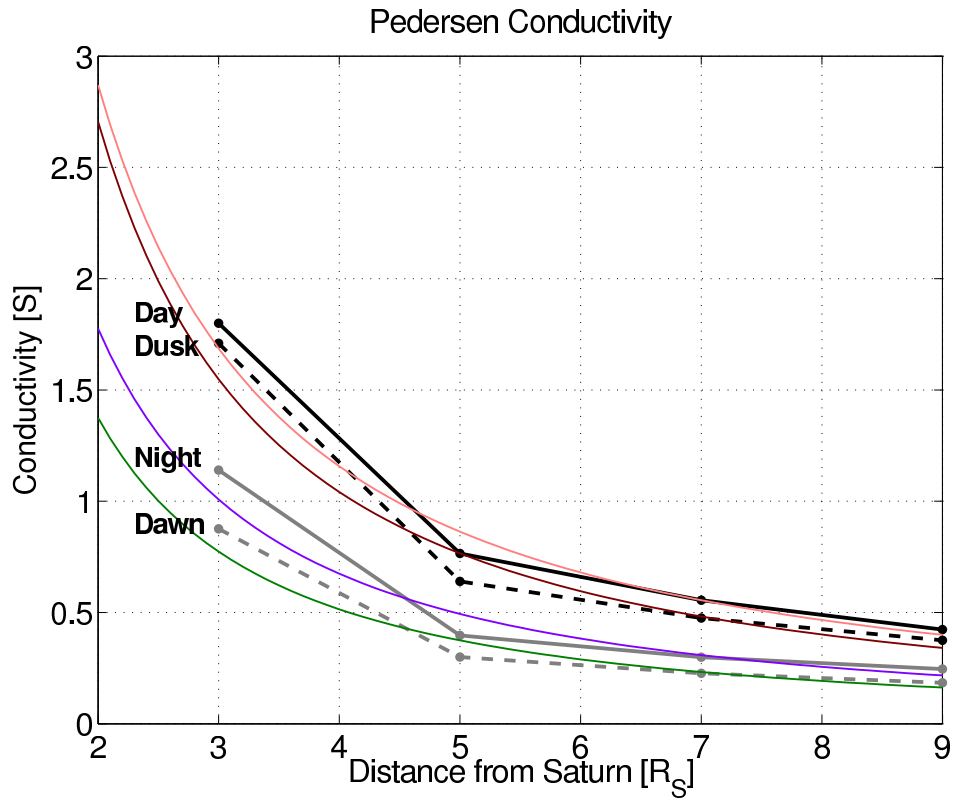
Figure 5.5: Integrated Pedersen conductivities in each L and their fitting curve. Black solid line indicates 12 LT, black dashed line indicates 18 LT, grey solid line indicates 0 LT and grey dashed line indicates 6 LT. The fitting curves are pink for day, brown for dusk, purple for night and green for dawn.

small since the electric field is inversely proportional to the conductivity (equation (3.16)). The ion velocity approaches the co-rotation speed since the newly created magnetospheric electric field is relatively small on day time. On the other hand, the ion velocity decreases if the conductivity is small on dawn time, since newly created electric field is larger. The ion velocity strongly depends on the Pedersen conductivity and it is slower when the conductivity is small. It means that the magnetosphere-ionosphere coupling is remarkably important for the dust-plasma interaction.
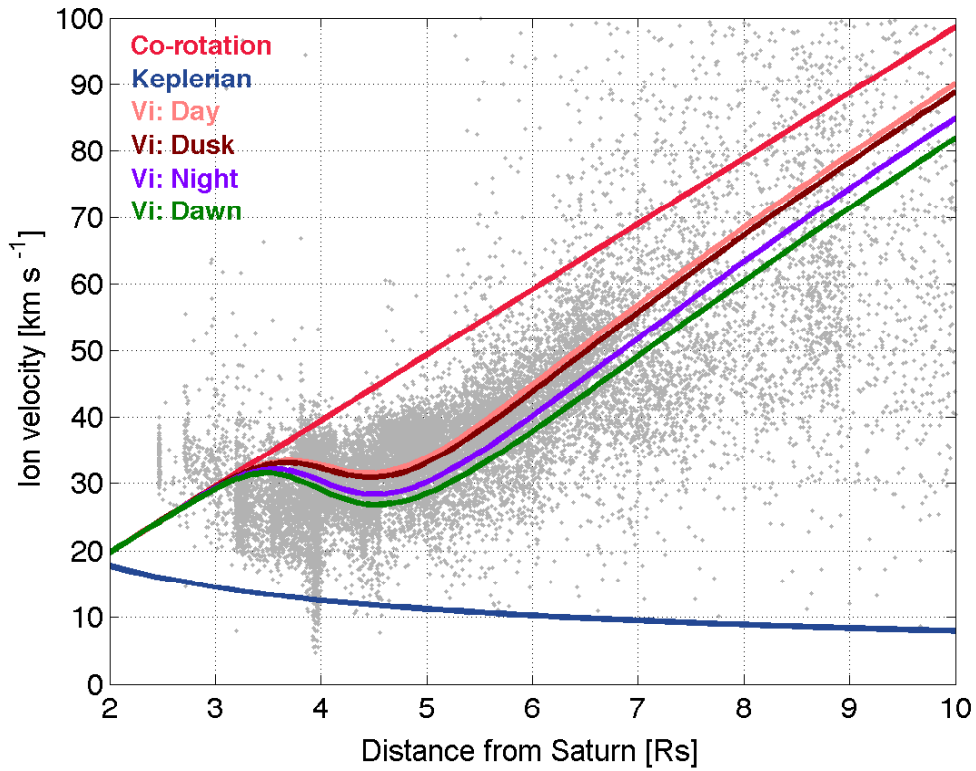


Figure 5.6: Comparisons between modeling results and RPWS/LP observations. Ion velocities are superposed on the LP observations from *Holmberg et al* [2012] when the dust density at 2 $R_S$ is $6.4 \times 10^4$ m$^{-3}$. Grey dots are observation points, red line indicates the ideal co-rotation speed, and blue line indicates the Keplerian speed. Pink, brown, purple and green lines indicate ion velocities at 12 LT, 18 LT, 0 LT and 6 LT, respectively.

## 5.4   Discussion

The magnetospheric ion velocity was calculated by using the calculated Pedersen conductivity. Our results showed that the ion velocity was slower when the Pedersen conductivity was small since newly created magnetospheric electric field was large.

Fig.5.6 shows that the ion velocities are superposed on ion observations by the LP onboard Cassini [*Holmberg et al.*, 2012]. The ion speeds from observations are dispersed on same $L$. It is suggested that this dispersion could show the dependence of local time. The ion velocity becomes fast during the solar irradiation since the Pedersen conductivity is large, while it becomes slow after the sunset because of the small conductivity. The ion velocity strongly depends on the Pedersen conductivity and the conductivity depends on the local time. Accordingly, the ion velocity should also depend on the local time.

## 5.5   Summary

The magnetospheric ion drift velocity was calculated by considering the ionospheric Pedersen conductivity. The ionospheric plasma densities were found at $L =$ 3, 5, 7 and 9 to estimate the Pedersen conductivity. The plasma density was the largest at $L = 3$ and it decreased as the distance from Saturn was large. The plasma density also depended on the local time, and it was the maximum value on day time and the minimum value on dawn time. The Pedersen conductivity was estimated from the plasma densities. It was the largest at $L = 3$ and it decreased as the distance from Saturn was large. The conductivity changed in local time, and the maximum was on the day time and the minimum was on the dawn time along with the plasma density profile.

The calculated ion velocity was almost the co-rotation speed within 3.5 $R_S$, and it decreased from the ideal co-rotation speed outside 3.5 $R_S$. The ion velocity was 60-80% of the co-rotation speed in the inner magnetosphere. The ion velocity was smaller than the co-rotation speed since the magnetospheric electric field is smaller than the co-rotational

electric field when the current due to the ion-dust collision flows in the inner magnetosphere. The ion velocity strongly depended on the local time since the conductivity also depended on the local time, and it was large on day time and it became small on dawn time. It is suggested that the dispersion of the observed speeds could show the dependence of local time. The ion velocity is fast during the solar irradiation since the Pedersen conductivity is large, while it becomes slow after the sunset because of the small conductivity.

The ionospheric conductivity strongly affects the ion velocity in the inner magnetosphere. The magnetosphere-ionosphere coupling is significantly important for the dust-plasma interaction and both of them are dominant in the Saturn's inner magnetospheric physics.

# Chapter 6

# Summary of this thesis

General introduction of Saturn's ionosphere, inner magnetosphere and dusty plasma is described in Chapter 1. Dusty plasma distribution of the Enceladus plume is described in Chapter 2. The condition of occurring the dust-plasma interaction in the inner magnetosphere was shown in Chapter 3, the relationship of the dusty plasma with the ionospheric plasma was discussed in Chapter 4 and 5. In this chapter, results in this thesis are summarized.

## Dusty plasma distribution in the Enceladus' plume

The horizontal diameter of the plume was about 3.8 $R_E$ at the low altitudes and increased to about 8.4 $R_E$ at high altitudes. At the high altitudes the plume extended to about 3 $R_E$ in the downstream. This may be indicating that the plume ions are affected by the co-rotation electric field and drifting in the direction. The ion densities were generally higher in the plume than the background plasma densities and they are two orders of magnitudes larger (maximum was about $10^4$ cm$^{-3}$) than the background at low altitudes. At high altitudes they were only slightly higher than the outside plume plasma densities. The electron density was, while, smaller than the background plasma density and the ion density. The density ratio of the electron to the ion was small at low altitude and about 0.01. The dust density was estimated to be about 20 cm$^{-3}$ from the observed density differences of the electron and the ion and assuming a certain dust distribution

with size of > 30 nm. The electron temperature was hotter ($\sim$4 eV) in the plume at the low altitudes, and it decreased to about 0.1 eV with increasing the altitude. The hotter photoelectron escaped from the plume gas was observed at low altitudes, and the electron cooled by collisions in the plume was found at high altitudes. The dust surface potential was generally negative and it became much less than a few V negative at low altitudes. This could be since a large amount of negative charge carriers are existence near Enceladus. The ion speed was near Keplerian speed in the plume.

Comparing with the results from the earlier observations by *Morooka et al.* [2011] the observed parameters were different. The general plasma densities of the plume in this study were smaller than the densities obtained by *Morooka et al.* [2011]. This can be due to the temporal activity of the tiger stripe.

## Ion velocity in the inner magnetosphere

The ion drift speed was calculated by using a multi-species fluid model (i.e., protons, water group ions, electrons, and charged dust) in order to examine the effect of dust on ion speed. In agreement with the LP observations, the modeling results showed that the ion speeds are less than the co-rotation speed. The dust-plasma interaction occurs through magnetosphere-ionosphere coupling. The inner magnetospheric total current along a magnetic field line weakens the dynamo electric field in Saturn's ionosphere. The ion speeds approach the Keplerian speed due to the large total current when the ion and dust densities are large. The dust-plasma interaction is significant when the thickness of the dust distribution is large and/or the density of ions and dusts is high.

## Ionospheric conductivity estimated from plasma density

The plasma density, velocity and temperature were calculated by using a MHD model in order to investigate the ionospheric Pedersen conductivity. The plasma density was about $10^9$ m$^{-3}$ at the altitude of 1200 km, and it decreased to about $10^7$ m$^{-3}$ at the

altitude of 10000 km. The dominant ion was $H_3^+$ between 1000 and 10000 km, and it was $H_2O^+$ below 1000 km. The $H^+$ has the upward velocity below 10000 km, while heavy ions have zero or downward velocity. This might be due to the difference of mass. The electron temperature was 140 K at the lower boundary and it increased to 20000 K at the altitude of 10000 km. This is since the heat flow significantly affects the electron temperature. The electron temperature was about 2000 K at the altitude of 1000 km, and the collision and joule heating were important below 2000 km. The electron density changed between about $10^8$ and $10^{10}$ $m^{-3}$ below 2000 km and it became the maximum around 14 LT. Above 2000 km it became the maximum around 18 LT. The minimum is around 6 LT at all altitudes. The electron density decreased with increasing the altitude. The electron temperature didn't basically depend on the local time, and it decreased with increasing the altitude. The conductivity was the maximum 0.77 S on day time and the minimum 0.30 S on dawn time. The Pedersen conductivity significantly depends on the plasma density in the ionosphere.

## Magnetospheric ion velocity in consideration of the ionospheric conductivity

The magnetospheric ion drift velocity was calculated in consideration of the ionospheric Pedersen conductivity. The ionospheric plasma density at $L =$ 3, 5, 7 and 9 were evaluated to estimate the Pedersen conductivity. The plasma density was the largest at $L = 3$ and it decreased as the distance from Saturn was large. The plasma density also depended on the local time, and it was the maximum value on day time and the minimum value on dawn time. The Pedersen conductivity was estimated from the plasma density. It was the largest at $L = 3$ and it decreased as the distance from Saturn was large. The conductivity changed in local time, and the maximum was on the day time and the minimum was on the dawn time along with the plasma density profile.

The calculated ion velocity was almost the co-rotation speed within 3.5 $R_S$, and it decreased from the ideal co-rotation speed outside 3.5 $R_S$. The ion velocity was 60-80% of the co-rotation speed in the inner magnetosphere. The ion velocity was smaller than the

co-rotation speed since the magnetospheric electric field is smaller than the co-rotational electric field when the current due to the ion-dust collision flows in the inner magnetosphere. The ion velocity strongly depended on the local time since the conductivity also depended on the local time, and it was large on day time, while it became small on dawn time. It is suggested that the dispersion of the observed speeds could show the dependence of local time. The ion velocity is fast during the solar irradiation since the Pedersen conductivity is large, while it becomes slow after the sunset because of the small conductivity.

## At the end of this thesis

The magnetosphere-ionosphere coupling is significantly important for the dust-plasma interaction. The dust-plasma interaction significantly occurs when the dust density is high and/or the thickness of dust distribution is large. The current along the field line weakens the ionospheric dynamo electric field when the current flows in the magnetosphere through the ion-dust collision, and thus the ion velocity is the slower than the co-rotation speed. However, the electric field depends on not only the current but also the ionospheric conductivity. Newly created electric field becomes large if the Pedersen conductivity is small, and total electric field decreases from the co-rotational field. Thus, the ionospheric conductivity strongly affects the ion velocity in the inner magnetosphere. It is impossible to understand the dust-plasma interaction in Saturn's inner magnetosphere without understanding of the Saturn's ionosphere, because the magnetosphere and ionosphere is intimately-connected. We could discuss the dust-plasma interaction by understanding the Saturn's ionosphere.

# Bibliography

Anicich, V. G. (1993), Evaluated bimolecular ion-molecule gas phase kinetics of positive ions for use in modeling planetary atmospheres, cometary comae, and interstellar clouds, *J. Phys. Chem. Ref. Data*, **22**, 1469-1569, doi:10.1063/1.555940.

Atreya, S., and T. M. Donahue (1975), The role of hydrocarbons in the ionospheres of the outer planets, *Icarus*, **25**, 335-338, doi:10.1016/0019-1035(75)90027-5.

Baum, W. A., T. Kreidl, J. A. Westphal, G. E. Danielson, P. K. Seidelmann, D. Pascu, and D. G. Currie (1981), Saturn's E ring: I. CCD observations of March 1980, *Icarus*, **47**, 84-96, doi:10.1016/0019-1035(81)90093-2.

Bettinger, R. T., and E. H. Walker (1965), Relationship for plasma sheaths about Langmuir probe, *Phys. Fluids*, **8**, 748-751, doi:10.1063/1.1761293.

Blanc, M. F., R. Kallenbach, and N. V. Erkaev (2005), Solar system magnetospheres, *Space Sci. Rev.*, **116**, 227-298, doi:10.1007/s11214-005-1958-y.

Burger, M. H., E. C. Sittler Jr., R. E. Johnson, H. T. Smith, O. J. Tucker, and V. I. Shematovich (2007), Understanding the escape of water from Enceladus, *J. Geophys. Res.*, **112**, A06219, doi:10.1029/2006JA012086.

Bridge, H. S., J. W. Belcher, A. J. Lazarus, S. Olbert,J. D. Sullivan, F. Bagenal, P. R.

Gazis, R. E. Hartle, K. W. Ogilvie, J. D. Scudder, E. C. Sittler, A. Eviatar, G. L. Siscoe, C. K. Goertz, and V. M. Vasyliunas (1981), Plasma observations near Saturn - Initial results from Voyager 1, *Science*, **212**, 217-224, doi:10.1126/science.212.4491. 217.

Bridge, H. S., F. Bagenal, J. W. Belcher, A. J. Lazarus, R. L. McNutt, J. D. Sullivan, P. R. Gazis, R. E. Hartle, K. W. Ogilvie, J. D. Scudder, E. C. Sittler, A. Eviatar, G. L. Siscoe, C. K. Goertz, and V. M. Vasyliunas (1982), Plasma observations near Saturn - Initial results from Voyager 2, *Science*, **215**, 563-570, doi:10.1126/science.215.4532.563.

Brown, R. H., L. A. Soderblom, J. M. Soderblom, R. N. Clark, R. Jaumann, J. W. Barnes, C. Sotin, B. Buratti, K. H. Baines, and P. D. Nicholson (2008), The identification of liquid ethane in Titan's Ontario Lacus, *Nature*, **454**, 607-610, doi:10.1038/nature07100.

Cheng, A. F., and J. H. Waite Jr. (1988), Corotation lag of Saturn's magnetosphere: Global ionospheric conductivites revisited, *J. Geophys. Res.*, **93**, 4107-4109, doi:10.1029/JA093iA05p04107.

Connerney, J., M. H. Acuña, and N. F. Ness (1983), Currents in Saturn's magnetosphere, *J. Geophys. Res.*, **88**, 8779-8789, doi:10.1029/JA088iA11p08779.

Connerney, J. E. P., and J. H. Waite Jr. (1984), New model of Saturn's ionosphere with an influx of water from the rings, *Nature*, **312**, 136-138, doi:10.1038/312136a0.

Cowley, S. W. H., and E. J. Bunce (2003), Corotation-driven magnetosphere-ionosphere coupling currents in Saturn's magnetosphere and their relation to the auroras, *Ann.*

*Geophys.*, **21**, 1691-1707, doi:10.5194/angeo-21-1691-2003.

Cowley, S. W. H., E. J. Bunce, and J. M. O'Rourke (2004), A simple quantitative model of plasma flows and currents in Saturn's polar ionosphere, *J. Geophys. Res.*, **109**, A05212, doi:10.1029/2003JA010375.

Cravens, T. E., N. Ozak, M. S. Richard, M. E. Campbell, I. P. Robertson, M. Perry, and A. M. Rymer (2011), Electrons energetics in the Enceladus torus, *J. Geophys. Res.*, **116**, A09295, doi:10.1029/2011JA016498.

Dermott, S. F., and C. Sagan (1995), Tidal effects of disconnected hydrocarbon seas on Titan., *Nature*, **374**, 238-240, doi:10.1038/374238a0.

de Pater, I., and J. J. Lissauer (2001), *Planetary Sciences*, Cambridge University Press, Cambridge, UK.

Dong, Y., T. W. Hill, B. D. Teolis, B. A. Magee, and J. H. Waite (2011), The water vapor plumes of Enceladus, *J. Geophys. Res.*, **116**, A10204, doi:10.1029/2011JA016693.

Dougherty, M. K., K. K. Khurana, F. M. Neubauer, C. T. Russell, J. Saur, J. S. Leisner, and M. E. Burton (2006), Identification of a dynamic atmosphere at Enceladus with the Cassini Magnetometer, *Science*, **311**, 1406-1409, doi:10.1126/science.1120985.

Dragt, A. J. (1961), Effect of hydromagnetic waves on the lifetime of Van Allen radiation protons, *J. Geophys. Res.*, **66**, 1641-1649, doi:10.1029/JZ066i006p01641.

Dressler, R. A., M. J. Bastian, D. J. Levandier, and E. Murad (2006), Emperical model of the state-state dynamics in near-resonant hyperthermal $X^+ + H_2O$ charge-transfer

reactions, *Int. J. Mass Spectrom.*, **159**, 245-256, doi:10.1016/S0168-1176(96)04454-0.

Esposito, L. W., J. E. Colwell, K. Larsen, W. E. McClintock, A. I. F. Stewart, J. T. Hallett, D. E. Shemansky, J. M. Ajello, C. J. Hansen, A. R. Hendrix, R. A. West, H. U. Keller, A. Korth, W. R. Pryor, R. Reulke, and Y. L. Yung (2005), Ultraviolet imaging spectroscopy shows an active Saturnian system, *Science*, **307**, 1251-1255, doi:10.1126/science.1105606.

Eviatar, A., and J. Richardson (1986), Corotation of the Kronian magnetosphere, *J. Geophys. Res.*, **91**, 3299-3303, doi:10.1029/JA091iA03p03299.

Fahleson, U., C. -G. Fälthammar, and A. Pedersen (1974), Ionospheric temperature and density measurements by means of spherical double probes, *Planet. Space Sci.*, **22**, 41-66, doi:10.1016/0032-0633(74)90122-6.

Farrell, W. M., W. S. Kurth, D. A. Gurnett, R. E. Johnson, M. L. Kaiser, J. -E. Wahlund, and J. -H. Waite Jr. (2009), Electron density dropout near Enceladus in the context of water-vapor and water-ice, *Geophys. Res. Lett.*, **36**, L10203, doi:10.1029/2008GL037108.

Fortov, V. E., A. V. Ivlev, S. A. Khrapak, A. G. Khrapak, and G. E. Morfill (2005), Complex (dusty) plasmas: Current status, open issues, perspectives, *Phys. Rep.*, **421**, 1-103, doi:10.1016/j.physrep.2005.08.007.

Gérard, J. -C., B. Bonfond, J. Gustin, D. Grodent, J. T. Clarke, D. Bisicalo, and V. Shematovich (2009), Altitude of Saturn's aurora and its implications for the characteristic energy of precipitated electrons, *Geophys. Res. Lett.*, **36**, L02202,

doi:10.1029/2008GL036554.

Glocer, A., T. I. Gombosi, G. Toth, K. C. Hansen, A.J. Ridley, and A. Nagy (2007), Polar wind outflow model: Saturn results, *J. Geophys. Res.*, **112**, doi:10.1029/2006JA011755.

Goertz, C. K. (1989), Dusty plasmas in the solar system, *Rev. Geophys.*, **27**, 271-292, doi:10.1029/RG027i002p00271.

Goertz, C. K., M. F. Thomsen, and W. -H. Ip (1981), Saturn's radio emissions: rotational modulation, *Nature*, **292**, 737-739, doi:10.1038/292737a0.

Gurnett, D. A., W. S. Kurth, D. L. Kirchner, G. B. Hospodarsky, T. F. Averkamp, P. Zarka, A. Lecacheux, R. Manning, A. Roux, P. Canu, N. Cornilleau-Wehrlin, P. Galopeau, A. Meyer, R. Bostrm, G. Gustafsson, J. -E. Wahlund, L. Ahlen, H. O. Rucker, H. P. Ladreiter, W. Macher, L. J. C. Woolliscroft, H. Alleyne, M. L. Kaiser, M. D. Desch, W. M. Farrell, C. C. Harvey, P. Louarn, P. J. Kellogg, K. Goetz, and A. Pedersen (2004), The Cassini radio and plasma wave investigation, *Space Sci. Rev.*, **114**, 395-463, doi:10.1007/s11214-004-1434-0.

Gurnett, D. A., A. M. Persoon, W. S. Kurth, J. B. Groene, T. F. Averkamp, M. K. Dougherty, and D. J. Southwood (2007), The variable rotation period of the inner region of Saturn's plasma disk, *Science*, **316**, 442-445, doi:10.1126/science.1138562.

Gustafsson, G., and J. -E. Wahlund (2010), Electron temperatures in Saturn's plasma disc, *Planet. Space Sci.*, **58**, 1018-1025, doi:1016/j.pss.2010.03.007.

Haff, P. K., G. L. Siscoe, and A. Eviatar (1983), Ring and plasma - The enigmae of
    Enceladus, *Icarus*, **56**, 426-438, doi:10.1016/0019-1035(83)90164-1.


Hill, T. W. (1979), Inertial limit on corotation, *J. Geophys, Res.*, **84**, 6554-6558, doi:10.10
    29/JA084iA11p06554.


Hill, T. W., M. F. Thomsen, R. L. Tokar, A. J. Coates, G. R. Lewis, D. T. Young, F.
    J. Crary, R. A. Baragiola, R. E. Johnson, Y. Dong, R. J. Wilson, G. H. Jones, J.
    -E. Wahlund, D. G. Mitchell, and M. Horányi (2012), Charged nanograins in the
    Enceladus plume, *J. Geophys. Res.*, **117**, A05209, doi:10.1029/2011JA017218.


Holmberg, M. K. G., J. -E. Wahlund, M. W. Morooka, and A. M. Persoon, Ion densities
    and velocities in the inner plasma torus of Saturn (2012), *Planet. Space Sci.*, **73**,
    151-170, doi:10.1016/j.pss.2012.09.016.


Horányi, M., T. W. Hartquist, O. Havnes, D. A. Mendis, and G. E. Morfill (2004),
    Dusty plasma effects in Saturn's magnetosphere, *Rev. Geophys.*, **42**, RG4002,
    doi:10.1029/2004RG000151.


Horányi, M., A. Juhász, and G. E. Morfill (2008), Large-scale structure of Saturn's E-
    ring, *Geophys. Res. Lett.*, **35**, L04203, doi:10.1029/2007GL032726.


Huang, T., and T. Hill (1989), Corotation lag of the Jovian atmosphere, ionosphere and
    magnetosphere, *J. Geophys. Res.*, **94**, 3761-3765, doi:10.1029/JA094iA04p03761.


Huba, J. D., G. Joyce, and J. A. Fedder (2000), Sami2 is Another Model of the Ionosphere
    (SAMI2): A new low-latitude ionosphere model, *J. Geophys. Res.*, **105**, 23035-

23053, doi:10.1029/2000JA000035.

Hubbard, W. B. (1980), Interiors of the giant planets, *Science*, **214**, 145-149, doi:10.1126/science.214.4517.145.

Hubbard, W. B., T. Guillot, J. I. Lunine, A. Burrows, D. Saumon, M. S. Marley, and R. S. Freedman (1997), Liquid metallic hydrogen and the structure of brown dwarfs and giant planets, *Phys. Plasmas*, **4**, 2011-2015, doi:10.1063/1.872570.

Itikawa, Y., and N. Mason (2005), Cross sections for electron collisions with water molecules, *J. Phys. Chem. Ref. Data*, **34**, 1, doi:10.1063/1.1799251.

Jones, G. H., C. S. Arridge, A. J. Coates, G. R. Lewis, S. Kanani, A. Wellbrock, D. T. Young, F. J. Crary, R. L. Tokar, R. J. Wilson, T. W. Hill, R. E. Johnson, D. G. Mitchell, J. Schmidt, S. Kempf, U. Beckmann, C. T. Russell, Y. D. Jia, M. K. Dougherty, J. H. Waite Jr., and B. A. Magee (2009), Fine jet structure of electrically charged grains in Enceladus' plume, *Geophys. Res. Lett.*, **36**, L16204, doi:10.1029/2009GL038284.

Jurac, S., R. E. Johnson, and J. D. Richardson (2001), Saturn's E ring and production of the neutral torus, *Icarus*, **149**, 384-396, doi:10.1006/icarus.2000.6528.

Kane, M., D. G. Mitchell, J. F. Carbary, S. M. Krimigis, and F. J. Crary (2008), Plasma convection in Saturn's outer magnetosphere determined from ions detected by the Cassini INCA experiment, *Geophys. Res. Lett.*, **35**, L04102, doi:10.1029/2007GL032342.

Kempf, S., U. Beckmann, R. Srama, M. Horányi, S. Auer, and E. Grün (2006), The elec-
    trostatic potential of E ring particles, *Planet. Space Sci.*, **54**, 999-1006, doi:10.1016
    /j.pss.2006.05.012.

Kempf, S., U. Beckmann, G. Moragas-Klostermeyer, F. Postberg, R. Srama, T. Economou,
    J. Schmidt, F. Spahn, and E. Grün (2008), The E ring in the vicinity of Enceladus.
    I. Spatial distribution and properties of the ring particles, *Icarus*, **193**, 420-437,
    doi:10.1016/j.icarus.2007.06.027.

Khrapak, S. A., A. V. Ivlev, and G. E. Morfill (2004), Momentum transfer in complex
    plasmas, *Phys. Rev.*, **70**, 056405, doi:10.1103/PhysRevE.70.056405.

Kim, Y. H., and J. L. Fox (1994), The chemistry of hydrocarbon ions in the Jovian
    ionosphere, *Icarus*, **112**, 310-325, doi:10.1006/icar.1994.1186.

Kliore, A. J., I. R. Patel, G. F. Lindal, D. N. Sweetnam, H. B. Hotz, J. H. Waite,
    Jr., and T. R. McDonough (1980), Structure of the ionosphere and atmosphere of
    Saturn from Pioneer 11 Saturn radio occultation, *J. Geophys. Res.*, **85**, 5857-5870,
    doi:10.1029/JA085iA11p05857.

Kliore, A. J., J. D. Anderson, J. W. Armstrong, S. W. Asmar, C. L. Hamilton, N. J.
    Rappaport, H. D. Wahlquist, R. Ambrosini, F. M. Flasar, R. G. French, L. Iess, E.
    A. Marouf, and A. F. Nagy (2004), Cassini Radio Science, *Space Sci. Rev.*, **115**,
    1-70, doi:10.1007/1-4020-3874-7_1.

Kliore, A. J., A. F. Nagy, E. A. Marouf, A. Anabtawi, E. Barbinis, D. U. Fleischman,
    and D. S. Kahan (2009), Midlatitude and high-latitude electron density profiles
    in the ionosphere of Saturn obtained by Cassini radio occultation observations, *J.*

*Geophys. Res.*, **114**, A04315, doi:10.1029/2008JA013900.

Kurth, W. S., T. F. Averkamp, D. A. Gurnett, and Z. Wang (2006), Cassini RPWS observations of dust in Saturn's E ring, *Planet. Space Sci.*, **54**, 988-998, doi:10.1016/j.pss.2006.05.011.

Kurth, W. S., T. F. Averkamp, D. A. Gurnett, J. B. Groene, and A. Lecacheux (2008), An update to a Saturnian longitude system based on kilometric radio emissions, *J. Geophys. Rev.*, **113**, A05222, doi:10.1029/2007JA012861.

Lindal, G. F., D. N. Sweetnam, and V. R. Eshleman (1985), The atmosphere of Saturn: An analysis of the Voyager radio occultation measurements, *Astron. J.*, **90**, 1136-1146, doi:10.1086/113820.

Lindsay, B. G., D. R. Sieglaff, K. A. Smith, and R. F. Stebbings (1997), Charge transfer of 0.5-, 1.5-, and 5-keV protons with $H_2O$: Absolute differential and integral cross sections, *Phys. Rev. A*, **55**, 3945-3946, doi:10.1103/PhysRevA.55.3945.

Lishawa, C. R., R. A. Dressler, J. A. Gardner, R. H. Salter, and E. Murad (1990), Cross sections and product kinetic energy analysis of $H_2O^+$-$H_2O$ collisions at suprathermal energies, *J. Chem. Phys.*, **93**, 3196-3206, doi:10.1063/1.458852.

Lunine, J. I. (1993), Does Titan have an ocean - a review of current understanding of Titan's surface, *Rev. Geophys.*, **31**, 133-149, doi:10.1029/92RG02794.

Lunine, J. I. (1994), Does Titan have oceans?, *Am. Sci.*, **82**, 134-143.

Lunine, J. I., D, J. Stevenson, and Y. L. Yung (1983), Ethane ocean on Titan. *Science*, **222**, 1229-1230, doi:10.1126/science.222.4629.1229.

Matcheva, K. I., D. F. Strobel, and F. M. Flasar (2001), Interaction of gravity waves with ionospheric plasma: Implications for Jupiter's ionosphere, *Icarus*, **152**, 347-365, doi:10.1006/icar.2001.6631.

McAndrews, H. J., M. F. Thomsen, C. S. Arridge, C. M. Jackman, R. J. Wilson, M. G. Henderson, R. L. Tokar, K. K. Khurana, E. C. Sittler, A. J. Coates, and M. K. Dougherty (2009), Plasma in Saturn's nightside magnetosphere and the implications for global circulation, *Planet. Space Sci.*, **57**, 1714-1722, doi:10.1016/j.pss.2009.03.00 3.

McElroy, M. B. (1973), The ionospheres of the major planets, *Space Sci. Rev.*, **14**, 151-167, doi:10.1007/BF00214756.

Mendillo, M., L. Moore, J. Clarke, I. Müller-Wodarg, W. S. Kurth, and M. L. Kaiser (2005), Effects of ring shadowing on the detection of electrostatic discharges at Saturn, *Geophys. Res. Lett.*, **32**, L05107, doi:10.1029/2004GL021934.

Mendis, D. A. (1979), Dust in cosmic plasma environments, *Astrophys. Space Sci.*, **65**, 5-12, doi:10.1007/BF00643484.

Millar, T. J., P. R. A. Farquhar, and K. Willacy (1997), The UMIST database for astro-chemistry 1995, *Astron. Astrophys. Suppl. Set.*, **121**, 139-185, doi: 10.1051/aas:1997 118.

Millward, G. H., R. J. Moffett, W. Quegan, and T. J. Fuller-Rowell (1996), A Coupled Thermospheric-IonosphericPlasmasphere Model (CTIP), in *STEP: Handbook of Ionospheric Models*, edited by R. W. Schunk, pp. 239-279, Utah State University, Logan, Utah.

Moses, J. I., and S. F. Bass (2000), The effects of external material on the chemistry and structure of Saturn's ionosphere, *J. Geophys. Res.*, **105**, 7013-7052, doi:10.1029/1999JE001172.

Moses, J. I., B. Bézard, E. Lellouch, G. R. Gladstone, H. Feuchtgruber, and M. Allen (2000), Photochemistry of Saturn's atmosphere I. Hydrocarbon chemistry and comparisons with ISO observations, *Icarus*, **143**, 244-298, doi:10.1006/icar.1999.6270.

Moore, L., and M. Mendillo (2005), Ionospheric contribution to Saturn's inner plasmasphere, *J. Geophys. Res.*, **110**, A05310, doi:10.1029/2004JA010889.

Moore, L., and M. Mendillo (2007), Are plasma depletions in Saturn's ionosphere?, *Geophys. Res. Lett.*, **34**, L12202, doi:10.1029/2007GL029381.

Moore, L., M. Mendillo, I. C. F. Müller-Wodarg, and D. L. Murr (2004), Modeling of global variations and ring shadowing in Saturn's ionosphere, *Icarus*, **172**, 503-520, doi:10.1016/j.icarus.2004.07.007.

Moore, L., A. F. Nagy, A. J. Kliore, I. Müller-Wodarg, J. D. Richardson, and M. Mendillo (2006), Cassini radio occultations of Saturn's ionosphere: Model comparisons using a constant water flux, *Geophys. Res. Lett.*, **33**, L22202, doi:10.1029/2006GL027375.

Moore, L., M. Galand, I. Müller-Wodarg, R. Yelle, and M. Mendillo (2008), Plasma temperatures in Saturn's ionosphere, *J. Geophys. Res.*, **113**, A10306, doi:10.1029/2008J A013373.

Moore, L., M. Galand, I. Müller-Wodarg, and M. Mendillo (2009), Response of Saturn's ionosphere to solar radiation: Testing parameterizations for thermal electron heating and secondary ionization processes, *Planet. Space Sci.*, **57**, 1699-1705, doi:10.1016/j.pss.2009.05.001.

Moore, L., I. Müller-Wodarg, M. Galand, A. Kliore, and M. Mendillo (2010), Latitudinal variations in Saturn's ionosphere: Cassini measurements and model comparisons, *J. Geophys. Res.*, **115**, A11317, doi:10.1029/2010JA015692.

Morooka, M. W., J. -E. Wahlund, A. I. Eriksson, W. M. Farrell, D. A. Gurnett, W. S. Kurth, A. M. Persoon, M. Shafiq, M. André, and M. K. G. Holmberg (2011), Dusty plasma in the vicinity of Enceladus, *J. Geophys. Res.*, **116**, A12221, doi:10.1029/201 1JA017038.

Mott-Smith, H. M., and L. Langmuir (1926), The theory of collectors in gaseous discharges, *Phys. Rev.*, **28**, 727-763, doi:10.1103/PhysRev.28.727.

Müller-Wodarg, I. C. F., M. Mendillo, R. V. Yelle, and A. D. Aylward (2006), A global circulation model of Saturn's ionosphere, *Icarus*, **180**, 147-160, doi:10.1016/j.icarus.2 005.09.002.

Nagy, A. F., A. J. Kliore, E. Marouf, R. French, M. Flasar, N. J. Rappaport, A. Anabtawi, S. W. Asmar, D. Johnston, E. Barbinis, G. Goltz, and D. Fleischman (2006),

First results from the ionospheric radio occultations of Saturn by the Cassini spacecraft, *J. Geophys. Res.*, **111**, A06310, doi:10.1029/2005JA011519.

Nisbet, J. S. (1968), Photoelectron escape from the ionosphere, *J. Atmos. Terr. Phys.*, **30**, 1257-1278, doi:10.1016/S0021-9196(68)91090-8.

Pang, K. D., C. C. Voge, J. W. Rhoads, and J. M. Ajello (1984), The E ring of Saturn and satellite Enceladus, *J. Geophys. Res.*, **89**, 9459-9470, doi:10.1029/JB089iB11p09459.

Perry, J. J., Y. H. Kim, J. L. Fox, H. S. Porter (1999), Chemistry of the Jovian auroral ionosphere, *J. Geophys. Res.*, **104**, 16541-16565, doi:10.1029/1999JE900022.

Persoon, A. M., D. A. Gurnett, W. S. Kurth, G. B. Hospodarsky, J. B. Groene, P. Canu, and M. K. Dougherty (2005), Equatorial electron density measurements in Saturn's inner magnetosphere, *Geophys. Res. Lett.*, **32**, L23105, doi:10.1029/2005GL024294.

Persoon, A. M., D. A. Gurnett, W. S. Kurth, and J. B. Groene (2006), A simple scale height model of the lectron density in Saturn's plasma disk, *Geophys. Res. Lett.*, **33**, L18106, doi:10.1029/2006GL027090.

Persoon, A. M., D. A. Gurnett, O. Santolik, W. S. Kurth, J. B. Faden, J. B. Groene, G. R. Lewis, A. J. Coates, R. J. Wilson, R. L. Tokar, J. -E. Wahlund, and M. Moncuquet (2009), A diffusive equilibrium model for the plasma density in Saturn's magnetosphere, *J. Geophys. Res.*, **114**, A04211, doi:10.1029/2008JA013912.

Persoon, A. M., D. A. Gurnett, J. S. Leisner, W. S. Kurth, J. B. Grone, and J. B. Faden (2013), The plasma density distribution in the inner region of Saturn's magneto-

sphere, *J. Geophys. Res. Space Physics*, **118**, 2970-2974, doi:10.1002/jgra.501812.

Porco, C. C., P. Helfenstein, P. C. Thomas, A. P. Ingersoll, J. Wisdom, R. West, G. Neukum, T. Denk, R. Wagner , T. Roatsch, S. Kieffer, E. Turtle, A. McEwen, T. V. Johnson, J. Rathbun, J. Veverka, D. Wilson, J. Perry, J. Spitale, A. Brahic, J. A. Burns, A. D. DelGenio, L. Dones, C. D. Murray, S. Squyres (2006), Cassini observes the active south pole of Enceladus, *Science*, **311**, 1393-1401, doi:10.1126/science.1123 013.

Richardson, J. D. (1986), Thermal ions at Saturn: Plasma parameters and implications, *J. Geophys. Res.*, **91**, 1381-1389, doi:10.1029/JA091iA02p01381.

Richardson, J. D. (1998), Thermal plasma and neutral gas in Saturn's magnetosphere, *Rev. Geophys.*, **36**, 501-524, doi:10.1029/98RG01691.

Ross, M., H. C. Graboske, and W. J. Nellis (1981), Equation of state experiments and theory relevant to planetary modeling, *Phil. Trans. R. Soc. Lond. A*, **303**, 303-313, doi:10.1098/rsta.1981.0204.

Sagan, C., and S. F. Dermott (1982), The tide in the seas of Titan, *Nature*, **300**, 731-733, doi:10.1038/300731a0.

Sakai, S., S. Watanabe, M. W. Morooka, M. K. G. Holmberg, J. -E. Wahlund, D. A. Gurnett, and W. S. Kurth (2013), Dust-plasma interaction through magnetosphere-ionosphere coupling in Saturn's plasma disk, *Planet. Space Sci.*, **75**, 11-16, doi:10.101 6/j.pss.2012.11.003.

Saur, J., B. H. Mauk, A. Ka$\beta$ner, and F. M. Neubauer (2004), A model for the az-imuthal plasma velocity in Saturn's magnetosphere, *J. Geophys. Res.*, **109**, A05217,

doi:10.1029/2003JA010207.

Schunk, R. W., and A. F. Nagy (2009), Ionization and energy exchange processes in *Ionospheres: Physics, Plasma Physics, and Chemistry*, edited by J. T. Houghton, M. J. Rycroft, and A. J. Dessler, Cambridge University Press, The Edinburgh Building, Cambridge CB2 8RU, Cambridge, England, United Kingdom, pp.254-288.

Shafiq, M., J. -E. Wahlund, M. W. Morooka, W. S. Kurth, and W. M. Farrell (2011), Characteristics of the dust-plasma interaction near Enceladus' South Pole, *Planet. Space. Sci.*, **59**, 17-25, doi:10.1016/j.pss.2010.10.006.

Shemansky, D. E., P. Matheson, D. T. Hall, H. -Y. Hu, and T. M. Tripp (1993), Detection of the hydroxyl radical in the Saturn magnetosphere, *Nature*, **363**, 329-331, doi:10.1038/363329a0.

Smith, H. T., R. E. Johnson, M. E. Perry, D. G. Mitchell, R. L. McNutt, and D. T. Young (2010), Enceladus plume variability and the neutral gas densities in Saturn's magnetosphere, *J. Geophys. Res.*, **115**, A10252, doi:10.1029/2009JA015184.

Spahn, F., J. Schmidt, N. Albers, M. Hörning, M. Makuch, M. Sei$\beta$, S. Kempf, R. Srama, V. Dikarev, S. Helfert, G. Moragas-Klostermeyer, A. V. Krivov, M. Sremcevic, A. J. Tuzzolino, T. Economou, E. Grün (2006), Cassini dust measurements at Enceladus and implications for the origin of the E ring, *Science*, **311**, 1416-1418, doi:10.1126/science.1121375.

Stevenson, D. J. (1982), Interiors of the giant planets, *Annu. Rev. Earth Planet Sci.*, **10**, 257-295, doi:10.1146/annurev.ea.10.050182.001353.

Stevenson, D. J. (1983), Planetary magnetic fields, *Rep. Prog. Phys.*, **46**, 555-620, doi:10.1088/0034-4885/46/5/001.

Stone, E. C., and T. C. Owen (1984), The Saturn system, in *SATURN*, edited by T. Gehrels, and M. S. Matthews, The University of Arizona Press, Tucson, Arizona, pp. 3-23,

Teolis, B. D., G. H. Jones, P. F. Miles, R. L. Tokar, B. A. Magee, J. H. Waite, E. Roussos, D. T. Young, F. J. Crary, A. J. Coates, R. E. Johnson, W. -L. Tseng, and R. A. Baragiola (2010), Cassini finds an oxygen-carbon dioxide atmosphere at Saturn's icy moon Rhea, *Science*, **330**, 1813-1815, doi:10.1126/science.1198366.

Thomsen, M. F., D. B. Reisenfeld, D. M. Delapp, R. L. Tokar, D. T. Young, F. J. Crary, E. C. Sittler, M. A. McGraw, and J. D. Williams (2010), Survey of ion plasma parameters in Saturn's magnetosphere, *J. Geophys. Res.*, **115**, A10220, doi:10.1029/2010JA015267.

Tyler, G. L., V. R. Eshleman, J. D. Anderson, G. S. Levy, G. F. Lindal, G. E. Wood, and T. A. Croft (1981), Radio science investigation of the Saturn system with Voyager 1: Preliminary results, *Science*, **212**, 201-206, doi:10.1126/science.212.4491.201.

Tyler, G. L., V. R. Eshleman, J. D. Anderson, G. S. Levy, G. F. Lindal, G. E. Wood, and T. A. Croft (1982), Radio science with Voyager 2 at Saturn: Atmosphere and ionosphere and the Masses of Mimas, Tethys, and Iapetus, *Science*, **215**, 553-558, doi:10.1126/science.215.4532.553.

Wahlund, J. -E., R. Boström, G. Gustafsson, D. A. Gurnett, W. S. Kurth, T. Averkamp, G. B. Hospodarsky, A. M. Persoon, P. Canu, A. Pedersen, M. D. Desch, A. I.

Eriksson, R. Gill, M. W. Morooka, and M. André (2005), The inner magnetosphere of Saturn: Cassini RPWS cold plasma results from the first encounter, *Geophys. Res. Lett.*, **32**, L20S09, doi:10.1029/2005GL022699.

Wahlund, J. -E., M. André, A. I. E. Eriksson, M. Lundberg, M. W. Morooka, M. Shafiq, T. F. Averkamp, D. A. Gurnett, G. B. Hospodarsky, W. S. Kurth, K. S. Jacobsen, A. Pedersen, W. Farrell, S. Ratynskaia, and N. Piskunov (2009), Detection of dusty plasma near the E-ring of Saturn, *Planet. Space Sci.*, **57**, 1795-1806, doi:10.1016/j.pss.2009.03.011.

Waite, J. H. (1981), *The ionosphere of Saturn*, PhD Thesis, Univ. of Michigan, Ann Arbor.

Waite, J. H., Jr., M. R. Combi, W. -H. Ip, T. E. Cravens, R. L. McNutt Jr., W. Kasprzak, R. Yelle, J. Luhmann, H. Niemann, D. Gell, B. Magee, G. Fletcher, J. Lunine, and W. -L. Tseng (2006), Cassini Ion and Neutral Mass Spectrometer: Enceladus plume composition and structure, *Science*, **311**, 1409-1412, doi:10.1126/science.1121290.

Wilson, R. J., R. L. Toker, M. G. Henderson, T. W. Hill, M. F. Thomsen, and D. H. Pontius Jr. (2008), Cassini plasma spectrometer thermal ion measurements in Saturn's inner magnetosphere, *J. Geophys. Res.*, **113**, A12218, doi:10.1029/2008JA013486.

Wilson, R. J., R. L. Toker, and M. G. Henderson (2009), Thermal ion flow in Saturn's inner magnetophere measured by the Cassini plasma spectrometer: A signature of the Enceladus torus? *Geophys. Res. Lett.*, **36**, L23104, doi:10.1029/2009GL040225.

Yaroshenko, V. V., S. Ratynskaia, J. Olson, N. Brenning, J. -E. Wahlund, M. Morooka, W. S. Kurth, D. A. Gurnett, and G. E. Morfill (2009), Characteristics of charged

dust inferred from the Cassini RPWS measurements in the vicinity of Enceladus, *Planet. Space Sci.*, **57**, 1807-1812, doi:10.1016/j.pss.2009.03.002.

Young, D. T., J. -J. Berthelier, M. Blanc, J. L. Burch, S. Bolton, A. J. Coates, F. J. Crary, R. Goldstein, M. Grande, T. W. Hill, R. E. Johnson, R. A. Baragiola, V. Kelha, D. J. McComas, K. Mursula, E. C. Sittler, K. R. Svenes, K. Szegö, P. Tanskanen, M. F. Thomsen, S. Bakshi, B. L. Barraclough, Z. Bebesi, D. Delapp, M. W. Dunlop, J. T. Gosling, J. D. Furman, L. K. Gilbert, D. Glenn, C. Holmlund, J. -M. Illiano, G. R. Lewis, D. R. Linder, S. Maurice, H. J. McAndrews, B. T. Narheim, E. Pallier, D. Reisenfeld, A. M. Rymer, H. T. Smith, R. L. Tokar, J. Vilppola, C. Zinsmeyer (2005), Composition and dynamics of plasma in Saturn's magnetosphere, *Science*, **307**, 1262-1266. doi:10.1126/science.1106151.